Stony Brook University

The Role of Protein/Substrate Interface in the Functioning Biomedical Devices

A Dissertation Presented

by

Liudi Zhang

to

The Graduate School

in Partial Fulfillment of the

Requirements

for the Degree of

Doctor of Philosophy

in

Materials Science and Engineering

Stony Brook University

December 2015

Stony Brook University

The Graduate School

Liudi Zhang

We, the dissertation committee for the above candidate for the

Doctor of Philosophy degree, hereby recommend

acceptance of this dissertation.

Dr. Miriam H. Rafailovich – Dissertation Advisor
Distinguished Professor, Department of Materials Science and Engineering
Stony Brook University

Dr. Dilip Gersappe – Chairperson of Defense
Professor, Department of Materials Science and Engineering
Stony Brook University

Dr. Keith Jones
Adjunct Professor, Department of Materials Science and Engineering
Stony Brook University

Dr. Marcia Simon
Professor, Department of Oral Biology and Pathology
Stony Brook University

This dissertation is accepted by the Graduate School

Charles Taber
Dean of the Graduate School

Abstract of the Dissertation

The Role of Protein/Substrate Interface in the Functioning Biomedical Devices

by

Liudi Zhang

Doctor of Philosophy

in

Materials Science and Engineering

Stony Brook University

2015

Choosing the right materials can be critical to biomedical device performance. Usually factors such as biocompatibility, function, and cost are considered. Here we focused on the interactions between proteins, cells, and the material surfaces used for their biomedical application.

The influence of surface hydrophobicity and hydrophilicity on adsorbed fibrinogen conformation, orientation, fiber formation and platelet adhesion has been investigated to understand the interactions between blood components and the materials used in blood-contacting medical devices. The results indicate that fibrinogen adsorbed to either hydrophobic or hydrophilic polymer surfaces binds platelets, implying that both surfaces are potentially thrombogenic. We

present a model for surface initiation of clots, which enabled the design of a quick screen for thrombogenesis and guides the innovation and design of new anti-thrombogenic materials.

In addition, the interactions of polyisoprene (PI) and commercially Gutta-percha (nanoparticles filled PI) with dental pulp stem cells (DPSC) has been evaluated. The composition of three different kinds of Gutta-percha is consistent with their mechanical properties. The biocompatibility tests show that the Gutta-percha used in our study are non-cytotxic for human adult DPSCs, and could induce biomineralization by DPSCs without the addition of a chemical inducer. Then, the study of influence of PI substrates moduli on differentiation of DPSCs show that the “hard, G>2.3MPa” substrates can improve cell proliferation and induce biomineralization without chemical inducer. The results indicate that Gutta-percha, which is a filling material currently used in endodontic practice, can be potentially used in regeneration of the tooth, rather than obduration of the canal. PI as a polymer matrix can also be used in re-engineer scaffold for tooth regeneration therapy.

Hence, the study of interface between protein/cells and substrates could help the choice of materials and the design of biomedical devices.

Dedicated To

My

Family

Table of Contents

List of Figures

List of Tables

Acknowledgments

A lot of the greatest peoples have inspired me to perform valuable works throughout my six years in Stony Brook. I would like to start by sincerely thanking my advisor, Prof. Miriam H. Rafailovich, not only for knowledge, creativity and research guidance, but also for various components of my life. Without her constant encouragement, advice, and financially support, this work would not be possible. I feel so lucky for being her PhD student all these years.

I sincerely thank Prof. Marcia Simon, who gave me the opportunity to work with them in the Department of Oral Biology and Pathology. The close collaboration, generous assistance, and invaluable discussions have inspired me a lot in this study.

I greatly thank Prof. Keith Jones for the efficient collaboration, discussions, and suggestions, which greatly speed up the progress of my project.

I must also extend thanks to Prof. Dilip Gersappe for serving my dissertation committee and his suggestions.

During this six years, I have many collaborations, and I wish to express my warmest thanks to them for their great help. I sincerely thank Prof. Dennis Galanakis from Department of Pathology for mentoring and guiding my research on blood clot. His never-ending enthusiasm for research is so impressive. I greatly thank Dr. Katherine Vorvolakos, Dr. Brendan Casey, Dr. Jiwen Zheng, Dr. Qijin Lu, Dr. Richard Malinauskas, and Dr. Shelby Skoog from FDA, for their invaluable favors. It's my great honor to work with them. I want to extend my special thanks to Prof. Richard Clark from Department of Biomedical Engineering, and Prof. Stephen Walker from Department of

Oral Biology and Pathology, Stony Brook University. Without their support, I would not have overcome so many barriers. I am also grateful to Prof. Daniel Ou-Yang and Dr. Ming-Tzo Wei from Physics Department of Lehigh University, for the generous assistance and discussion.

It is also my pleasure to extend my thanks to my preliminary members, Prof. Jonathan Sokolov and Prof. Alexander Orlov, for their assistance and valuable comments.

Thank Dr. Jim Quinn, Dr. Christine Falabella, Dr. Adriana Pinkas-Sarafova, and Ms. Lourdes Collazo, for their help with my experiment.

I greatly appreciate the technical assistance and informative conversations from all the Garcia MRSEC members: Dr. Ying Liu, Dr. Chung-Chueh Chang, Dr. Seongchan Pack, Dr. Jaseung Koo, Dr. Yantian Wang, Dr. Xiaolan Ba, Dr. Divya Bhatnagar, Dr. Cheng Pan, Dr. Tatsiana Mironava, Dr. Kai Yang, Dr. Sisi Qin, Youjun Zhai, Chien-Hsu Lin, Yingjie Yu, Linxi Zhang, Hongfei Li, Clement Marmorat, Vincent Ricotta, Yichen Guo, Kuan-Che Feng, Yan Xu, Fan Yang, Ke Zhu, NaHyun Cho, Shan He, Zhenhua Yang, Kao Li, Julia Budassi, Yuan Xue, Xianghao Zuo, Juyi Li, and Mariah Geritano. They are great support for me all the time.

Finally, I would like to express my gratitude and share my happiness with my family. Since their love, support, and encouragement have driven a completion of my dissertation, I hereby dedicate this dissertation to my family.

Chapter 1: Introduction

1.1 Biomedical Devices

Biomedical device, defined from U.S. Food and Drug Administration (FDA) (the Medical Device, Food, Drug and Cosmetics Act, Section 201 (h)), is an instrument, apparatus, machine, contrivance, implant, in vitro reagent, or similar or related article, including a component part, or accessory used to diagnose, prevent, or treat disease. The definition of biomedical device is different from drug. It could not achieve its primary intended purposes through chemical action within or on the body.

There are numerous biomedical devices in current use. Although they vary in complexity and application, they are all targeted at protecting human health and safety. According to FDA's definition, biomedical devices for clinic use range from both simple devices such as tongue depressors to advanced devices such as laser surgical instruments. In addition, *in vitro* diagnostic products, such as general purpose lab equipment, reagents, and antibody test kits, could also be considered as biomedical devices. The implants and prostheses are some of the most complex and cutting-edge products available today, such as hip implants, pace makers, artificial heart valves, stents, catheters, breast implants, *etc*. [1, 2]. Even though they can help to save or improve the quality of a patient's life, the design of medical devices constitute a major challenge of the field of biomedical engineering.

1.2 Biomaterials

When designing a biomedical device, materials must be chosen to meet performance demands of safety requirement [3]. The most response to the materials/device must also be monitored for unanticipated adverse events leading to device failure [1]. To determine the material candidate, we need to consider biodegradation, compatibility with sterilization, and several other factors such as biocompatibility, qualification, functioning, and cost [3, 4]. A biomaterial is a nonviable material used in a medical device, intended to interact with biological systems [1]. The compatibility of biomaterials reflects how biomaterials interact with the human body and eventually how those interactions determine the clinical success of a medical device [5].

In this dissertation, we focus on biomaterials for two kinds of medical devices, blood-contacting medical devices and dental devices. Since these two kinds of medical devices are usually performed directly in contact with tissue or protein of human body, researches on interfaces between protein/cells and materials of devices are necessary. On one hand, blood-contacting medical devices, e.g. drug-eluting stents, have been reported on stent thrombosis occurred late after implantation [6]. This material surface initiated aberrant coagulation within blood vessels could be life threatening. On the other hand, some materials for dental devices, e.g. hydrogel and hydroxyapatite, have been reported to be able to induce stem cells differentiation, thus, may have potential application on tooth regeneration therapy [7, 8]. Hence the characterization and biological analysis of protein/cells with different material surfaces should be considered for biomedical application. It will be essential to help choosing materials, innovation and the design of these medical devices.

Chapter 2: The influence of surface hydrophobicity and hydrophilicity on adsorbed fibrinogen conformation, orientation, fiber formation and platelet adhesion

2.1 Introduction

Hemostasis is a complex process involving a multitude of proteins, enzymes and cellular components. Fibrinogen, an integral protein of the body's hemostatic system, usually circulates in plasma at 2-4 mg/ml, but during inflammation can exceed 7 mg/ml. It is composed of two sets of three non-identical polypeptide chains: Aα, Bβ, and γ chain [9]. The amino termini of all six chains are disulfide-linked, forming its central E region while the outer two D regions comprise disulfide-linked carboxyl terminal portions of Bβ and γ chains and a portion of the Aα chain. The two coiled-coil connectors connect the central and outer regions that join them in a symmetrical way. (Figure 2.1) [10, 11]. Upon activation by thrombin, fibrin molecules are polymerized together and cross-linked via Factor XIII, to produce a polymer mesh capable of interacting with blood platelets, extracellular matrix components, and erythrocytes, to seal vascular wounds and prevent blood loss[12]. Although fibrinogen is vital to prevent blood loss upon vascular insult, the protein has also been implicated in the formation of life-threatening vascular thrombosis[13] which may occur in the absence of thrombin, and is especially prevalent when material implants are in contact with blood [14, 15].

Specially chosen polymers have been used in medical applications for a long time due to their biocompatibility [16, 17], multiple functionality [18, 19] , and ease of processing[20]. Common medical device polymers include: polystyrene (PS), usually used for diagnostic instruments, delivery devices, and medical devices housings [21]; poly(methylmethacrylate) PMMA, used for chest drainage units, ventilation accessories, check valves, blood handling components, and intravascular catheter accessories [22]; polylactic acid (PLA), is used for sutures, orthopedic fixation devices, dental implants, stents, dialysis media, skin covering devices, and drug-delivery devices[23, 24] and poly(4-vinylpyridine) (P4VP) is in coatings for catheters, and particles for drug delivery systems [25-27]. Despite their popularity, polymers are also known for induction of thrombogenesis [28, 29]. Despite a large body of ongoing work, no definitive association has been established between material traits of surface chemical composition, charge, or hydrophilicity[30, 31] and the mechanism of clot formation.. Hence, in addition to systemic anti-coagulant medications which are prescribed for the patient [32-34] when devices containing polymers, e.g., stents or valves, are introduced into the blood stream, the surfaces of the implants are modified with drug eluting coatings to prevent restenosis. Yet despite these precautions, it has been shown that the incidence of thrombosis following implantation of drug eluting sirolimus-stent can be as high as 1.2% within four years, which is higher than the risk from bare metal stents (BMS) which is 0.6%. [35]. MacFadden EP *et al*. reported -that late stage thrombosis could also occur when anti-platelet therapy was discontinued, indicating that as the drug eluting factors were depleted, the risk of spontaneous thrombus formation from contact with the polymer surface was still present; the authors recommended extension of the anti-platelet treatment[6]. The focus on prevention of platelet adhesion was based on a large body of work which had shown that platelet adsorption readily occurred on biomaterial surfaces, regardless of their charge or functionality [36-39]. The

role of circulating fibrinogen in the platelet adhesion to biomaterial surfaces, is an open question, notwithstanding its rapid adsorption to such surfaces [40]. These reports therefore underscore the importance of understanding the fundamental aspects of the blood/materials interactions which generate thrombi, and can lead to formulation of new materials that lack thrombogenic potential without invoking restenosis or drug eluting coatings.

Our previous research has shown that hydrophobic surfaces can mimic the effect of thrombin and initiate self-assembly of fibrinogen fibers. We have found that the fibers can form in the absence of thrombin on hydrophobic polymer or metal surfaces, such as the materials of the types commonly used for stents [40, 41]. The E and D regions of the fibrinogen molecule were adsorbed on these surfaces, and the results indicated untethering of the αC regions (exposing the αC connector: Aα221-391 and αC domain: Aα 392-610). Our results further indicated that this exposure in turn recruited soluble fibrin and fibrinogen molecules, resulting in the formation of large fiber structures and networks parts of which were linked to the surface, with a several molecule thick surface coating comprising mostly fibrinogen or fibrin monomers. Typically, only a fraction of fibrinogen participated in forming these fibers and networks and there was no progression to clot formation. To assess the surface linkage further, thromboelastographic of thrombin induced clots disclosed that they readily anchored onto the hydrophobic (polyacrylic) surface [42]. Modification of the surface with UV/Ozone to decrease the water contact angle [42], or introducing P4VP copolymers [41], prevented fiber formation, thus establishing the central role of hydrophobic adsorption. The lack of fiber formation by hydrophilic surfaces was attributed to failure to untether the αC parts of the molecule. Exposing the αC domains via surface adsorption also enabled endothelialization by exposing the RGD sequences at the Aα 572-574 location which are responsible for endothelial cell adhesion [41, 43]. However, even though these data were

suggestive of the role of the surface in clot initiation, they were not yet conclusive, since data on platelet adhesion, which is central to thrombogenesis, were not provided. A key characteristic of hydrophobic adsorption was that fiber networks consistently failed to progress to clot formation, a feature possibly reflecting the behavior or soluble fibrin content of fibrinogen preparations. Advantage was taken of this, in present studies, to examine the possibility of platelet adhesion to these fibers.

The correlation between fibrinogen adsorption and platelet adhesion has been reported previously [44]. The integrin $\alpha_{IIb}\beta_3$ (glycoproteins GPIIb/IIIa) on the platelet membrane is the primary receptor set involved in platelet adhesion, but the corresponding domains are not readily available on the fibrinogen molecule in the absence of cleavage by thrombin. It has been proposed by several groups that the process of surface adsorption can sufficiently alter the conformation of fibrinogen such that different platelet binding domains become available [45, 46]. Here we investigate whether the conformation of the fibrinogen in the surface-induced fibers reported previously [40, 41] exposes otherwise cryptic sites enabling them to recruit platelets. The results demonstrate adhesion of platelets to these fibers in the absence of thrombin. The observations described herein will inform a more comprehensive model of surface-induced clot initiation that potentiates thrombogenesis apart from that induced in thrombin generation sites. The results, moreover, can aid in the development of a rapid screen for potentially thrombogenic materials, and help design of new surfaces which would suppress thrombosis and obviate the addition of anticoagulant agents.

2.2 Experimental Section

2.2.1 Preparation of polymer surfaces

Four kinds of polymers were chosen for this study: polystyrene (PS) (Mw=311,100, polydispersity index (PI) =1.05, from Scientific Polymer Products, Ontario, NY), poly(methylmethacrylate) (PMMA) (Mw=94,100, polydispersity index (PI)=1.03, from Scientific Polymer Products), polylactic acid (PLA) (Mw=131,300, polydispersity index (PI) =2.00, from Durect Corporation, Birmingham, AL), poly(4-vinylpyridine) (P4VP) (Mw=60,000, from Sigma-Aldrich, St. Louis, MO). The PS and PMMA were dissolved in the toluene (Sigma-Aldrich), PLA was dissolved in chloroform (VWR International, Plainfield, NJ), and the P4VP was dissolve in the Dimethylformamide (Sigma-Aldrich). The solutions were spin-cast onto substrates at 2500rpm for 30s. There were three kinds of substrates involved in this study. First, silicon wafers with orientation (100) (Wafer World, West Palm Beach, FL), were cut to 1cm×1cm square and sonicated in methanol for 10 min. They were boiled in a mixed ($H_2O/H_2O_2/NH_3H_2O$ 5:1:1 by volume) ammonia-peroxide solution for 15min, rinsed in deionized (DI) water, then boiled in piranha solution ($H_2O/H_2O_2/H_2SO_4$ 3:1:1 by volume) for 15min, and rinsed in deionized (DI) water, to create a hydrophilic surface. There was one more step to create a hydrophobic surface: immerse surface in diluted hydrofluoric acid solution (H_2O/HF 10:1) for 30s. Second, 12mm diameter Micro Coverglass slide (Electron Microscopy Sciences, Hatfield, PA), which was needed for fluoresce microscopy imaging because of its transparent, was cleaned by sonication in methanol for 10 min before use. Third, Kapton film (Fralock, Valencia, CA) was chosen for flow experiment because of its flexibility. These substrates were then rinsed with DI water again and dried in N_2 gas before the film coating. The thickness of the layers, approximately 100nm, was measured by ellipsometry (Rudolph Technologies, Flanders, NJ). P4VP was then annealed at 150℃ and other polymers at 130℃ in a vacuum of 10^{-3} Torr overnight to remove the residual

solvent and relax strains induced by the spinning process. After that, the water contact angle was measured six times on each surface.

2.2.2 Characterization of fibrinogen adsorbed on polymer surfaces

Human fibrinogen (fraction I-2) was isolated and dialyzed as previously described in ref [47]. Isolated fibrinogen, >97% clottable, was PMSF-treated to neutralize trace proteases. Solutions were prepared in tris (Trizma)-buffered saline (TBS; 10mM Tris, 150mM NaCl, pH=7.4) with 0.5mM ethylene diamineteraacetate disodium salt (EDTA) and stored frozen at -80 ℃. Two kinds of methods were used to adsorb isolated fibrinogen on polymer surfaces. First, static incubation: fibrinogen (0.1 mg/ml and 4 mg/ml in TBS, pH 7.4, 0.5mM EDTA) was incubated on spun-cast polymer films at ambient temperature for 12h. Second, to induce fibrinogen self-assembly by flow, fibrinogen (4 mg/ml in TBS, pH 7.4, 0.5 mM EDTA) was subjected to peristalsis in a 15 ml capacity circular 3/16" ID Tygon tube, at 100 ml/min, ambient temperature for 12h (Fig.7). The spun-cast polymer films on Kapton substrates were rolled and inserted into the tube. Besides isolated fibrinogen, PS and P4VP surfaces were also incubated in human whole plasma for 12h at ambient temperature.

Then, the adsorbed fibrinogen images were assessed by optical microscopy (OM) and Bruker Dimension ICON scanning probe microscopy (SPM) (Bruker, Santa Barbara, CA) scans. Both topographic and friction modes of SPM were used in this study. The samples were rinsed with TBS three times and then with DI water three times prior to OM and SPM measurement. To further evaluate the adsorbed fibrinogen on polymer surfaces, the amount of fibrinogen adsorbed on the substrates was estimated by QuantiPro Bicinchoninic acid (BCA) assays (Micro BCA^{TM} Protein

Assay Reagent Kit, Pierce, Rockford, IL) by calculating the color developed according to manufacturer instructions.

2.2.3 Monoclonal anti-fibrinogen IgG against the Aα and γ chains

Two monoclonal (mAb) anti-fibrinogen primary antibodies were used, anti-Aα529-539 mAb and anti-γ86-411 mAb to investigate the structure of fibrinogen on polymer substrates. For the anti-Aα529-539 mAb, polymer substrates were first incubated with 0.1 and 4mg/ml fibrinogen for 12 h at ambient temperature, stained the surfaces with this primary antibody at 4 ℃ overnight, and then stained with Alexa Fluor 594 conjugated goat anti-mouse lgG1 secondary antibody for 1.5h at ambient temperature. For the anti-γ86-411 mAb, two types of samples were prepared: (a) we first incubated polymer substrates with 0.1 and 4mg/ml fibrinogen for 12 h at ambient temperature, and then we stained the surfaces with anti-γ86-411 primary antibody at 4 ℃ overnight and Alexa Fluor 594 conjugated goat anti-mouse lgG1 secondary antibody for 1.5h at ambient temperature; (b) we first mixed 4mg/ml fibrinogen with the same primary antibody in solution, then incubated polymer substrates with the mixture for 12 h at ambient temperature, and then stained with the same secondary antibody for 1.5h at ambient temperature. Polymer substrates were also incubated with 4mg/ml BSA for 12h at ambient temperature, then stained with each primary and secondary antibody, as a negative control. PS and P4VP substrates were chosen for this experiment because of the different surface chemistry. A leica TCS SP8 X laser scanning confocal microscopy (Leica Microsystem, Buffalo Grove, IL) was employed to visualize the Alexa Flour 594 fluorescent on the surface.

2.2.4 Platelets binding and characterization

Fresh human blood was obtained from the National Institutes of Health (NIH) Blood Donor Research Program. Upon receipt, the blood was centrifuged (200G, 10 min) to obtain platelet rich plasma (PRP). The PRP was then passed through a sepharose column (Sepharose 2B, 60-200 μm) to separate the platelets from the plasma components, and obtain gel-filtered platelets (GFP). After that, the platelets were diluted to 200,000/μL in TBS solution. To investigate platelets binding to fibrinogen/fiber, half of the spun-cast polymer films was incubated with 0.1 and 4mg/ml fibrinogen for 12h at ambient temperature. Both the fibrinogen pre-incubated surfaces and blank polymer surfaces were then incubated in the GFP for 1 h at ambient temperature. Two kinds of methods were used to adsorb platelets onto surfaces. First, static incubation on a shaker at 60 rpm. Second, flow loop in a 15 ml capacity circular 3/16" ID Tygon tube at 100 ml/min. The Kapton samples were rolled and inserted into the tube.

After incubation the surfaces were rinsed twice with TBS for the following characterization..Half of the surfaces were blocked with 1% bovine serum albumin (BSA, Sigma) for 30 min at ambient temperature to prevent nonspecific antibody binding. The surfaces were then rinsed with TBS and incubated with CD41-FITC conjugated antibody (Beckman Coulter, Jersey City, NJ) for 30 min at ambient temperature on a shaker at 60 rpm. A Nikon ECLIPSE TE2000-U fluorescent microscopy (Nikon Inc, Melville, NY) was used to image platelets and fibrinogen fibers with both fluorescence and optical microscope modes. Then the images from these two modes were merged to investigate the distribution of platelets. The other half of the surfaces were fixed in 2 vol% glutaraldehyde (Sigma-Aldrich) for 12 h at room temperature. Next, the samples were dehydrated with graded ethanol series (0%, 25%, 50%, 70%, 95%, and 100%) and Hexamethyldisilazane (Thermo Fisher Scientific, Waltham, MA), and then allowed to air-dry overnight. These stages preserved and stabilized the 3D morphologies of the adherent platelets.

Scanning Electron Microscopy (SEM) (JEOL USA, Inc., Peabody, MA), at accelerating voltage from 5kV to 15kV, was used on gold sputter-coated (45s) samples to observe the platelet shape change, distribution and the total number density of the adhering platelets.

2.3 Results

2.3.1 Influence of surface chemistry on adsorbed fibrinogen

Polymeric surfaces were prepared by spin casting thin (~100nm) films onto polished single crystal silicon wafers or glass slides. In this manner the RMS surface roughness of the amorphous polymers films was less than 1nm, enabling us to image fine features of the adsorbed fibrinogen. The polymers, substrates, and the corresponding water contact angle measurements are listed in Table 2.1, where we can see that the values are a function of the polymer only, and not the underlying substrate. From the table we can also see that only the P4VP polymer can be considered "hydrophilic" in the context of the Berg Limit which defines hydrophobicity in terms of the water attraction forces and having a Young's contact angle $\theta > 65°$ [48]. PLA is the only substrate which was crystalline under ambient conditions with Tg=60℃. The polymer-coated substrates were incubated in 4mg/ml and 0.1mg/ml purified fibrinogen solutions in TBS at ambient temperature for 12h and then analyzed using Scanning Probe Microscopy (SPM). The SPM images generated in the topography mode are shown in Figure 2.2, where we can clearly see the effect of the concentration of protein in the solution. At the lower concentration of 0.1mg/ml no fibers are observed. This is also observed optically, as shown in the images of Figure 2.3. Rather, as the SPM friction mode images in Figure 2.4 elucidate, the surface appears to be covered by a uniform layer of monomers, having the tri-nodular structure shown in the inset. At the top of Figure 2.4, a cartoon of the monomer structure postulates that the hydrophobic D and E domains are adsorbed onto the

surface while the hydrophilic αC domains are free. Similar results were also reported by Koo *et al* for fibrinogen on hydrophobic clay surfaces [41]. No tri-nodular features are observed on the hydrophilic P4VP polymer, where, as shown in the inset, the surface is covered with irregular single nodular shapes. On the PLA surface in Figure 2.2 (lower image), we first see the surface nucleated spherulite structures of the crystalline polymer. Small fibrinogen clusters are seen decorating the spherulites, but the polymer lamellae, which are approximately 20nm depth, are assembled into features which mask the nodular structures, making it difficult to image them.

In contrast, the high concentration (4.0 mg/mL) fibrinogen solutions led to large fibers distributed on nearly the entire surface area of the hydrophobic polymers, as shown in the upper images of Figure 2.2 (topography SPM mode) and 2.3 (optical mode). SPM (friction mode) images in Figure 2.5 show large fibers, several microns in diameter, which are composed of smaller fibers that are anchored to the surfaces. Large fibers appear on PS, PMMA, and PLA surfaces. No fibers are observed on the hydrophilic P4VP surface.

The amount of adsorbed protein after 12 h incubation at the low and high concentrations, 0.1mg/ml and 4.1mg/ml, respectively was measured using BCA analysis. The results are shown in Figure 2.6. From the figure we can see that, given a specific fibrinogen concentration, the amount of protein is similar on all surfaces, regardless of the difference in ultrastructure: tri-nodular structures at the low concentrations and fibers at the large concentration. The amount on PLA is somewhat larger than on the amorphous polymers, but this may be correlated to the increased roughness, and therefore increased surface area to which protein can adsorb, generated by the polymer crystals. The major difference between P4VP and the other surfaces is therefore attributed mostly to the degree of hydrophobicity, which determines the structure of the adsorbed monomers. As the solution concentration is increased by a factor of 40, the amount adsorbed on all surfaces

is seen to increase 7~10 fold, indicating that the amount adsorbed is mostly dependent on the concentration in solution. The formation of the large fibers though is also seen to correlate with the degree of hydrophobicity.

Since fibrinogen is present in blood, flow effects are expected to be important in representing *in vivo* conditions. We therefore constructed a dynamic flow loop, which can mimic physiological blood flow conditions present in the human body. Polymer films were spin-cast on Kapton films which folded into tubes and inserted into the flow loop tubing (Figure 2.7). 15ml of 4mg/ml fibrinogen solution was flowed at a rate of 100ml/min through the PS and PLA surfaces for 12h. The surfaces of the polymer-coated Kapton inserts were examined with SPM and the images are shown in Figure 2.7. From the figure we can see that extensive fiber formation occurred in the absence of thrombin on both the PS and PLA coated surfaces. Both large and small fibers are observed, with dimensions similar to those observed under static conditions. Hence, dynamic flow did not seem to hinder fibrinogen adsorption or fiber self-assembly.

2.3.2 Fibrinogen structure on polymer surfaces

We have previously shown that the alpha-C domains were essential in the formation of the fibrinogen fibers [40]. Hence no fibers were formed when either des-αC, a fibrinogen fraction lacking the αC chains, or anti-bodies blocking the terminal region, Aα529-539 were used. In order to understand the role that the surface plays in locating the αC chains on the adsorbed Fg molecules, we stained with anti-Aα529-539 antibody the PS and P4VP surfaces after exposure for 12 h to 4mg/ml and 0.1mg/ml fibrinogen solutions. Even though the latter was not directly responsible for fiber formation, its location was critical in order to determine the orientation of the fibrinogen molecule. The results are shown in Figure 2.8. On the PS surface the fibers formed at the higher

incubation concentration are clearly outlined in bright red, confirming their proposed structure as having the knob/hole molecules in register with the αC domains on the outside. This conformation, produced by placing the hydrophilic moiety on the outside, is responsible for maintaining the solubility of the fibrinogen, and recruiting further molecules into the growing fibers. On the PS surface incubated the lower concentration which we had shown to produce only a monolayer of fibrinogen, a uniform red stain with very small fiber segments are observed. In contrast, no stain is observed on the P4VP surface incubated at the same concentration. As we had shown previously, BCA analysis indicates that approximately the same amount of fibrinogen is adsorbed on this surface, yet no fibers results at any concentration. Previously it was hypothesized that the αC domains, having a high content of carboxylic groups and being somewhat hydrophilic were preferentially adsorbed to the P4VP surface, rendering them incapable of recruiting further molecules to form the fibers. The lack of stain on the low concentration surface, where only monolayer coverage occurs, confirms this hypothesis. At the higher concentration, a uniform red stain is observed corresponding to further layers of adsorbed proteins, which are neither in contact with the P4VP surface which blocks the αC domains, nor are they organized in any other orientation, resulting in the uniform surface fluorescence.

In order to further confirm the influence of the surface on the structure of the adsorbed fibrinogen and its impact on the function we also stained the samples for anti-fibrinogen γ86-411 antibody. This segment of the molecule is very hydrophobic and is expected to be adsorbed onto hydrophobic surfaces and repelled from the hydrophilic ones. Two types of samples were prepared: (a) Samples where we first incubated fibrinogen on polymer substrates for 12 h and then we stained the surfaces with anti-fibrinogen γ86-411 primary antibody and Alexa Fluor 594 conjugated secondary antibody and (b) Samples we first mixed fibrinogen with the same primary antibody in

solution, incubated polymer substrates with the mixture for 12 h, and then stained with the secondary antibody. The images for both types of antibody-labeled fibrinogen are shown in Figure 2.9, where we observe no significant difference between images obtained by the two methods of labeling.

From the BCA data (Figure 2.6), and the SPM scans on the hydrophobic polymer surfaces (Figure 2.2 and 2.4), we had shown that fibrinogen is present both in fibers and as a coating of monomers in the regions around the fibers. Yet, from the location of the fluorescence it appears that the decapeptide domains are available only on the fibers. On the hydrophobic polymer samples with the lower fibrinogen concentration, only monomers and no fibers are observed, and no fluorescence is observed as well. On the hydrophilic surface on the other hand, where no fibers formed at either concentration, a broad film of florescence is observed at all concentrations.

The clinical relevance of these findings was also probed by exposing the PS and P4VP surfaces to whole plasma, rather than purified proteins. Fibers formed on the hydrophobic surfaces with the same morphology as those obtained from the purified samples after 12 h of incubation. The results presented in Figure 2.10.

2.3.3 Platelets binding on adsorbed fibrinogen/fiber

Platelets are known to express the domains, GPIIb/IIIa which are potential binding sites to decapeptide γ400-411, resident on the γ chain of human fibrinogen [10]. To further study the coagulation process, we incubated gel-filtered platelets (GFP) (200,000/ μL), which were isolated using a sepharose column [49], for 1 h on polymer surfaces that were pre-incubated for 12 h with fibrinogen solutions at 0.1mg/ml and 4mg/ml. The platelets were then stained with CD41-FITC antibody, and imaged with both fluorescence and optical microscope modes. These two modes

merged images are shown in Figure 2.11. This antibody binds integrin alpha 2b of the IIb/IIIa complex, which is part of a fibrinogen binding receptor expressed on the membrane of platelets as part of the coagulation process. From the images we see that on the hydrophobic polymers, the majority of the platelets are present on fibers, which are formed on the substrates exposed to the higher fibrinogen concentration. No staining is observed on the fibers which were not exposed to platelets, and only a few platelets were seen on the substrates pre-incubated at the lower fibrinogen concentration, where no fibers were observed.

A second set of samples prepared at same time were imaged with Scanning Electron Microscopy (SEM) and the results for PS, PMMA, and P4VP are shown in Figure 2.12. We see that on the hydrophobic surfaces incubated at the higher fibrinogen concentration, both large and small fibers are formed over much of the sample surface. Even though some platelets are observed on the flat regions, the majority of the platelets are observed on the fibers. This is observed even more clearly in the zoomed images of Figure 2.12 where we can see that multiple layers of platelets are aggregated on the fibers, which is consistent with the large intensity of FITC fluorescence observed on the fibers in the florescent images. Very few platelets are observed on the bare hydrophobic polymers or the substrates incubated at the lower concentration of fibrinogen, where no fibers were formed. It is interesting to note that the P4VP substrates were covered with a monolayer of highly extended platelets, where the platelet coverage did not seem to depend on the concentration of fibrinogen adsorbed.

Platelets adhesion experiments were also conducted with undiluted platelet rich plasma (PRP), which is closer to physiological conditions, but may also contain additional clotting factors. Similar results were obtained, where most of the platelets were adhered in multiple layers piled

onto the fibers. The higher platelet binding density reflecting the larger platelet concentration found in PRP. The images are shown in Figure 2.13.

In order to more closely simulate the *in vivo* environment, we set up a dynamic flow loop to mimic the physiological conditions of blood flow in the human body. Gel-filtered platelets (GFP) (200,000/μL) were flowed through Kapton tubes whose surfaces were coated with PS, PLA and P4VP, pre-incubated with the 4mg/ml fibrinogen for 12h. In order to inhibit platelet activation simply by the shear action during flow, EDTA was added [50]. SEM images of the surfaces after 1 h exposure are shown in Figure 2.14, where we can see that very few platelets are observed on the bare surfaces of PS and PLA, which were not pre-incubated with fibrinogen. On the surfaces which were pre-incubated, platelets are adhered mostly on the regions covered by the fibers. On the P4VP surface no fibers are observed after incubation with fibrinogen, but similar amounts of platelets are observed to adhere, regardless of exposure to fibrinogen. These results are consistent with those obtained under static conditions, except that the EDTA prevented activation, but not adhesion, of the platelets adsorbed on the P4VP surface.

2.4 Discussion

There has been a lot of research on blood compatibility of blood-contacting materials. These studies include protein adsorption, as well as platelet adhesion [51] both in static mode [52-54] and using flow loops to mimic flow conditions [55, 56]. It is well established that injury to blood vessel triggers the release of tissue factor and subsequent generation of thrombin, which produces fibrin fibers and induces platelet adhesion and activation. More recently, it was demonstrated that fibrinogen alone can mediate platelet adhesion on biomaterial surfaces [53] in absence of any wound activity. The structure of adsorbed fibrinogen was previously studied by our group on

hydrophobic and hydrophilic surfaces [40, 41]. It was shown using antibody blocking methods [40] and more recently atomic force microscopy [57] that on hard molecularly flat, hydrophobic surfaces, i.e. modified clay or graphite, the hydrophobic D and E domains are so strongly adsorbed to the surface that the fibrinogen molecule is distorted. This frees the αC domains, which in turn become available for recruiting other molecules into protofibril formation. In Figure 2.4 we show the surface substrates, coated with PMMA or PS films, that were exposed to 0.1mg/ml fibrinogen solution, where we could see that in both cases they are covered with a layer of fibrinogen molecules, clearly showing the tri-nodular structure (cartoon insert), indicative of strong adsorption. In Figure 2.2 we show the PS, PMMA, and PLA surfaces after exposure to higher, physiological concentrations of fibrinogen, where large fiber formations are visible. In Figure 2.5 we show high magnification topography and lateral force images of the PS surface, where we can see that the large fibers are collectives of smaller fibers anchored onto the surface. Hence, on these softer polymeric surfaces, the fibrinogen monomer adsorption is similar to that previously reported on the hard surfaces, where the αC domains are free and participate in recruiting other molecules, resulting in the formation of large fibers without the presence of thrombin. Despite their primary length scale similarity, the monomers coating the hydrophobic surfaces are fundamentally different than those recruited into forming the fibers. In Figure 2.15 we also label the platelet binding domain. From the figure we see that the domain is obscured by the polymer surfaces when the molecules are adsorbed directly onto the hydrophobic surfaces, whereas the domain is exposed when incorporated into the fibrinogen fibers. In contrast, on the hydrophilic surfaces, also shown in Figure 2.2 and 2.4, no tri-nodular structures are observed since the molecules are adsorbed with the more hydrophilic αC chains in contact with the polymer surface. In Figure 2.6 we compare the total amounts of protein adsorbed on the different polymer surfaces, where we can see no

significant differences in the respective amounts adsorbed by PS, PMMA and P4VP surfaces. Hence, as Figure 2.15 illustrates, the lack of fibers on P4VP at physiological fibrinogen concentration is interpreted as being due to the inability of the αC domains to continue polymerization of the fibers when they are adsorbed onto the surface. In the case of PLA, the larger amount of protein adsorbed may simply be due to the larger surface area presented by the rougher, crystalline morphology of the polymer, which can be seen beneath the fibrinogen fibers in Figure 2.2. The roughness is also too great to directly observe the tri-nodular structures, but their presence is inferred by the observation of large fibers on the substrates incubated at the higher concentration. These data also underscore that fibrinogen is easily adsorbed to either hydrophobic or hydrophilic surfaces, as previously reported by numerous groups. The nature of the surface, however, determines the morphology of the monomer, which in turn determines the ultrastructure of self-assembly on the surface and the formation of fibers.

The clinical relevance of these findings was also probed by conducting the experiments in whole plasma. In this case the concentration of fibrinogen is approximately 2-4mg/ml, which is sufficient to form fibers, yet, we wanted to probe whether the presence of other plasma proteins would interfere with fiber formation. The results showed that fibers, of the same appearance and dimension as those formed with the purified fibrinogen, were formed on the hydrophobic surface, and no fibers were observed on P4VP shown in Figure 2.10.

We can now correlate the availability of the platelet-binding domains with the structure of the adsorbed fibrinogen, and probe the configurations proposed in Figure 2.15. In Figure 2.9, we image the adsorbed fibrinogen after staining with fluorescent antibodies for the 86-411sequence on the γ chain. Even though this antibody covers a much wider area than the γ400-411 sequence required for platelet binding, its absence provides confirmation that the domain is not accessible for binding.

For the monomers adsorbed onto the hydrophobic surface, no fluorescence is observed, consistent with the domain being inaccessible for binding by the antibody, as shown in Figure 2.15. In contrast, strong fluorescence is observed on the fibers that are attached to the surface monomer sheet, again confirming the proposed configuration shown in Figure 2.15, where the domains are exposed on the fiber surface. Further complexity is revealed by significant fluorescence on the fibrinogen adsorbed onto the hydrophilic surfaces, at-both low and high concentrations, despite lack of fiber formation or tri-nodular structures. A possible explanation may be that the hydrophilic surface attracts the αC domains, while repelling the D and E domains, resulting in the structure shown in Figure 2.15, where the platelet binding become exposed. Hence, fluorescence would be observed only on the monomer sheets adsorbed on the surface, consistent with the observations.

In order to determine if the adsorbed fibrinogen fibers were able to initiate clotting, we first conducted experiments under static conditions with diluted platelets. The results are shown in Figure 2.11, where the platelets were labeled with FITC-CD41 antibodies and imaged with optical microscopy. From the figure we can see that intense fluorescence is observed only on the fibers. This is further confirmed by the SEM images where multiple platelets are observed on the fiber formations on the hydrophobic surfaces. The platelets have a rounded appearance, which according to the arbitrary classification of five stages of shape change for activated platelets [52], indicates a stage of partial activation. On the other hand, on the hydrophilic surfaces at both high and low fibrinogen concentrations, the surface is covered with flat platelets which according to classification are fully activated.

In order to simulate physiological conditions, a flow loop was established and sets of experiments were performed in order to determine physiological relevance of the static study results. First, 4mg/ ml fibrinogen, a concentration similar to that found in blood, was circulated in

the loop past Kapton covered tubes, coated with PS and PLA, for 12 h. The surfaces were examined with SPM and large fibers were observed on both surfaces. The distribution and appearance of the fibers was similar to that observed in the static experiments, confirming that the fibrillogenesis in the absence of thrombin was not an artifact of the static conditions under which the previous research [40, 41] was performed.

Platelets were also circulated past the polymer coated tubes that had been exposed to fibrinogen for 12 h. The results were very similar to those obtained under static conditions, where large amounts of platelets were observed to adhere to the fibers on PS and PLA, and very few platelets were observed on the control polymer surfaces. In contrast, platelets were found to adhere to the hydrophilic P4VP surface indiscriminately, even when the P4VP surface was not pre-coated. Even though the platelets had undergone filtration a small amount of fibrinogen may have still been present. The plasma was flowed for 1 h, which may have been insufficient time to form fibers at this low concentration, but was sufficient to form a thin adsorbed layer, which attracted the platelets due to exposure of the platelet binding domain.

These results fully confirmed the ones obtained in the static experiments. Since the flow experiments require a large amount of plasma and are complicated to set up and maintain in a clinical facility in a typical medical device facility, these results indicate that the static experiments suffice in order to screen for the possible spontaneous clot formation of a surface.

2.5 Conclusion

We have proposed a model for spontaneous clot formation on polymer surfaces. We showed that, when physiological concentrations were used, fibrinogen was adsorbed on hydrophobic

surfaces in a manner which facilitates fiber formation, whereas on hydrophilic surfaces the same amounts were observed but the conformations prevented fiber formation. Exposure of the surface to platelets, both under static and flow conditions indicated that the platelets adhere to the fibers on the hydrophobic surface, and to the adsorbed monomer on the hydrophilic surfaces. The platelet adhesion patterns correlated with conformations of the fibrinogen where the platelet binding domains were exposed. Hence both hydrophobic and hydrophilic polymer surfaces are able to initiate clot formation.

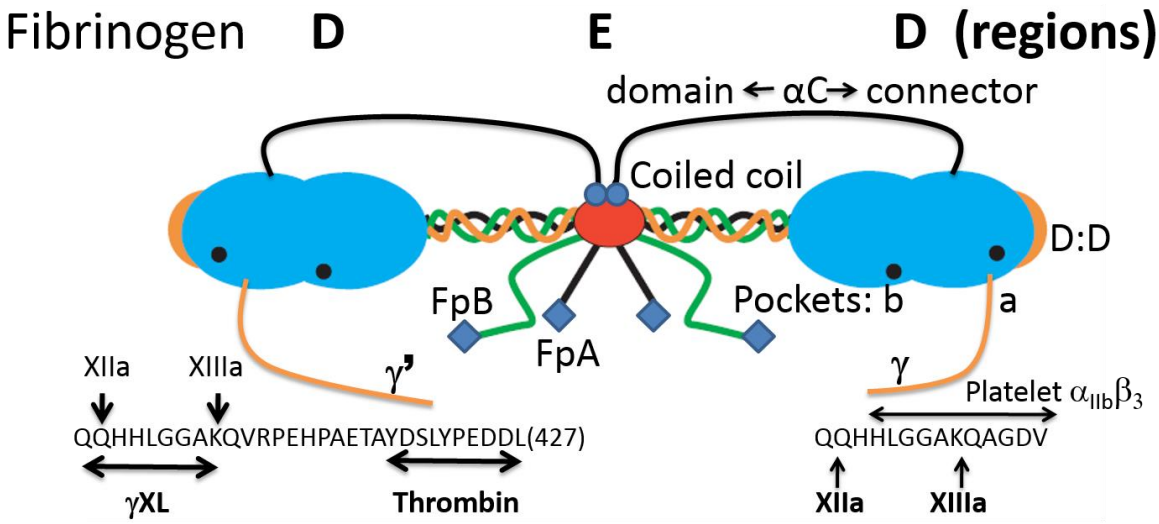

Figure 2.1 Schematic representation of the fibrinogen molecule and its functional regions. Top cartoon: the molecule is shown with its αC appendages tethered at its central or E region. This region also shows its fibrinopeptides FpA and FpB. Its outer or D regions show its constituently available pockets a and b, its D surface sights (D:D) that interface with their counterparts of another molecule during polymerization, and the two forms of its γ chain, γ and γ'. These indicate the residues crosslinked (γXL) by F XIIIa, the platelet receptor binding C terminal γ chain segment, and the thrombin binding C terminal γ' segement (i.e. the γ' is a splice variant present in ~15% of the molecules).

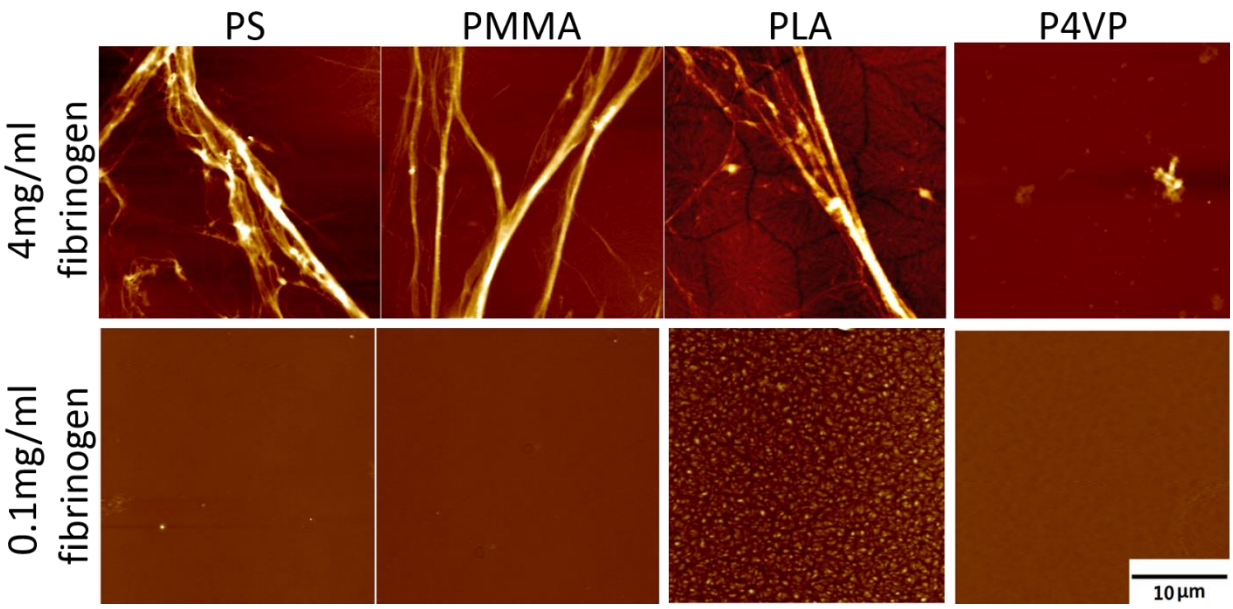

Figure 2.2 SPM images of the PS, PMMA, PLA, and P4VP polymer coated substrates incubated with 4mg/ml (top panel: Z scale 0-300nm) and 0.1mg/ml (bottom panel: Z scale 0-150nm) solutions of fibrinogen for 12 h. Note fiber formation occurs only at the higher concentration.

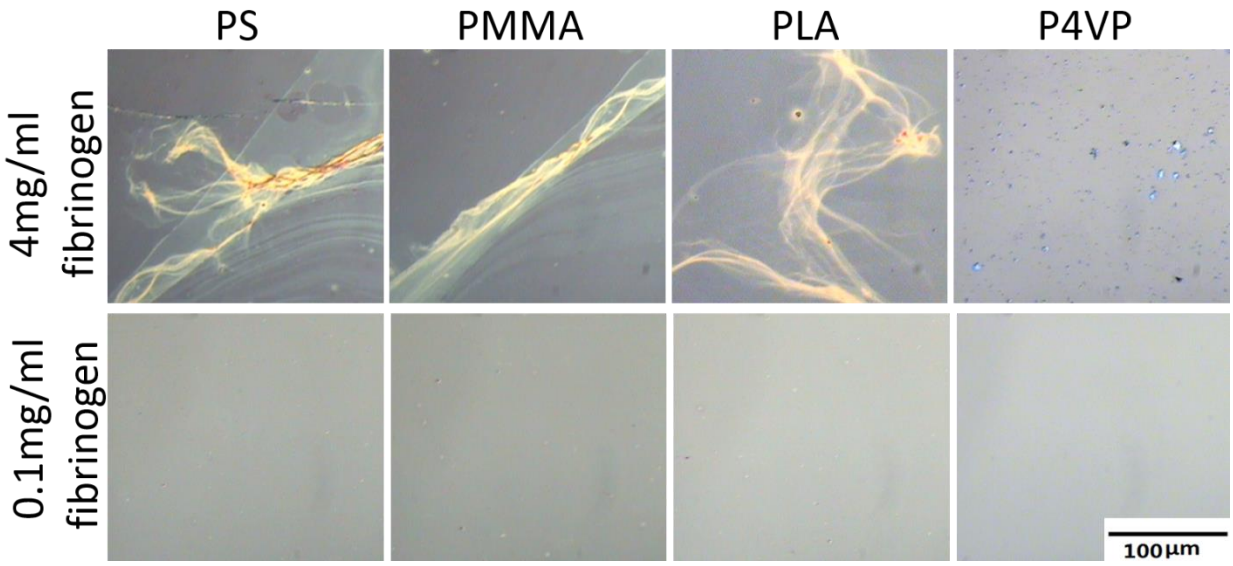

Figure 2.3 Optical microscope images of the samples imaged in figure 2A where we can see large fibrinogen fibers formed following its incubation on PS, PMMA, PLA, and P4VP surfaces as detailed in Methods. Shown are surface-linked fiber networks yielded at 4mg fibrinogen/ml on hydrophobic (PS, PMMA, PLA) surfaces and but not by 0.1mg/ml.

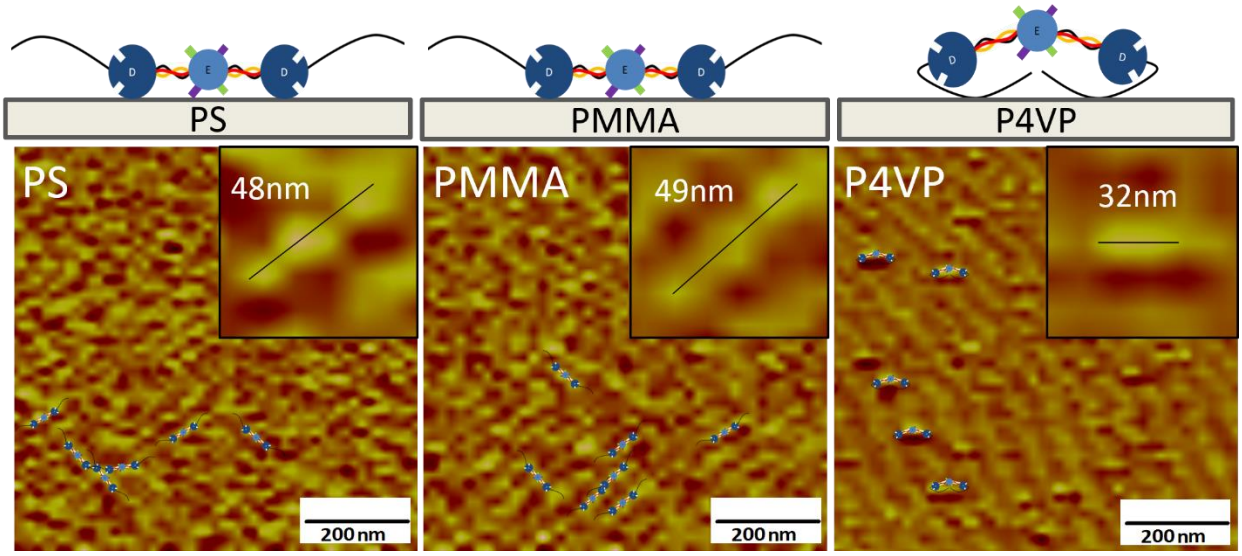

Figure 2.4 High resolution lateral force mode SPM images of the fibrinogen coating obtain after incubation with 01mg/ml Fibrinogen solution .The inserts show a highly magnified region where the orientation of the trinodular fibrinogen molecule on the surface could be observed. Similar images are also observed between fibrinogen fibers (data not shown). Note that the trinodular structures appear only on the hydrophobic surfaces. The illustration above each image is a cartoon showing the placement of the different segments of the fibrinogen molecule near hydrophobic (PS, PLA) and hydrophilic (P4VP) surfaces.

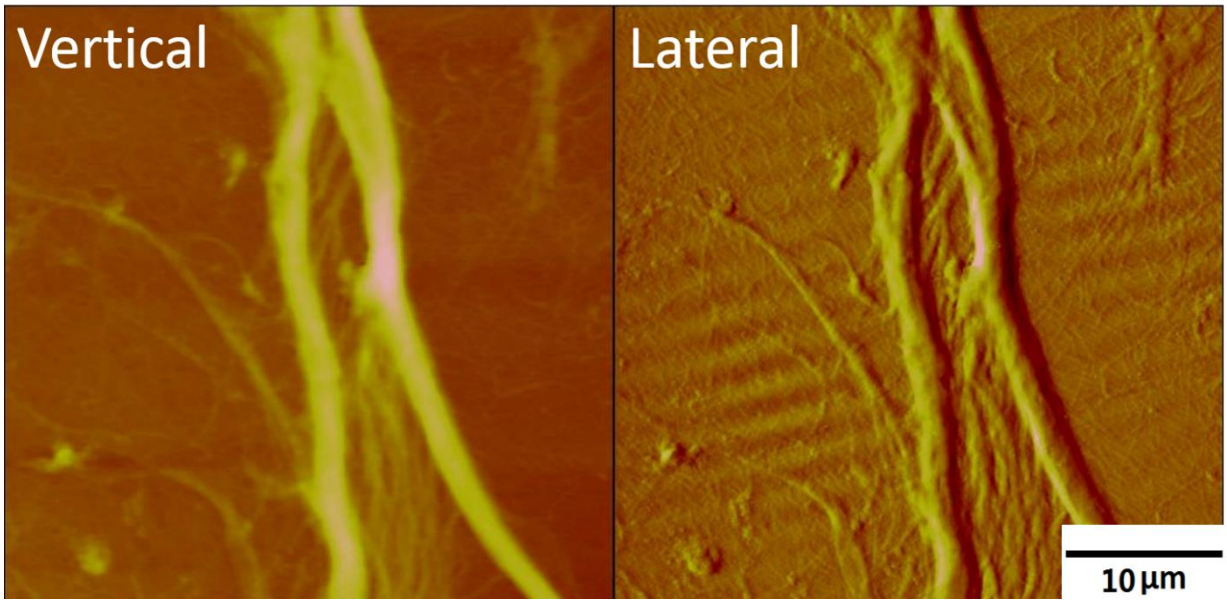

Figure 2.5 High resolution topographical and corresponding lateral force image of a fibrinogen fibers formed on a PS substrate. Note that the fiber is composed of smaller fibers, attached to the surface, which are intertwined and form very large surface anchored rope like structures. Z scales are 0-900nm for vertical and 0-2.5V for lateral.

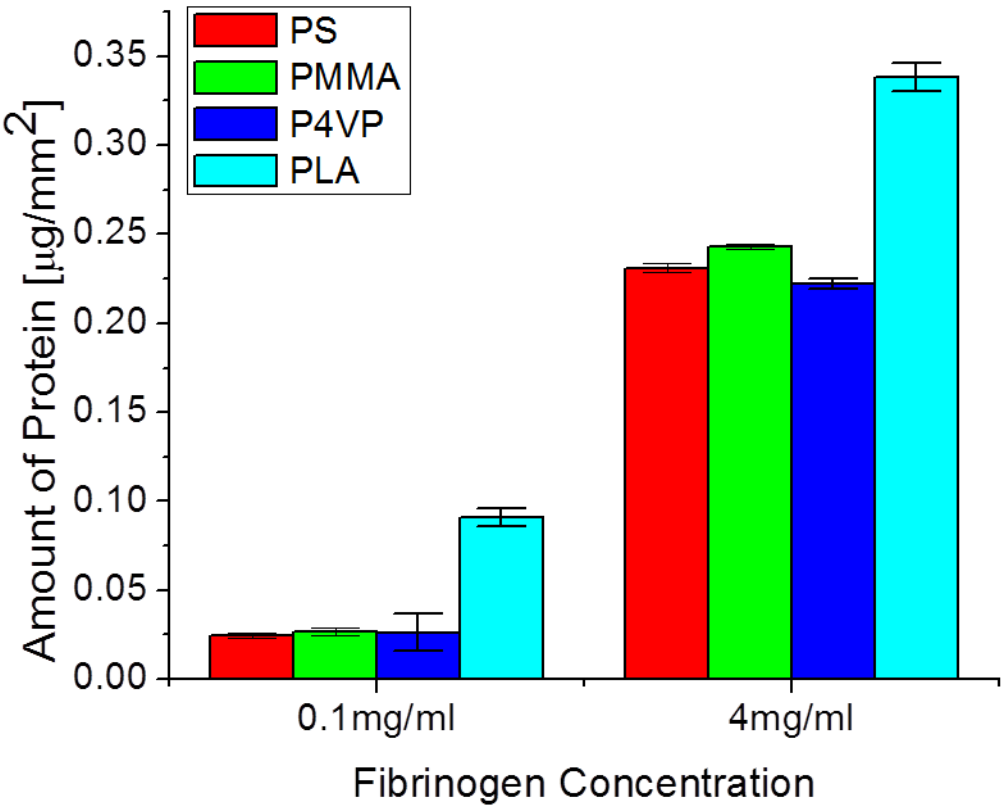

Figure 2.6 BCA measurements of fibrinogen adsorbed on PS, PMMA, P4VP, and PLA surfaces after 12 hours of incubation at two concentration, 0.1mg/ml and 4mg/ml.

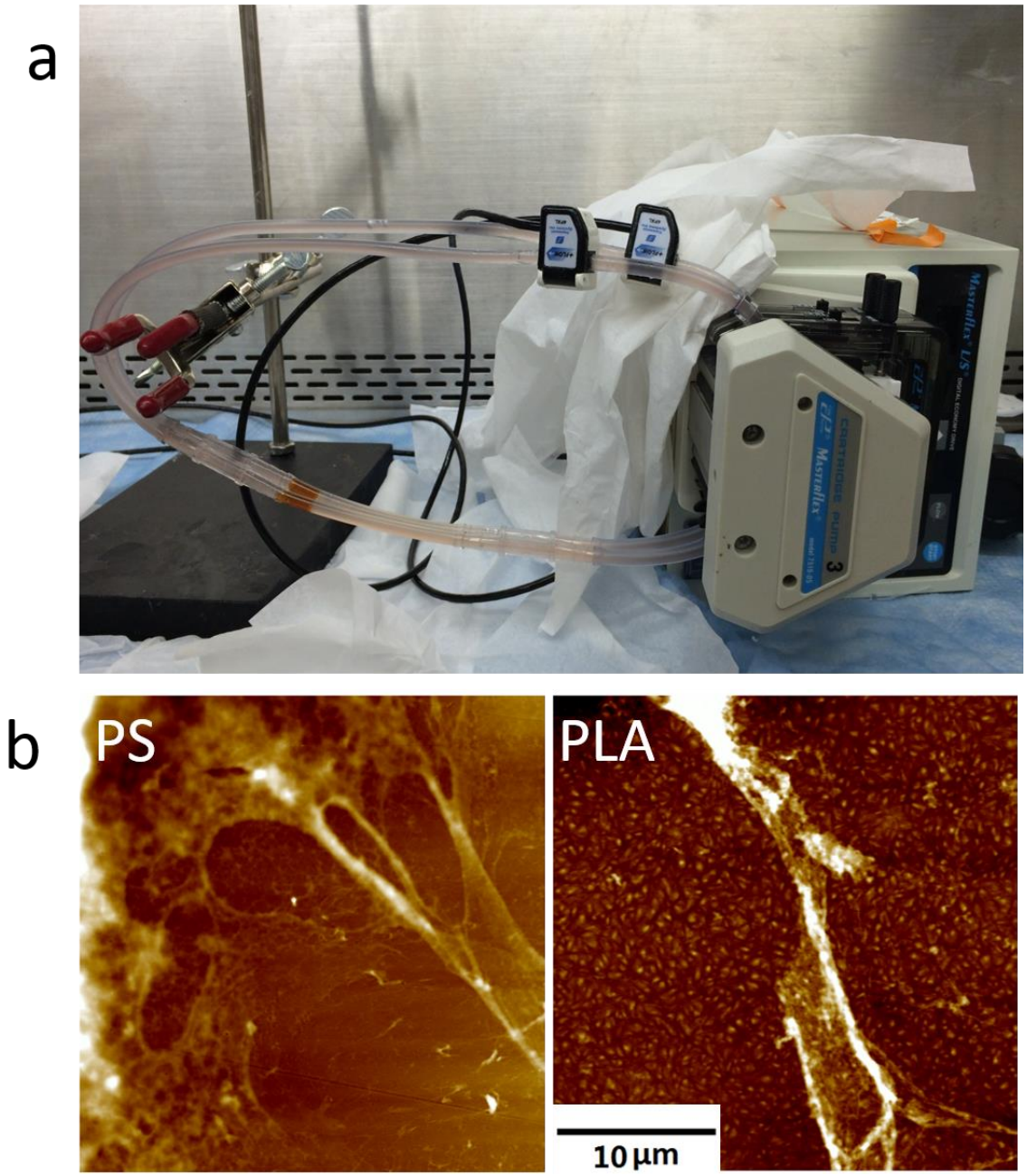

Figure 2.7: a. Closed flow loop device consisting of a 17.5 ml capacity circular 3/16" ID Tygon tube inserted into a peristalsis pump capable of circulating liquids at a constant flow rate of 100 ml/min. Adsorption of either fibrinogen or platelets to polymer coated surfaces was measured by insertion of a tubular Kapton structure, supporting a polymer coated substrate, directly into the flow through the Tygon tube as demarcated by the square box. b. Topographic SPM scans of the Kapton film inserts coated with PS (Left) and PLA (right) after being exposed for 12 hours to a flowing solution of 4mg/ml fibrinogen. Z scale is 0-300nm.

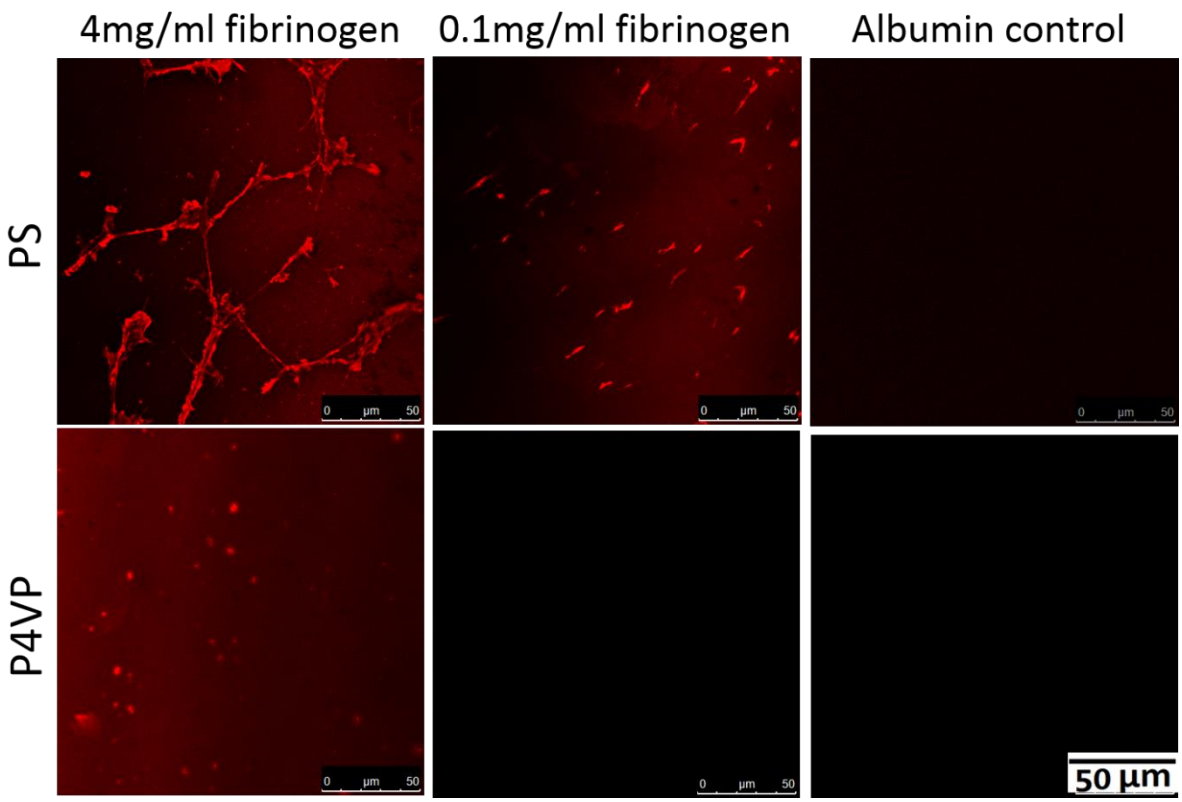

Figure 2.8 Confocal microscopy images of PS and P4VP spun cast thin films pre-incubated with the two fibrinogen concentrations shown, 12 h. To visualize images the plates were first exposed to anti-fibrinogen Aalpha chain 529-539 mAb, and then to Alexa Fluor 594-conjugatede anti-mouse IgG. Albumin controls are polymer substrates incubated with 4mg/ml BSA for 12h, then stained with same primary and secondary antibody.

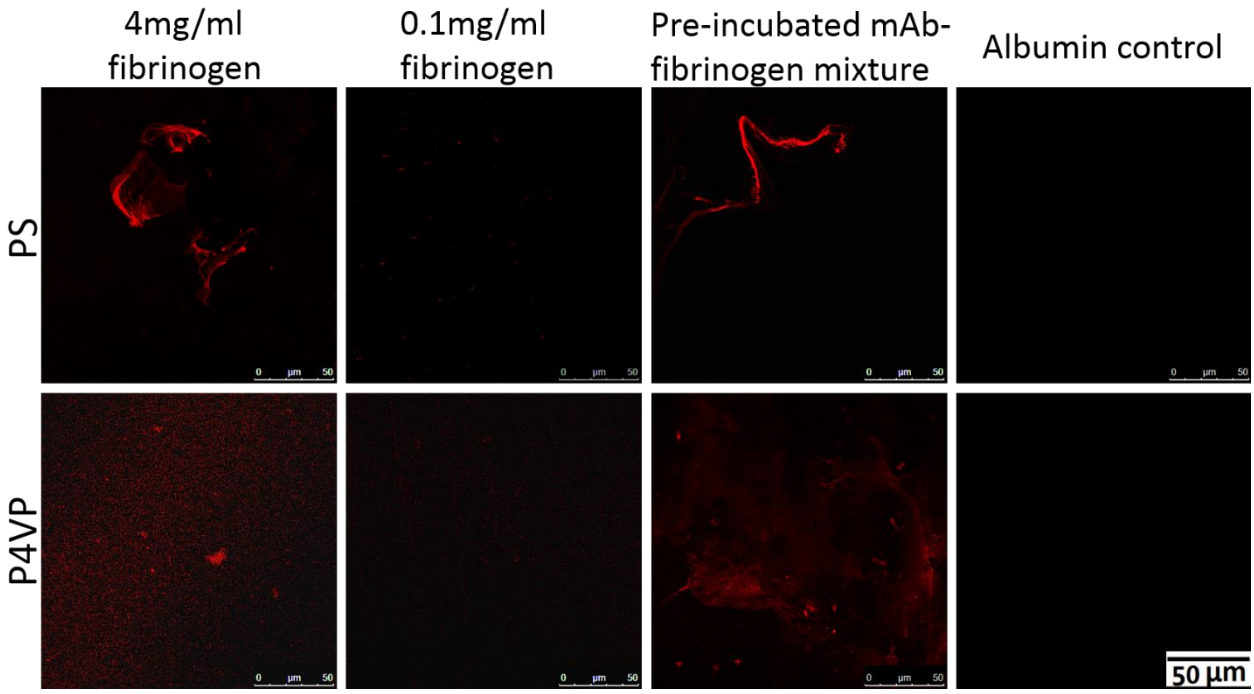

Figure 2.9 Confocal microscopy images of PS and P4VP spun cast thin films pre-incubated with the two fibrinogen concentrations shown, 12 h. To visualize images the plates were first exposed to anti-fibrinogen gamma chain 86-411 mAb, and then to Alexa Fluor 594-conjugatede anti-mouse IgG. Pre-incubated mAb-fibrinogen mixture samples are polymer substrates incubated with mixed 4mg/ml fibrinogen and primary antibody solution for 12h, then stained with secondary antibody. Albumin controls are polymer substrates incubated with 4mg/ml BSA for 12h, then stained with same primary and secondary antibody.

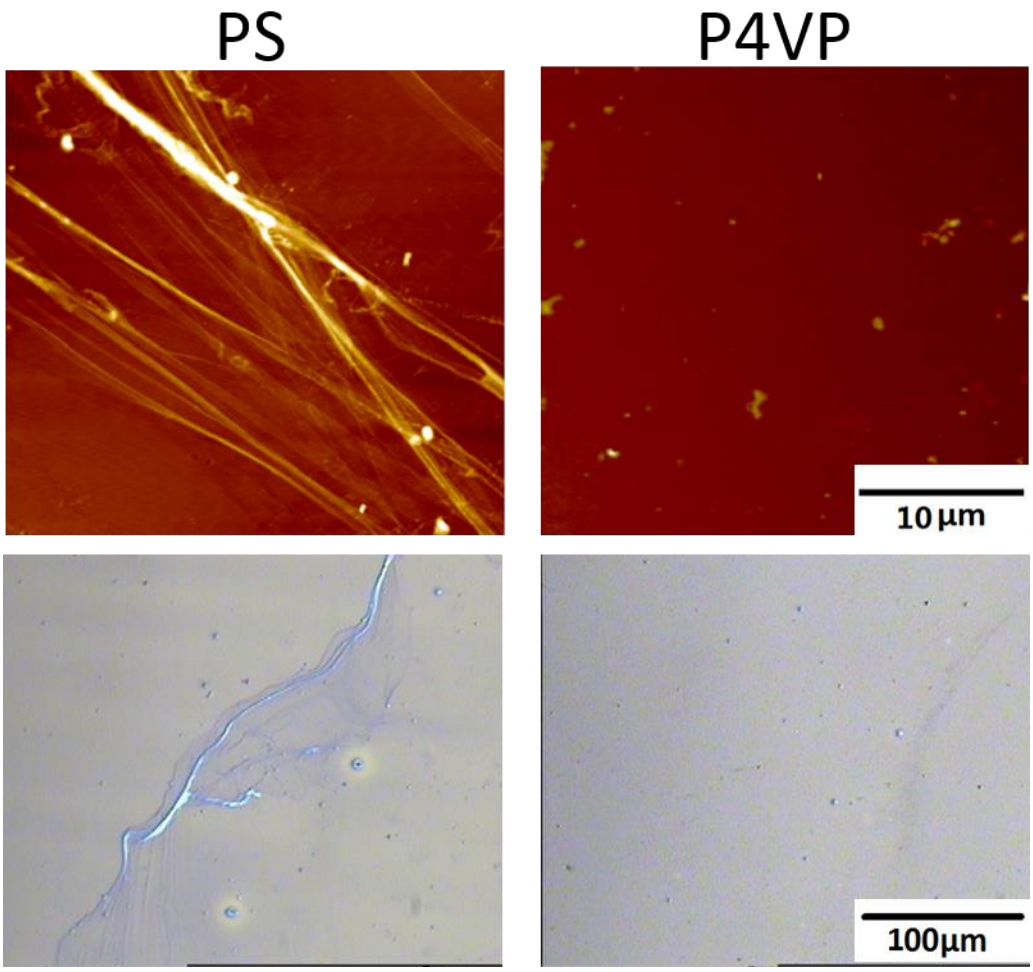

Figure 2.10 SPM (upper panels: Z scale 0-300nm) and optical microscope (lower panels) images of PS and P4VP surfaces incubated with whole plasma for 12h.

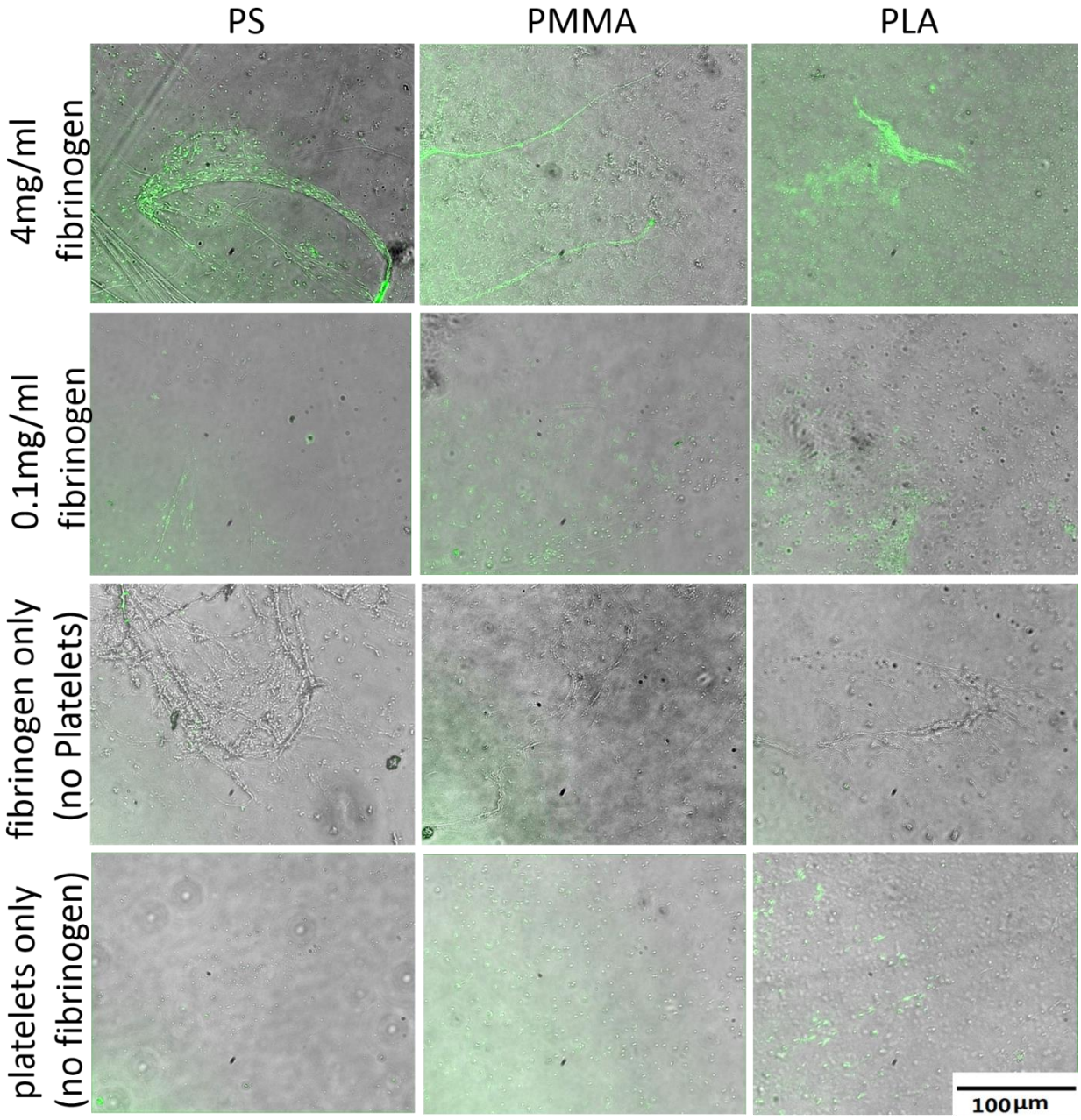

Figure 2.11 Fluorescence microscope images of platelets stained with CD41-FITC antibody superimposed on optical microscope images. The surfaces consisted of polymers spun cast on micro cover glass, pre-incubated in two different fibrinogen solutions, 4mg/ml and 0.1 mg/ml, for 12h, washed, and then incubated with platelets under static conditions, for 1h. Surfaces not incubated with platelets or fibrinogen were used as control.

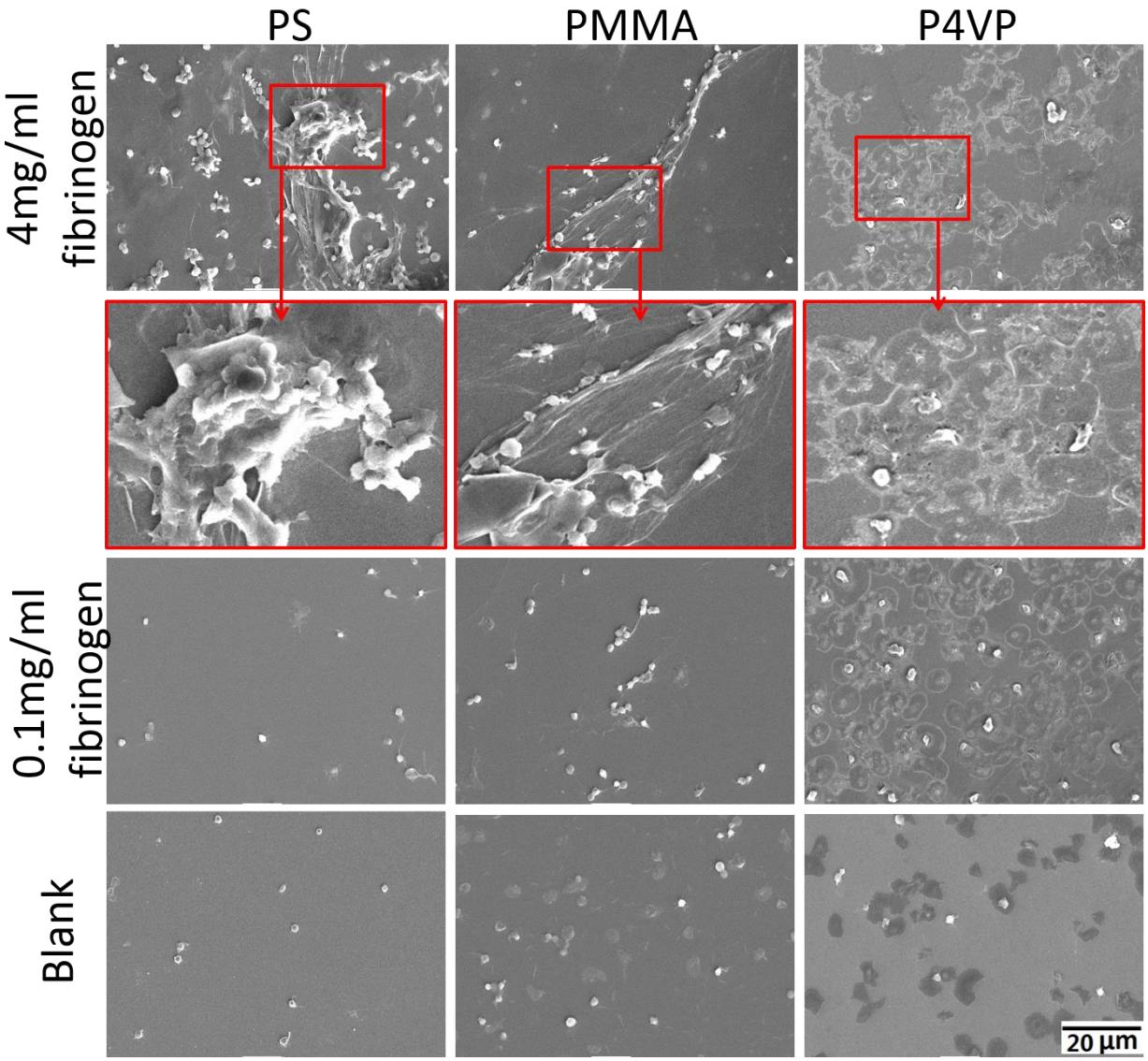

Figure 2.12 SEM images of PS, PMMA, and P4VP surfaces, pre-incubated with the two concentrations of fibrinogen for 12h, and then exposed to platelets under static conditions for 1h.

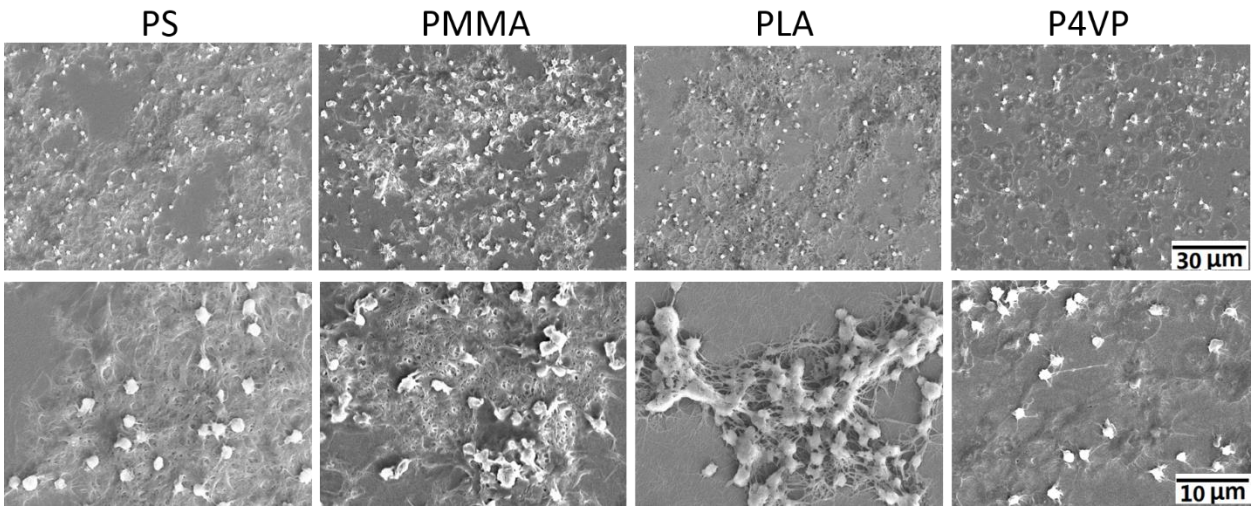

Figure 2.13 SEM images of undiluted PRP exposed for 1h to PS, PMMA, PLA, and P4VP that had been pre-incubated with fibrinogen 4mg/ml.

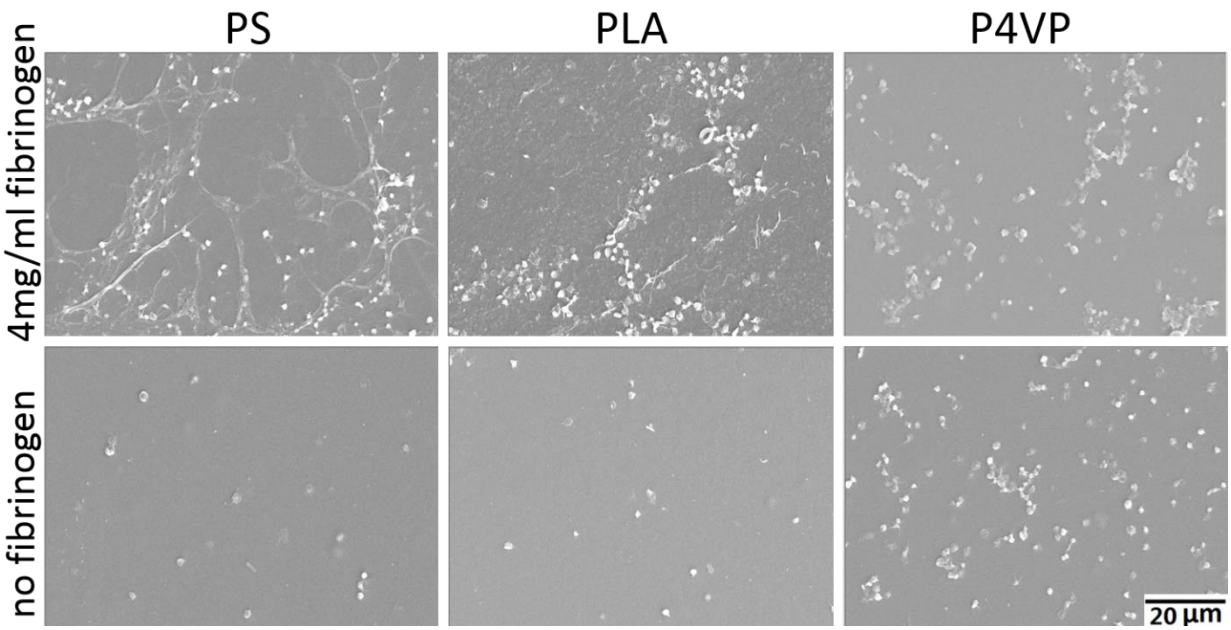

Figure 2.14 SEM images of PS, PLA, and P4VP pre-incubated with 4mg/ml fibrinogen for 12h, and then exposed to with platelets for 1h under flow conditions in the apparatus shown in figure 5a.

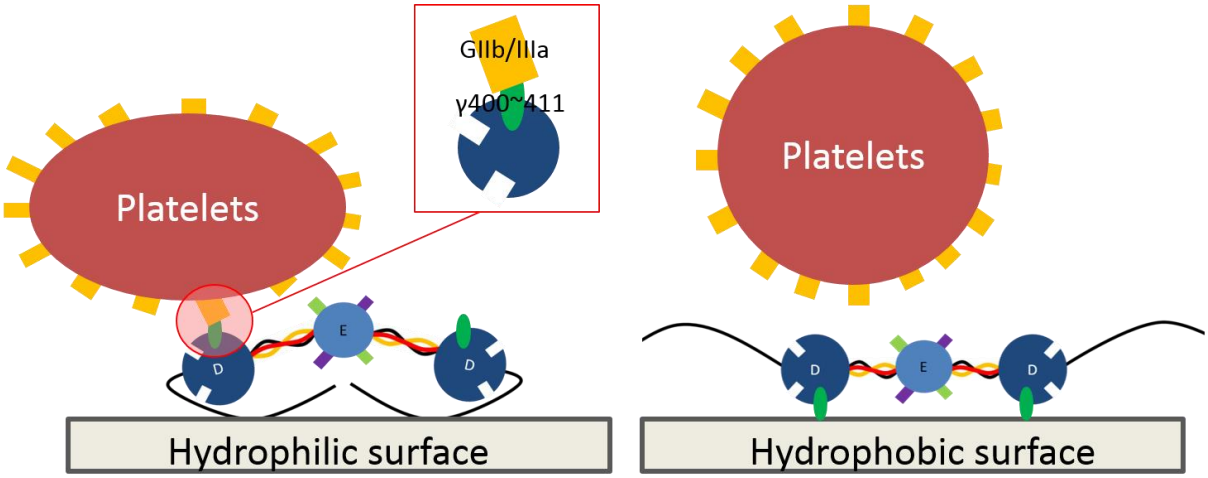

Figure 2.15 Schematic illustrating the orientation of the fibrinogen molecules adsorbed on hydrophilic and hydrophobic surfaces. On the Hydrophilic surface, the αC region is preferentially surface adsorbed, thereby exposing the D and E domain, which contains the platelet binding sequence, as shown in the inset. On the hydrophobic surface, the D and E domains are preferentially adsorbed, thereby releasing the αC regions which are not available to recruit other molecules or soluble fibrin segments. Hence the platelet binding domains are not available, while those fore recruitment of fibrin into larger fibers is exposed.

Table 2.1 Water contact angle values on the coated surfaces.

Polymer	Tg	Tm	Substrate	Water Contact Angle (mean ±s.d. n=6)
PS	100 ℃	240 ℃	Si Wafer	91 ±1 °
PS	100 ℃	240 ℃	Glass	89 ±1 °
PS	100 ℃	240 ℃	Kapton film	90 ±2 °
PMMA	105 ℃	160 ℃	Si Wafer	69 ±1 °
PMMA	105 ℃	160 ℃	Glass	70 ±1 °
PMMA	105 ℃	160 ℃	Kapton film	70 ±1 °
PLA	60 ℃	173 ℃	Si Wafer	71 ±1 °
PLA	60 ℃	173 ℃	Glass	70 ±1 °
PLA	60 ℃	173 ℃	Kapton film	71 ±2 °
P4VP	137 ℃	260 ℃	Si Wafer	56 ±2 °
P4VP	137 ℃	260 ℃	Kapton film	55 ±2 °

Chapter 3: Evaluation of composition, mechanical properties, and biocompatibility of Gutta-percha

3.1 Introduction

Root canal therapy is the most common endodontic procedure used for preserving a tooth without the need of an invasive surgery or a dental implant [58]. It involves the removal of infected dental pulp, the subsequent shaping, cleaning the hollows, and the obduration of the decontaminated canals with an inert filling such as Gutta-percha [59]. Gutta-percha is a partially crystalline and viscoelastic polymeric material that contains the molecule trans-1,4-polyisoprene (PI). The average molecular weight of PI in Gutta-percha was found to be about 42,000 and covers a narrow polymeric range [60]. Because of the low melting point of PI, inorganic fillers are added for commercially used Gutta-percha cones to provide mechanical properties. Varying the volume fraction of filler allows for control of the thermomechanical properties, and protection against infection of the canal since many metal oxides are anti-bacterial. Composition of commercially used Gutta-percha points varies according to manufacturer, with a composition of about 14-23% Gutta-percha serving as a matrix; 45-78% zinc oxide used for its antimicrobial and cost cutting properties; 2-37% heavy metal salts employed for their radiopacity; and 1-8% waxes or resins used to increase plasticity of the final product [61-63].

Some clinicians choose the brand of Gutta-percha depending on the technique being used [64]. In this research, we evaluated three different kinds of Gutta-percha obturators used for different

endodontic techniques: uncrosslinked Protaper™ and Lexicon™, and crosslinked Guttacore™. For uncrosslinked obturators, endodontists will bend or heat them prior to usage in a root canal procedure to allow for increasing flexibility and allow for smooth insertion into the root canal orifice. The heat technique may not be favorable because melted Gutta-percha undergoes a large amount of shrinkage, which may result in productive locations for bacteria to re-contaminate the root canal region [65]. On the other hand, Guttacore™ is a gutta-percha-based core-carrier system with a crosslinked thermoset carrier and uncrosslinked 3-dimensionally Gutta-percha coating. It allows the movement of softened Gutta-percha in all directions within the root canal system and will be removed more easily during retreatment [66, 67]. The problem of Guttacore™ is the brittle carrier cannot be bent prior to placement, as a clinician might wish to do in difficult canal access, may cause uneven or inaccurate breaks when using [67].

The strength of Gutta-percha obturators derived dental materials has been found to have a direct correlation with efficiency [66]. There are few studies on the shear modulus of melted Gutta-percha obturators with regards to the warm Gutta-percha techniques [65], and comparison of Young's modulus of warm and cold Gutta-percha [68]. Furthermore, there are not enough reliable and consistent data with respect to the strength of current Gutta-percha obturator products, including noncrosslinked regular Gutta-percha points and crosslinked core-carrier system. In addition, the spatial distribution of the nanoparticles in Gutta-percha obturators, which is also critical to the performance of the Gutta-percha obturators, has not been studied in depth. The evaluation of particle distribution will help us to fully understand the structure-property relationship of the materials and to make valuable suggestions for endodontic use.

Bacterial infection is always a big issue in root canal therapy [69]. Zinc Oxide is claimed by manufacturers as an anti-bacterial filler in Gutta-percha obturators. However, according to

previous research, regular Gutta-percha cones did not inhibit any of the microorganisms tested [70]. Furthermore, many researchers have been looking for materials to use in dental pulp regeneration, which not only cleans and fills the pulp chamber but also allows regeneration of live tissue in it [71]. Some materials, such as poly (lactic-co-glycolic), poly (ι -lactic acid), poly (ε -caprolactone), gelatin hydrogels, and hydroxyapatite/tricalcium phosphate ceramic, have been reported as potential scaffolds for in tooth regeneration based on their ability to promote/allow in *vivo* and *in vitro* DPSC differentiation with dexamethasone [8, 72-75]. However, the use of chemical inducers such as dexamethasone corticosteroid, can cause adverse side effects such as hyperglycemia and a weakened immune system when applied *in vivo* [76]. Our previous research indicated that the enzymatically crosslinked gelatin hydrogels are extremely effective substrates for DPSCs osteo/odontogenic differentiation even in the absence of dexamethasone [7]. Therefore, we explore in this chapter whether Gutta-percha can also be an appropriate material for delivery of dental pulp stem cells and encouraging their differentiation without additional factors. Many *in vitro* studies demonstrated that Zinc Oxide nanoparticles are cytotoxic [77, 78]. Since it's the main filler in Gutta-percha products, research have been done on evaluating cytotoxicity of Gutta-percha obturators *in vitro*. Pascon and Spangberg showed that fourteen commercially available Gutta-percha points tested were toxic after 24 h incubation, and the toxicity was attributed to leakage of zinc ions into the fluids [79]. Gambarini *et al.* did research on some new root canal filling materials including the core-carrier system, none of which exhibit cytotoxicity [80]. However, there is insufficient research on long period cytotoxic effects of Gutta-percha obturators and their potential of regeneration of tooth.

Therefore, we performed a detailed characterization of three Gutta-percha materials: uncrosslinked ProTaper™ Lexicon™, and crosslinked Guttacore™. We used SEM-EDAX and

TGA to determine the nature and size of the fillers, and used X-ray computed microtomography (CMT) to determine the internal distribution of the particles and then correlate the results with mechanical measurements, tensile test and DMA. Comparison of Gutta-percha obturators before and after being worked was also carried out. In addition, antimicrobial tests were conducted, and culture of DPSC was performed to determine the interaction of the Gutta-percha obturators with dental tissue present inside the canal.

3.2 Experimental Section

3.2.1 Materials

The Gutta-percha used in this research were: ProTaper™ (DENTSPLY International, Inc., Johnson City, TN), Lexicon™ (DENTSPLY International, Inc.), and Guttacore™ ((DENTSPLY International, Inc.). ProTaper™ and Lexicon™ are regular Gutta-percha cones, while Guttacore™ is a core-carrier system. Components of Guttacore™ were shown in Figure 3.1. It includes grey core carrier part and outside pink coating part. All three materials in this study, Guttacore™, ProTaper™, and Lexicon™, consist of an elastomeric polymer matrix, PI, loaded with inorganic particles.

3.2.2 Mechanical manipulation

The Lexicon™ and ProTaper™ filaments were softened at room temperature by flexing and extending the filaments at a rate of 0.5Hz for two minutes. Guttacore™ was too brittle and did not soften.

3.2.3 Scanning electron microscopy and energy dispersive analysis X-ray (SEM/EDAX)

In order to analyze the actual morphology and composition of the particles in the Gutta-percha, the outside surface of the sample, as well as a cross section showing the inner surface (shown in Figure 3.2(a)) were sputtered with gold. A LEO/Zeiss 1550 field emission SEM (Minnesota, USA) at 20KeV accelerating voltage using Robinson type backscattering electron detectors. The elemental compositions of the samples were determined using energy dispersive X-ray microanalysis (EDAX) (Phoenix XEDS system).

3.2.4 Thermal gravimetric analysis (TGA)

Thermal Gravimetric Analysis (TGA) was performed to analyze the percent of filler in ProTaper™, Lexicon™, and each component of Guttacore™: the carrier core and the coating. All the samples were examined from room temperature to 800 ℃ at a frequency of 1 Hz with a heating rate 10 ℃ /min. A TGA (Mettler-Toledo International Inc., Columbus, OH) was used in conjunction with STARe Thermal Analysis Software to plot the results. All the samples were normalized for accurate comparisons between the various samples run.

3.2.5 X-ray computed microtomography (CMT)

X-ray computed microtomography measurements (CMT) were carried out at the Brookhaven National Synchrotron Light Source X2B beamline. The x-rays passing through the sample were detected with a CsI (Tl) scintillator observed with a 140 x 1300 pixel charge-coupled (CCD) camera. The effective pixel size following magnification with a 2.5 X lens was 7.6 μm. The attenuation of the x-rays by the sample was measured as the sample rotated through 180 º. Step sizes of 0.15 ºand 1 ºwere used. The beam energy was adjusted to the specific samples investigated and were in the range of 30 KeV. The data was reconstructed to give 3D volumes using the tomo display software (M. L. Rivers.

http://cars9.uchicago.edu/software/idl/tomography). The visualization and analysis of the results were performed with the ImageJ software.

3.2.6 Mechanical properties analysis

Tensile properties of Gutta-percha were determined using an Instron Tensile Tester (Model: 5524) with a 500N load cell and hydraulic pressure grip in compliance with ASTM D638. The dimension of samples were measured before test using a caliper. For Guttacore™, the coating was removed to solely test the carrier's core. For each composition, five specimen were tested with a constant speed 1mm/min.

3.2.7 Preparation of thin film surfaces

Hydrophobic Si wafers were prepared as described in chapter 2. Spun-cast films were: ProTaper™, Lexicon™, outside pink coating of Guttacore™ dissolved in chloroform (VWR International, Plainfield, NJ), and polyisoprene (PI) (Mw=803,000, polydispersity index=1.36, from Scientific Polymer Products, Ontario, NY) dissolved in the toluene (Sigma-Aldrich, St. Louis, MO). All the solutions were spun cast onto the substrates at 2500rpm for 30s. The thickness of the layers was measured by ellipsometry (Rudolph Technologies, Flanders, NJ). Polymers films were then annealed at 130 ℃ in a vacuum of 10^{-3} Torr overnight to remove the residual solvent, sterilize, and relax strains induced by the spinning process.

3.2.8 Zone exclusion antimicrobial activity and efficacy test

ProTaper™ and Lexicon™ samples were prepared both by spin casting from solutions as 38mm ×38mm square and molded as 29mm diameter disk. PI was also prepared by spin casting 38mm ×38mm square thin film as control sample. 10 μl enterococcus faecalis was sandwiched between

two layers of 38x38cm spun cast films and incubated for 24h. The surfaces were then rinsed to remove bacteria and the solution was re-plated to form colonies. The number of bacterial colonies was counted the following day.

3.2.9 Cell isolation and cell plating

Human dental pulp stem cells (DPSC) strain AX3 were obtained from Dr. Marcia Simon, Department of Oral Biology and Pathology, School of Dental Medicine, Stony Brook University, NY, USA, previously isolated from extracted wisdom teeth under an approved protocol (IRB#20076778). For use cells were cultured in "base medium": alpha Minimal essential medium (α-MEM) (Catalog # 12571, GIBCO, Invitrogen, Carlsbad, CA, USA) supplemented with 10% fetal bovine serum (FBS) (GIBCO, Invitrogen), 100 units/ml penicillin/100 µg/ml streptomycin (GIBCO, Invitrogen), 200 µM L-ascorbic acid 2-phosphate (Sigma Aldrich), and 10mM β-glycerol phosphate (Sigma Aldrich). Osteogenic induction of the DPSCs was achieved by addition of 10^{-8}M dexamethasone (Dex) (Sigma Aldrich) to the "base medium" as "induction medium". The DPSCs were grown in a humidified incubator at 37°C with 5% CO_2. Culture medium was refreshed every alternate day.

DPSCs were seeded onto Gutta-percha and PI coated Si surfaces at a density of 10,000 cells/cm^2. The number of DPSCs grown in "base media" was counted on day 3, 6, 9, 12 and 15 by hemacytometer (Hausser Scientific). For the differentiation experiments, half of the samples were cultured with the "base medium" and the other half with the "induction medium". On day 21 after cell seeding, all the samples were taken out of incubator and left overnight at room temperature to get rid of live cells. Then the samples were washed with deionized water twice to remove soluble salts from media and then left for air-drying at room temperature till they got dehydrated. The

specimens were sputtered with gold, and the surface morphologies and elemental compositions of deposits on all the substrates were examined using SEM/EDAX.

3.2.10 Confocal laser scanning microscopy

Immunocytochemistry was used to stain actin filaments and nuclei. The DPSCs were washed with phosphate buffered saline (PBS) (pH=7.4, Ca, Mg-free), fixed with 3.7% (w/v) formaldehyde (Boehringer Mannheim Corp., USA), permeabilized with a mild detergent (0.4% Triton X100 in PBS), stained with Alexa Fluor-488 Phalloidin (Molecular Probes, Eugene, OR) for actin and Propium Iodide (Molecular Probes) for the nucleus. All the surfaces were rinsed and stored in PBS. Samples were then imaged using a Leica TCS SP2 laser scanning confocal microscope (Leica microsystem Inc., Bannockburn, IL) to visualize actin cytoskeleton organization and the morphology of the cells on days 3 and 6.

3.3 Results

3.3.1 Gutta-percha composition

We first examined the exterior surfaces of the three types of Gutta-percha using Scanning Electron Microscopy with Energy Dispersive Analysis X-ray (SEM-EDAX). The Gutta-percha cones were sliced as illustrated in Figure 3.2(a) and typical segments of the inner and outer surfaces were examined. In all cases the images were found to be very similar, indicating that the materials were uniform in composition. The images, together with the associated EDAX spectra are shown in Figure 3.2(b). The Lexicon™ and ProTaper™ samples consist of micro-bar shaped ZnO particles, approximately of approximate dimensions, 200~400nm, which are densely packed together into a sheet held together by the minority polymer component. In addition to ZnO, ProTaper™ also contains a small fraction of $BaSO_4$ particles, for enhancing the X-ray

contrast. The $BaSO_4$ particles are significantly larger (approximately two or three times the volume) and are easily seen above the ZnO particle sheets. The morphology of the Guttacore™ material is less structured. The filler distribution in the coating component (surface) was composed mostly of close packed ZnO nanoparticles and a small fraction of $BaSO_4$ particles. The carrier component (cross section) consists of large micron scale irregularly shaped WO_3 particles and cubic $CaCO_3$ particles, embedded in a polymer layer with finely dispersed TiO_2 nanoparticles.

In order to determine the particle to polymer mass ratios, TGA was performed and the results are shown in Figure 3.3(a) where we plot the percent weight loss of each of the three samples as a function of heating temperature. In Figure 3.3(b) we plot the derivative of the function in Figure 3.3(a) in order to determine the decomposition temperatures of the different components in the materials and in Figure 3.3(c) we plot the weight fractions of the organic and inorganic components.

From Figures 3.3(a) and 3.3(b) we can see that ProTaper™ has two distinct transition temperatures where abrupt weight loss occurs at $T=400^{o}$ C and $T=600^{o}$ C. The first transition corresponds to the decomposition of PI, while the second corresponds to that of $BaSO_4$ [81] from which we can deduce that this material is composed of 1, 1, and 2 weight fractions of PI, $BaSO_4$, and ZnO in agreement with the SEM-EDAX images. In the case of Lexicon™ we find a similar initial weight loss at 400 ℃ corresponding to the PI matrix fraction and a decrease around 600 ℃ of a component with a weight fraction of less than 10%. Hence this material contains less PI and a much larger fraction of inorganic ZnO particles. Since we cannot find evidence of $BaSO_4$ or any other high Zn material other than ZnO, we can only conjecture that this fraction represents a layer of organic material which may have been tightly adsorbed to the inorganic particles and

hence decomposes at a higher temperature. The Guttacore™ carrier has a relatively complex decomposition pattern, reflecting the complex internal particle structure. The nanoscale TiO_2 particles are well dispersed and hence strongly adsorbed to the PI matrix, increasing the decomposition temperature by ~50 ℃. Multiple other peaks of components which comprise no more than 5-6% weight percent are also observed. The Guttacore™ coating on the other hand appears to be composed only of ZnO and PI, with the highest inorganic fraction of 89%.

3.3.2 Mechanical properties

The tensile properties of ProTaper™, Lexicon™ and Guttacore™ were measured and are plotted in Figures 3.4(a-d), where we show the stress-strain curves and the associated values of the toughness, Young's modulus, and the ultimate tensile strength. From the figure we can see that ProTaper™ and Lexicon™ have similar response functions, with relatively low moduli and relatively small elongation. Guttacore™ had a much higher modulus, but an even smaller amount of elongation. In order to increase the ductility both ProTaper™ and Lexicon™ were worked, as described previously. However, Guttacore™ was far more brittle and unable to be worked. In Figure 3.4(a) we can the dramatic increase in ductility of the same samples. From Figure 3.4(b-d) we can clearly see that after being worked for 2 min, both ProTaper™ and Lexicon™ show dramatic 3 and 4 fold, respectively, increase in elongation, and 4.5 fold increase in toughness. From the figure we can see that the ultimate tensile strength was not decreased, indicating that materials were becoming more flexible rather than weakening. Hence both ProTaper™ and Lexicon™ were more ductile after being manipulated. This effect is in contrast to that observed in metals and alloys, were manipulation and working of the samples increase the rigidity and modulus. In the case of metals the increased hardness is a result of migration of defects into the

area of deformation. In the case of amorphous polymer nanocomposites, internal migration and redistribution of the nanoparticles may affect the mechanical properties.

3.3.3 Particle distribution

In order to determine the three dimensional distribution functions, the Gutta-percha samples were analyzed using CMT. In Figure 3.5(a) we show a cross sectional scan obtained from a movie where the midsection of the Guttacore™ is imaged. From the figure we can clearly see the regions of the carrier and the coating components. From the SEM images we had seen that the particles in the carrier segment are relatively large (1-2 microns) and composed of W, Ti, and Ca, while the particles of the coating were much smaller and composed of ZnO and $BaSO_4$. Furthermore, the inorganic fractions were much higher, 89% vs 56%, in the coating than in the carrier. This can clearly be seen in Figure 3.5(d) where the values of the X-ray attenuation coefficient in the cross section are more uniformly distributed in the coating than the carrier. The coarse grained nature of the distribution of the carrier is also easily seen in the three dimensional projection shown in Figure 3.5(g). The ProTaper™ sample was also scanned and a cross sectional region is shown in Figure 3.5(b). The attenuation coefficient plotted in Figure 3.5(e) indicates that the distribution of particles is uniform, with a slight increase in density at the outer edges. The fine grained structure is also evident in the three dimensional projection shown in Figure 3.5(h). In Figure 3.5(c) we show a cross sectional region of the same ProTaper™ sample after it was worked. From the figure we see a large stripe of low density spanning the entire cross section. A series of these regions can be seen across the entire sample in the video images in the supplementary section. The attenuation coefficient across the scan of the diameter of section shows that the density is decreased by nearly 30% in the striped sections (Figure 3.5(f)). The magnified three dimensional scan shown in Figure 3.5(i) also shows that in addition to the

decreased density stripe, a coarsening of the particle distribution also occurred within the sample indicating a larger scale redistribution of the particles occurred to accommodate the low density region. Since these low density stripes appear only after repeated flexing of the sample, we attribute them to redistribution of the particles away from the region of the bend as a result of internal stresses in the polymer. These areas become larger with increased working and result in an overall softening of the composite, at constant ambient temperature.

3.3.4 Toxicological effects of Gutta-percha

EDAX results in Figure 3.2 confirmed the manufacturer's description that ZnO is the main filler of Gutta-percha obturators. It is well established that ZnO nanoparticles are cytotoxic. Although the nanoparticles may be encapsulated with PI on the surface, the contact of the material with fluids in the oral cavity may result in dissolution of the nanoparticles, and, chloroform used in endodontics for plasticizing Gutta-percha points and for facilitating removal of Gutta-percha root canal fillings in need of re-treatment may made ZnO available. We therefore dissolved the ProTaper™, Lexicon™, and the outside pink coating of Guttacore™ in chloroform and spun cast onto hydrophobic Si wafers to evaluate biocompatibility. PI coated Si water substrate was used as a control material. The surface morphology was imaged using SPM and SEM-EDAX. Lateral scans of SPM in Figure 3.6 indicate that the particles are coated with a soft material. The lack of contrast indicates that the same material covers particle and matrix, is most probably PI. From the results shown in Figure 3.6 and 3.7, we can see that Gutta-percha obturators are loaded with high fraction of nanoparticles. Particle size is approximately 200nm in height and 1μm in diameter, with aggregates of several microns in diameter. The SEM-EDAX in Figure 3.7 is consistent with that of bulk samples shown in Figure 3.2. The SPM and SEM-

EDAX of Gutta-percha coated Si surfaces further confirm the high degree of loading and stated chemical compositions.

ZnO is also argued as anti-bacterial filler in Gutta-percha obturators. Thus, zone exclusion antimicrobial activity and efficacy test was performed and results shown in Figure 3.8 (a). PI spun coated Si surface was used as a control material. We can clearly see that ProTaper™ and Lexicon™ spun cast into thin films or heat press molded as bulk samples, are not significantly anti-bacterial. The bacteria remained after 24 h incubation on molded substrates are almost at the same level as the beginning concentration. The spun cast Gutta-percha samples had a little bit lower bacterial concentration than molded ones possibly due to the exposure of ZnO nanoparticles. The calculation of the value of antimicrobial activity is:

$$R = [\log_{10}(B/A) - \log_{10}(C/A)] = \log_{10}(B/C) \quad (1)$$

Where, R: value of antimicrobial activity

A: average of the number of viable cells of bacteria immediately after inoculation on the untreated test piece

B: average of the number of viable cells of bacteria on the untreated test piece after 24h

C: average of the number of viable cells of bacteria on the antimicrobial test piece after 24h

According to the JIS Z 2801, the value of antimicrobial activity of this Standard should not be less than 2.0 for the antimicrobial efficacy of antimicrobial products. However, the value of all the test Gutta-percha samples was less than 2.0. The result indicates that these Gutta-percha obturators are not effective as an anti-bacterial agent.

Cytotoxcicity was probed using DPSC seeded at an initial density of 10,000/cm^2 on spun cast films. The cell proliferation curve and doubling time calculation are shown in Figure 3.8 (b, c). From the figure we find that when compared to the PI control, the proliferation curves on the Gutta-percha samples first show a lag region where the proliferation rate is slower, but then the culture recovers and proliferates at nearly the same rate as the control. And there is no significant difference of doubling time between all Gutta-percha samples and the control sample. The result is consistent with confocal microscopy images at days 3 and 6 in Figure 3.9. At day 3, the DPSCs were well spread on the PI control, but not on any of the Gutta-percha substrates. However, at day 6, the cells recovered, and their morphology shows well defined actin fibers and good tissue formation. These results are in sharp contrast to those obtained when ZnO particles are added directly into the cell culture media. In Figure 3.10 we show that concentration as small as 0.05mg/ml was cytotoxic.

The ability of the DPSC to differentiate on these substrates was also probed. Cells were incubated in cultures with and without dexamethasone, which is known to induce osteogenic differentiation [7]. After 21 days the samples were examined with SEM-EDAX and the results are shown in Figure 3.11. From the figure we can see that the cultures with added dexamethasone produced biomineralized deposits, which EDAX confirmed as being HA. Hence Gutta-percha does not interfere with the standard differentiation process. On the other hand, it's interesting to note that differentiation, as defined by deposition of biomineralized HA products, was also observed on all Gutta-percha samples, without dexamethasone. Hence we can conclude that Gutta-percha is neither anti-bacteria nor cytotoxic and may promote DPSC differentiation in the absence of additional chemical factors.

3.4 Discussion

As a reconstruction technique, CMT could be used as a tool to explore root canal anatomy and detect fractures in it [82, 83]. Here we used it for reconstruction of Gutta-percha in order to investigate the internal distribution of the nanoparticle. Prior to working the results indicate a remarkably uniform distribution despite the high degree of loading. Working the filaments results in a redistribution of the particles, where the particle concentration in the region of the bend is decreased resulting in a significant increase of the overall ductility. These results could be explained by the Mullins effect which was first demonstrated in carbon reinforced rubber composites. When a strip of it was extended to a given elongation, returned to zero strain, and subsequently extended again, stress softening was observed [84]. This well-known phenomenon, frequently referred to as the "Mullins effect" or "Mullins softening", is a viscoelastic effect, although in filled rubber there can be additional contributions to the mechanical hysteresis from filler particles de-bonding from each other or from the polymer chains [85]. One of the well-known models is the internal slipping of the macromolecular chains and sliding of the connecting chains on the reinforcing filler particles [86]. Our working of the Gutta-percha obturator was similar to the cycled force loading of Mullins effect, since we kept bending the obturator at a steady frequency for 2min. Also, our previous research showed that nanoparticles could stabilize a polymer system, as the particles move towards edge of the holes when they appeared on the dewetting polymer thin film [87, 88]. There was also report on nanoparticle rearrangement under shear stress in a nanoparticle filled polymer system [89]. Thus, our model of working Gutta-percha obturator is the schematic shown in Figure 3.4 (e). Before working, the polymer chains are uniformly tangled around randomly distributed nanoparticles. After being worked for 2min, hard filler and soft polymer domain microstructure of the system are rearranged. The polymer chains are stretched and the nanoparticles aggregate to form a soft pure polymer domain in

between. Baeza *et a*l. found that in filler reinforced polymer nanocomposite systems, increasing the volume fraction of fillers will lead to higher mechanical properties, due to the aggregation of the nanoparticles and formation of the pure polymer zones in low filler density system [90]. Thus, after being worked for 2min, the polymer-nanoparticle system becomes softer and is able to elongate through the stretch of pure polymer domains.

Here we show that Gutta-percha materials may also be suitable for tooth regeneration. In addition to imparting mechanical strength, the choice of ZnO nanoparticles is to provide anti-bacterial protection. Since these materials are used primarily for obduration, there was little concern regarding the impact of ZnO on the living cells in the pulp. The lack of toxicity observed when the cells were plated directly on the spun cast films was consistent with SPM scans of the surface which indicated that the polymer coated the particles, preventing them from contacting or penetrating the cells. This observation was also consistent with the lack of anti-bacterial activity. On the other hand, the increased mechanical properties and surface roughness appear to be contributing factors in the induction of DPSCs differentiation without additional chemical induction factors.

3.5 Conclusion

We have demonstrated that CMT is able to map the internal particle distribution of Gutta-percha filled systems and show that regions of decreased particle density are formed as a result of mechanical working of the material. The formation of these regions can be explained by the Mullins effect, predicts redistribution of the particles as a consequence of internal chain slipping, which results in stress softening of the material. The ZnO particles used in the Gutta-percha materials tested were encapsulated and hence the material was not cytotoxic or anti-bacterial.

The mechanical strength and roughness imparted by the particles contributed to promoting differentiation and biomineralization of DPSCs placed in contact with the material surfaces. These results indicate that in addition to obduration, Gutta-percha materials ProTaper™, Lexicon™, and Guttacore™ may also be used for tooth regeneration.

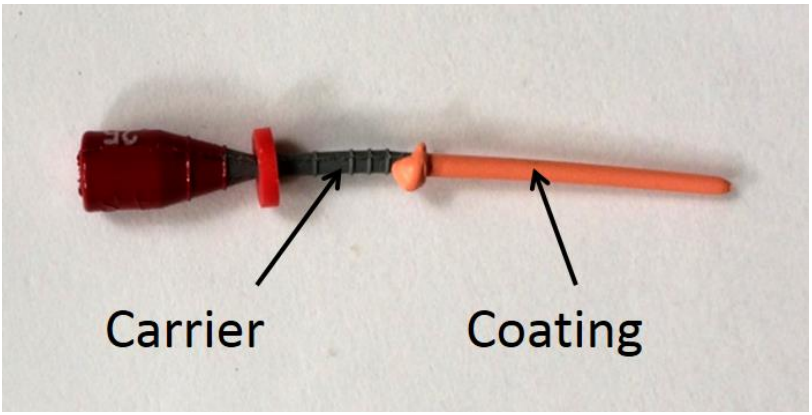

Figure 3.1 Guttacore^{TM} obturator components, including carrier part and coating part.

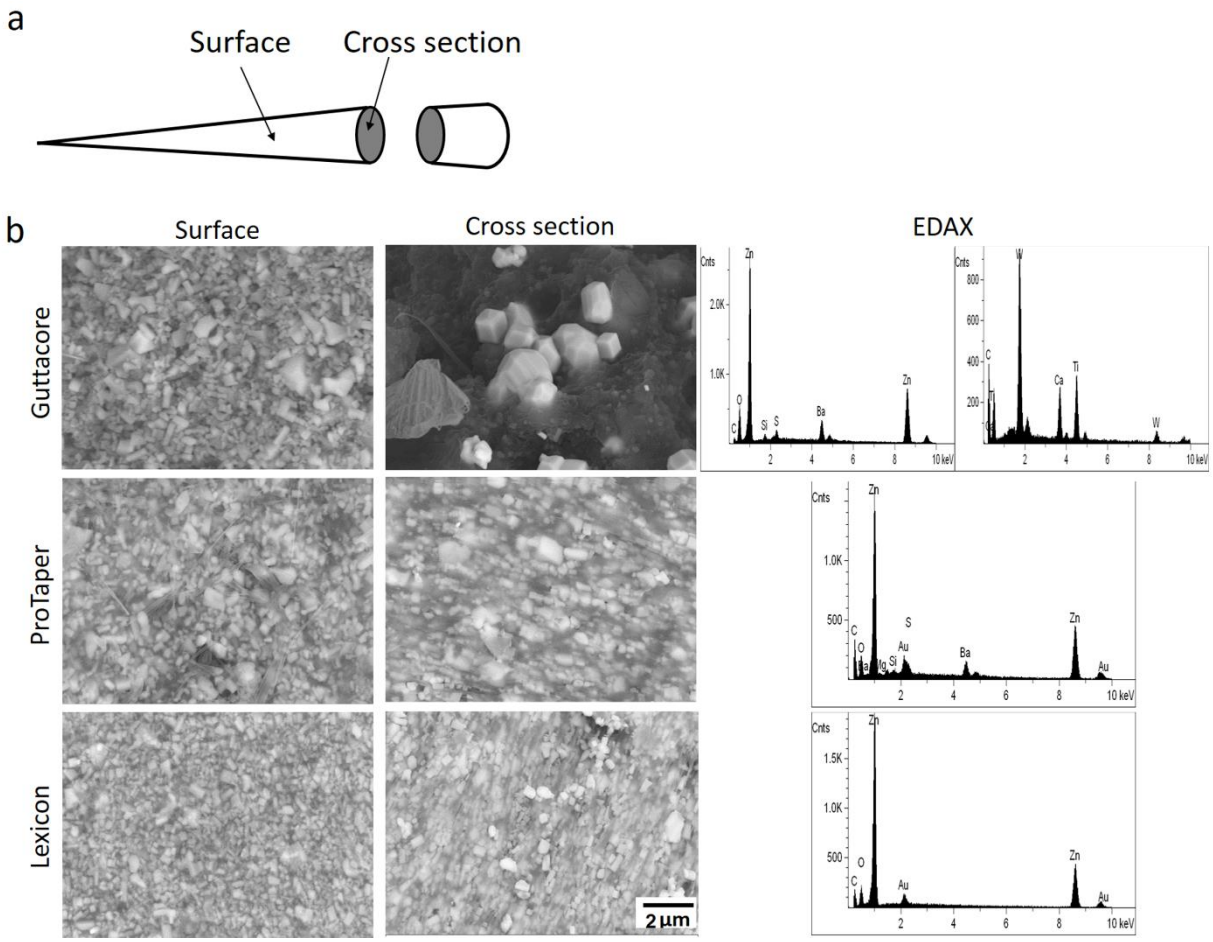

Figure 3.2 (a) A diagram of the outside surface and cross section showing the inner surface of a typical Gutta-percha sample for SEM-EDAX, (b) SEM-EDAX comparison of Gutta-percha obturators surface and cross section: Guttacore™ (the surface and cross section refer to coating and carrier components respectively), ProTaper™, and Lexicon™.

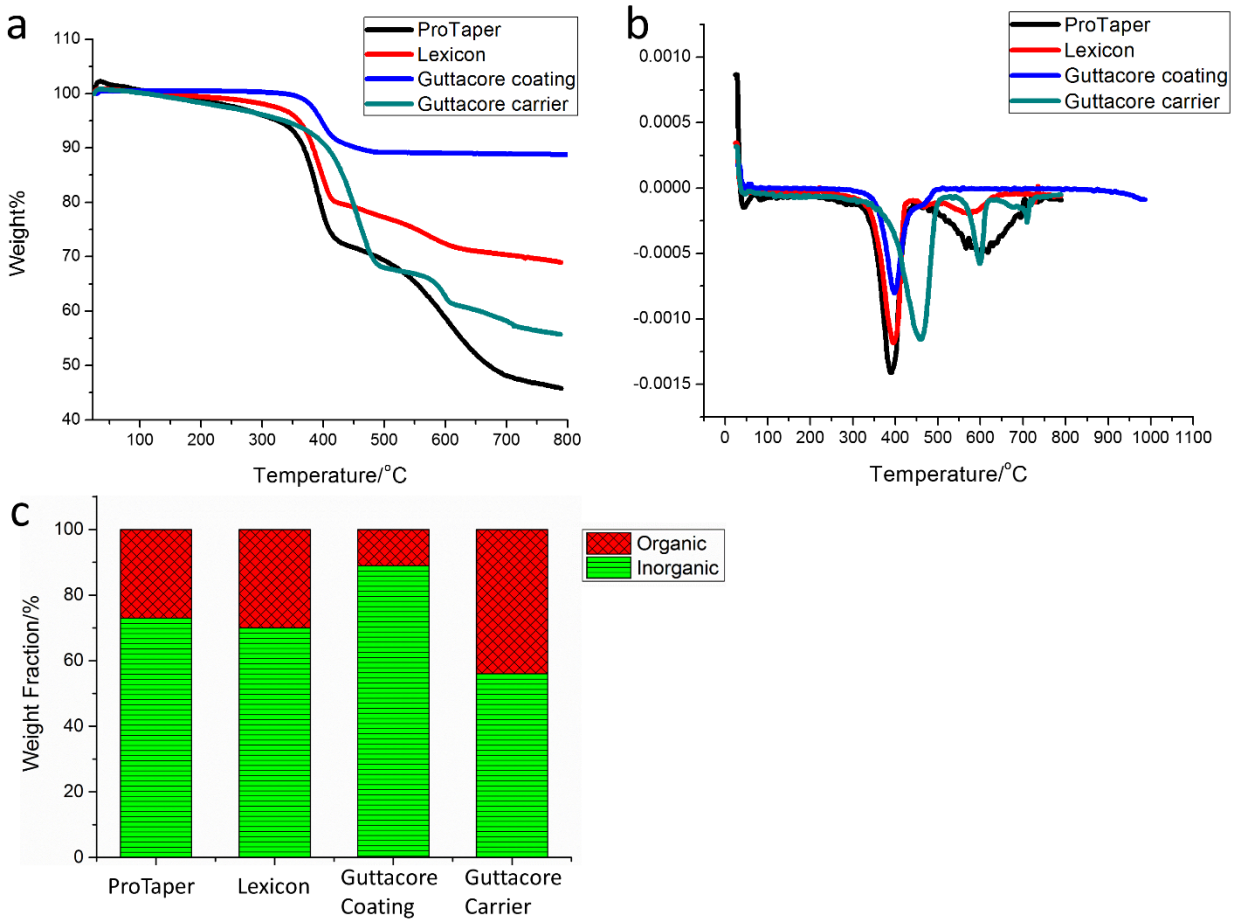

Figure 3.3 (a) TGA curves of ProTaper™, Lexicon™, Guttacore™ coating, and Guttacore™ carrier. All the samples were normalized using starting weights and heated to 800 ℃ at a heat rate of 25 ℃/min. (b) 1st derivative of TGA curves, (c) weight fractions of organic and inorganic components.

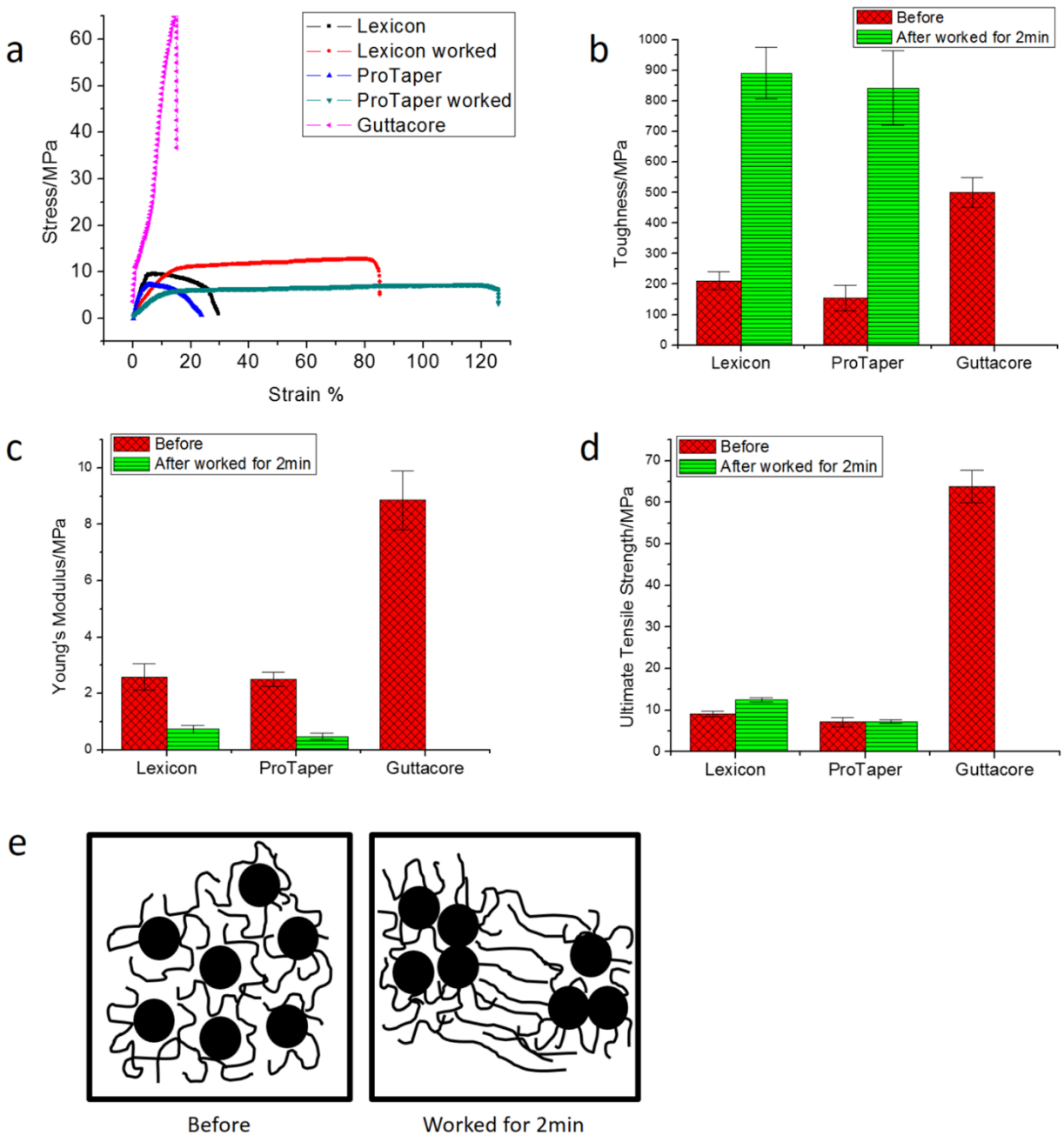

Figure 3.4 Mechanical properties of ProTaper™, Lexicon™, and Guttacore™. (a) Stress-strain curves, (b) Toughness, (c) Young's modulus, (d) Ultimate tensile strength, and (e) Schematic illustrating distribution of particles in ProTaper™ and Lexicon™, before and after worked for 2min.

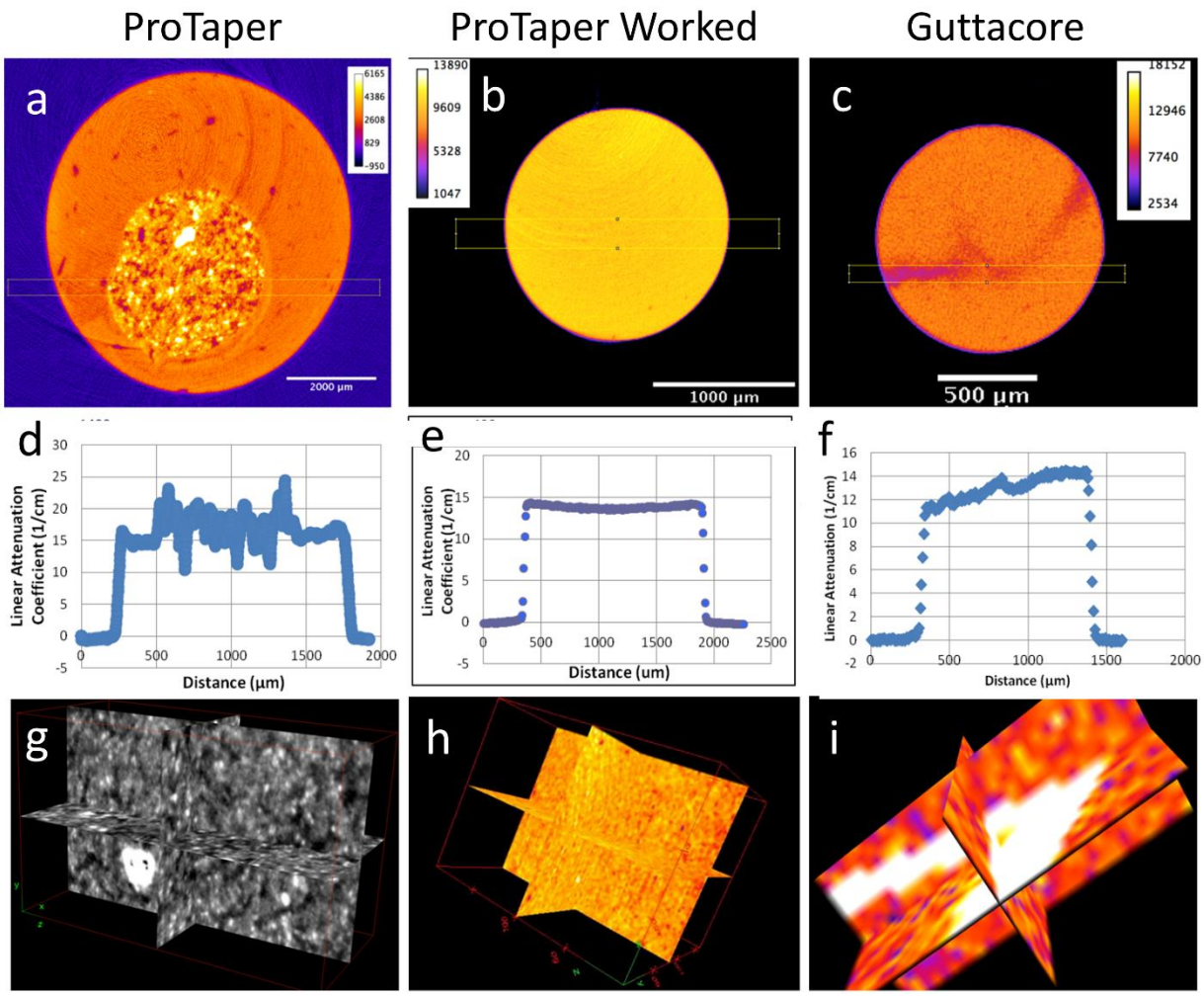

Figure 3.5 CMT of ProTaper™, ProTaper™ being worked for 2min, and Guttacore™: (a-c) two dimensional cross section, (d-f) plots of the attenuation coefficient vs distance corresponding to the box in upper panel, and (g-i) three dimensional plots of the x-ray attenuation coefficient across a volume segment.

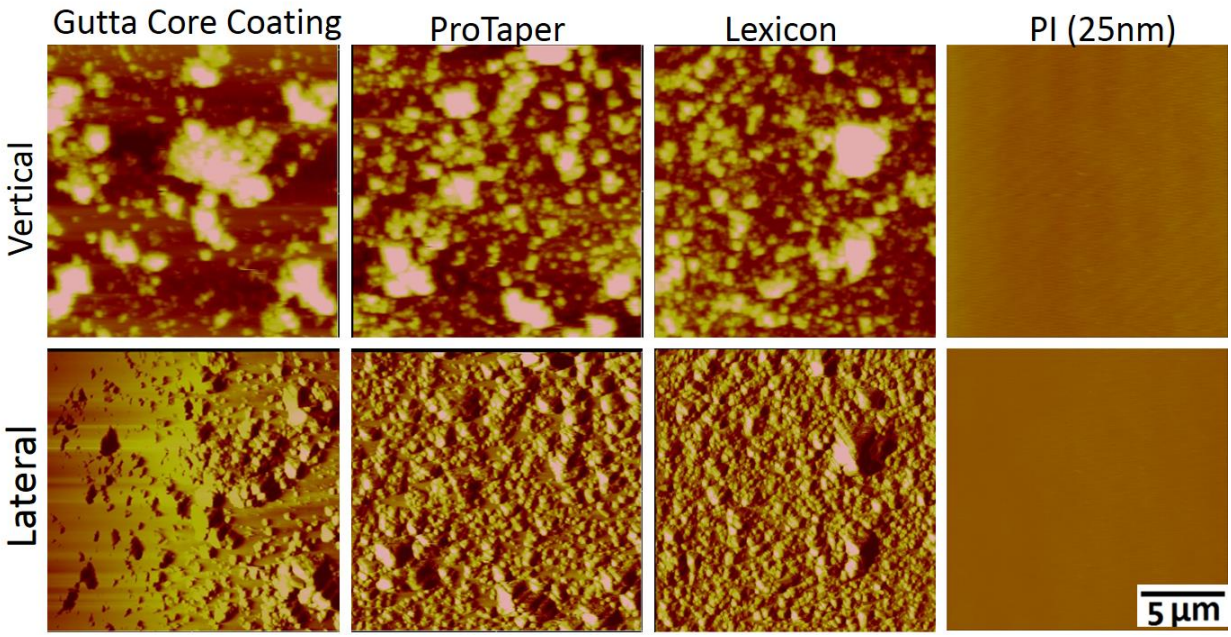

Figure 3.6 Scanning probe microscope (SPM) vertical and lateral scans of ProTaper™, Lexicon™, Guttacore™ coating, and PI coated Si substrates. The Z scales are 0-900nm (upper panels) and 0-4V (lower panels).

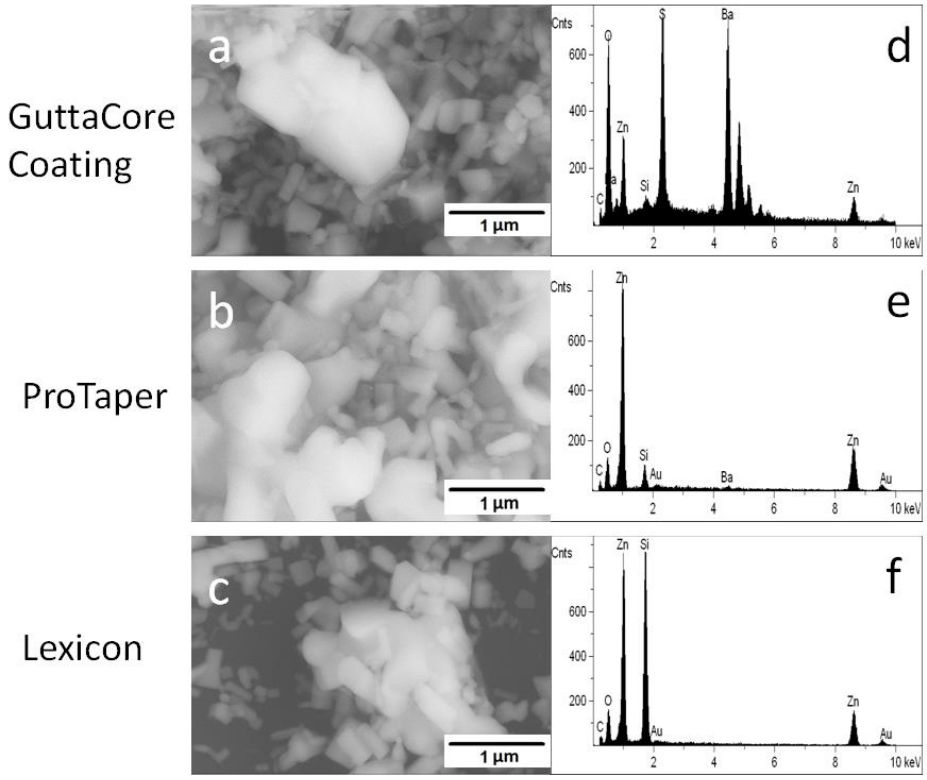

Figure 3.7 SEM and EDAX comparison of Gutta Percha coated on Si substrates: Guttacore™ Coating (a, d), ProTaper™ (b, e), Lexicon™ (c, f).

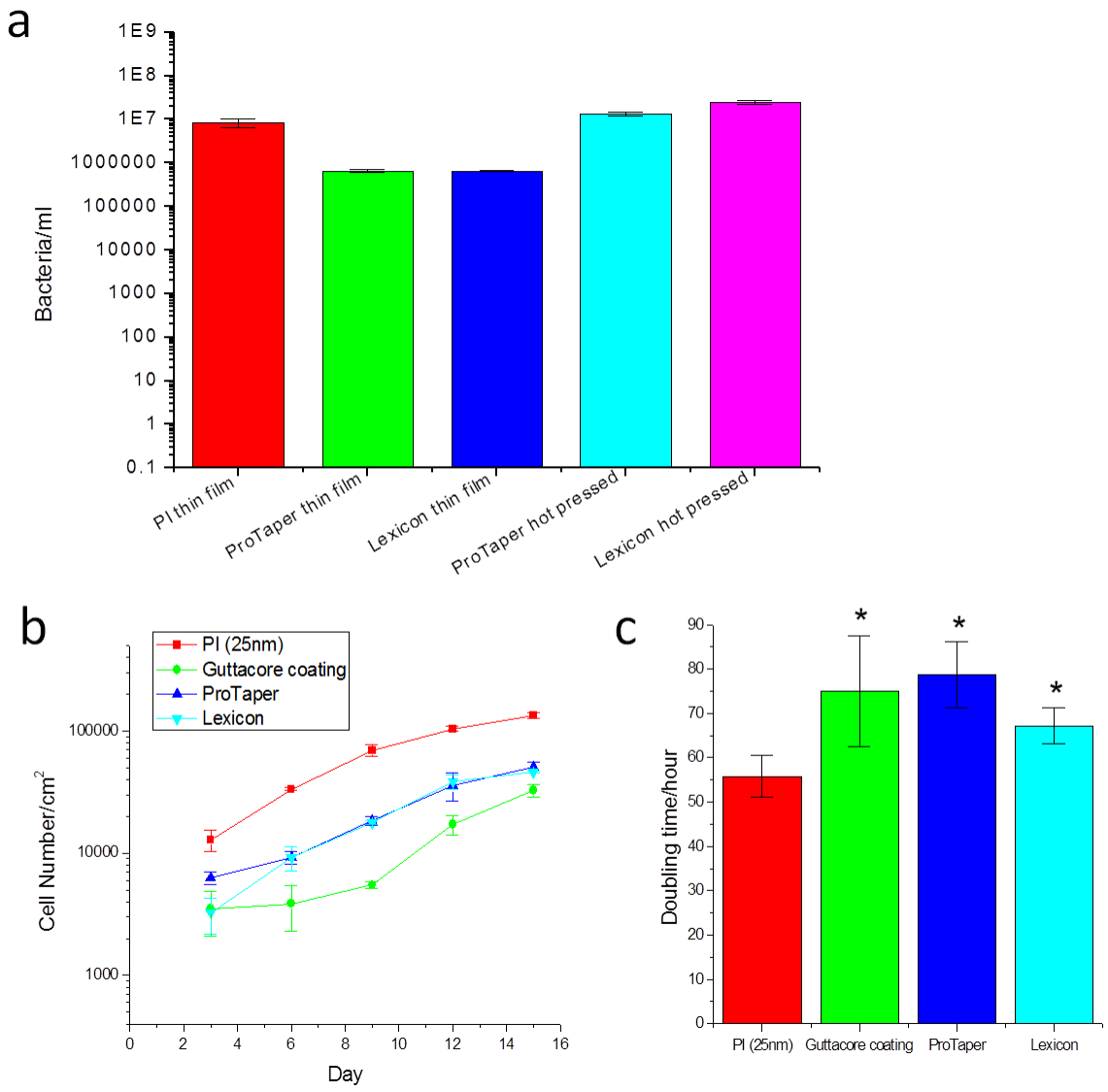

Figure 3.8 Biocompatibility of Gutta-percha. (a) Zone test for antimicrobial activity and efficacy on ProTaper™ and Lexicon™, which both spun cast on Si substrates and molded. 25nm PI coated Si substrate was used as control. Beginning Enterococcus faecalis concentration is 1E7, (b) DPSCs proliferation curve of ProTaper™, Lexicon™, and Guttacore™ coating coated Si substrates, with 25nm PI as control. The cell plating density is 10,000/cm^2, and (c) Cell doubling time calculated from (b). The Gutta-percha samples differ from control sample at a statistical level of P>0.05 (*).

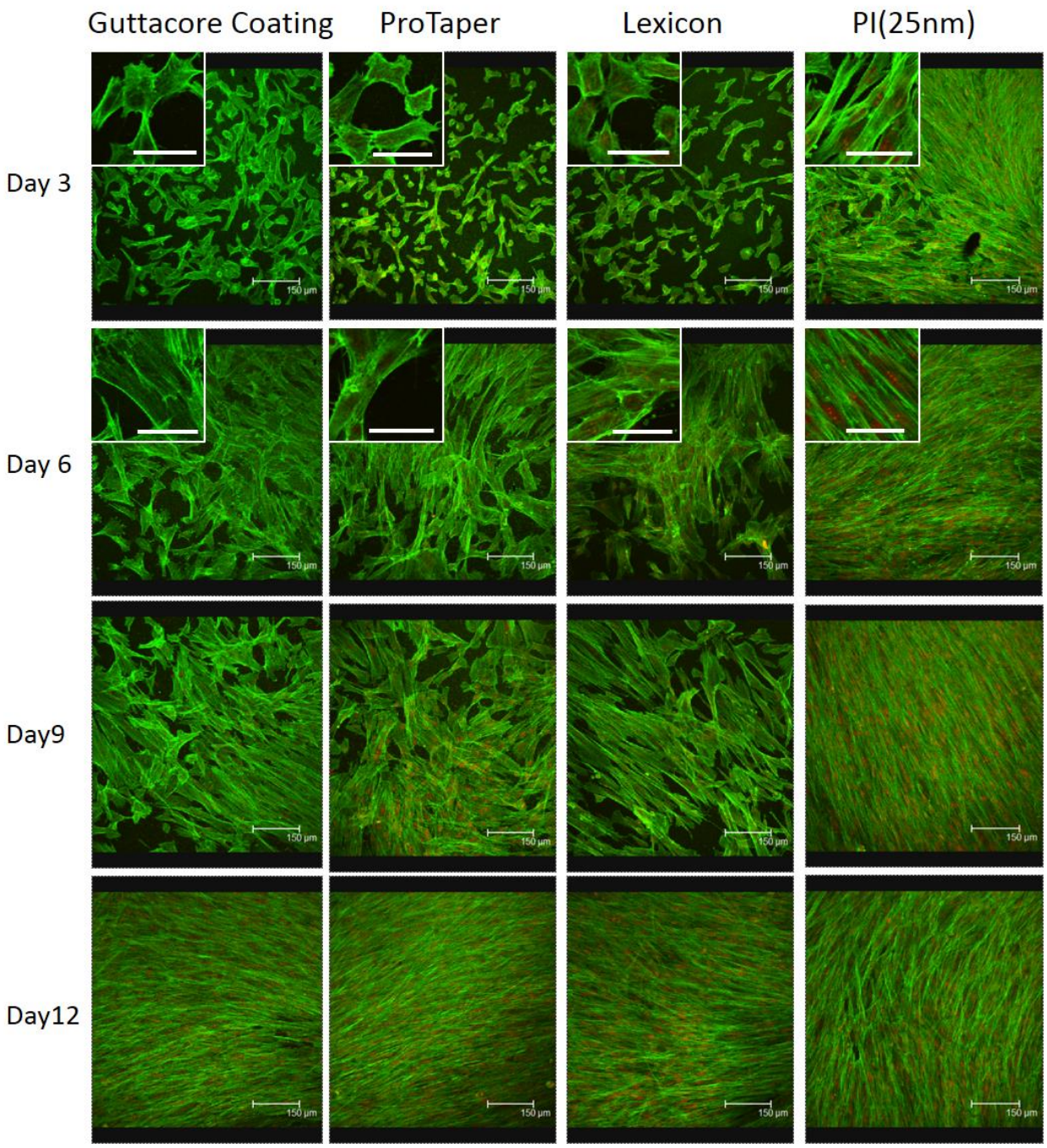

Figure 3.9 Confocal microscopy images of DPSCs morphology on ProTaper™, Lexicon™, Guttacore™ coating, and PI coated Si substrates at Day 3 and 6 without Dex. Insert scale bar is 50µm. DPSCs were stained with Alex Flour 488 for actin fiber (green) and Propium Iodide for nucleus (red).

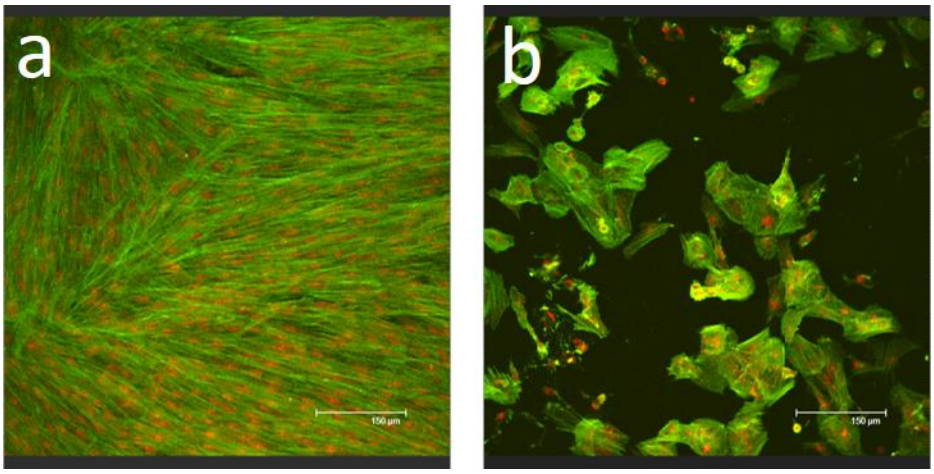

Figure 3.10 Confocal microscopy images of DPSCs morphology at (a) day 4 and (b) day 6 on tissue culture plastic, with a plating density of 10000 cells/cm^2. 0.05mg/ml ZnO was added at day 5.

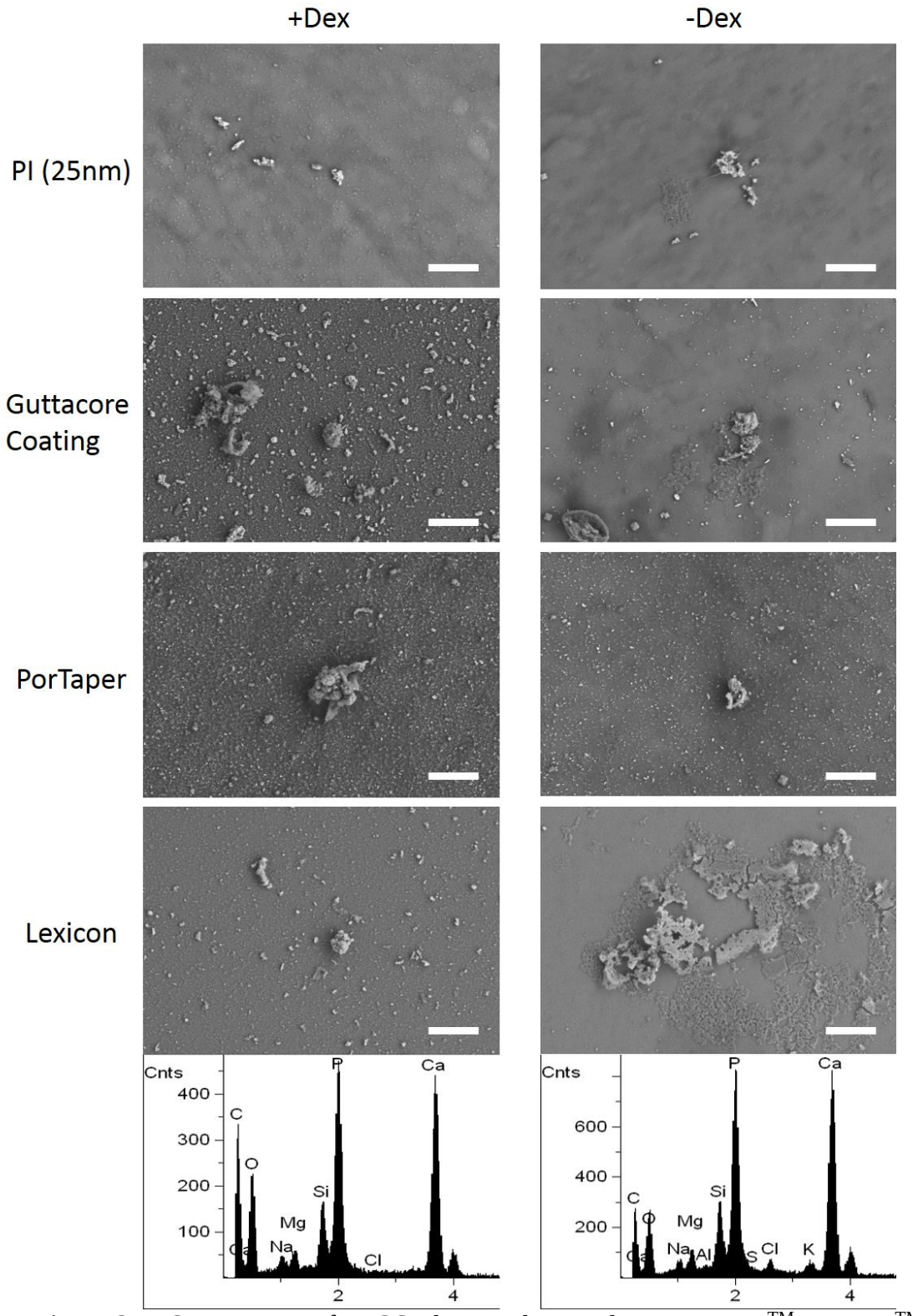

Figure 3.11 SEM images of DPSCs deposited minerals on ProTaper™, Lexicon™, Guttacore™ coating, and PI coated Si substrates at Day 21, with/without Dex. Each column of SEM images shares the same EDAX spectra. The scale bar is 50μm.

Chapter 4: The influence of substrates moduli on behavior of dental pulp stem cells cultured on Polyisoprene

4.1 Introduction

There is a critical need for a new approach to replace the current methods of dental and endodontic treatment. For immature health root elongation, the clean is preferred as it prevent tooth loss and avoid late requirement for implants. Currently, the conventional treatment options for permanent teeth that have sustained trauma which exposes the pulp predominately include root canal surgery and dental implants prepared from synthetic materials [91, 92]. However, root canal surgery does not restore the biological function of the dental pulp tissue after significant damage [74, 93, 94]. Even denture therapy is associated with symptoms, such as denture-induced stomatitis and traumatic ulcers [95]. Thus, it would be of great clinical benefit to develop a biologically based treatment to repair and regenerate traumatized teeth, to both avoid surgical procedures and preserve the natural tooth.

Recently, there has been some progress in tissue engineering and stem cell research provides insights for improving tooth regeneration. The main concept is to mimic the natural tooth development process either *in vitro* or *in vivo* using stem cells [96]. Stem cell proliferation and differentiation are dependent upon three main factors: the type of stem cell, the underlying scaffold, and the signaling molecules added, since they are sensitive to both chemical and mechanical changes in the environment [97]. Scaffold stiffness also can influence the mechanics

of cell grown on it [98-102]. Also, a lot of researchers showed that the migration, proliferation, and differentiation of stem cells were related to the physical properties of the extracellular matrix (ECM), such as elasticity, morphology, composition, and structure [103-106].

Dental pulp, the innermost soft living tissue of the tooth, is characterized by its abundance of multipotent DPSC. As undifferentiated mesenchymal stem cells, DPSC isolated from dental pulp has been used in many studies for biomedical applications. They are capable of self-renewal, proliferation, and have the potential to differentiate into various cell types including osteoblasts, odontoblasts, myocytes, adipocytes, and neuronal cells [107-110]. Because of their easy accessibility, high efficiency of extraction procedure, fast multiplication rate, and ability to express markers of various cells when grown in specific inducing media, DPSCs may be a candidate for studying stem cell regenerative therapies and tooth decay repair [111-113].

It has been reported that some materials, such as poly (lactic-co-glycolic), poly (ι -lactic acid), poly(ε -caprolactone), gelatin hydrogels, and hydroxyapatite/tricalcium phosphate ceramic, could be used as scaffold in dental pulp regeneration for *in vivo* and *in vitro* DPSC differentiation with external chemical inducers [8, 72-75]. Dexamethasone (Dex), which is a glucocorticoid steroid, has been shown the ability of chemically inducing DPSCs to express odontogenic markers and mineralization *in vitro* [114, 115]. However, the external chemical inducers such as steroids can cause adverse side effects such as hyperglycemia and a weakened immune system when applied *in vivo* [76]. Furthermore, it has been reported that chemical differentiation of DPSCs into specific tissue requires special media i.e. high glucose or high oxygen (20%) to differentiate and grow [116]. These conditions are nearly impossible to reproduce in vivo. The possible solution for that could be finding a trigger which induces

differentiation locally without globally changing the chemical or metabolic environment. Thus, material scaffolds that possess the optimal surface chemistry, topography, and properties to stimulate DPSC proliferation and differentiation, are essential to tooth regeneration.

Ideal scaffolds provide a foundation and initial support for cells to adhere, signal, proliferate, and differentiate. Because scaffold surface topography, chemistry, and mechanical properties can influence cell behavior, it is essential to manipulate such factors and understand their effects to create a bioactive scaffold. Our previous research indicated that the enzymatically crosslinked gelatin hydrogels were extremely effective substrates for DPSCs differentiation towards odontoblasts in the absence of dexamethasone [7]. Thus, it's possible to induce DPSCs differentiation *in vitro* in the absence of chemical inducer. However, little progress has been made in producing a scaffold with materials approved for use in the mouth, which also induces the exposed DPSCs of the traumatized tooth to proliferate and differentiate finally regenerate a new pulp-dentin complex.

Polyisoprene (PI) is a hydrophobic biocompatible synthetic rubber material (Tg = -67 ℃) used in dentistry as the polymer matrix for Gutta-percha, which is used to obturate root canals. Chang *et al.* have recently shown that polybutadiene (similar to PI) thin film on Si wafer substrate of a moduli higher than 2.3MPa induced upregulation of osteocalcin gene expression and deposition of crystalline hydroxyapatite deposits without other soluble induction agents, such as dexamethasone or BMP-2 [97]. In this study, we spun cast monodispersed PI (Mw/Mn =1.36) with high molecular weight chains (Mw =87.5K), and Rg≈71Å on Si wafer substrates. In order to determine whether DPSCs can sense the mechanics of the underlying PI substrate, the moduli of PI substrates were controlled by varying thickness of film while DPSC grown for 28 days. The stiffness of DPSCs on PI substrate with/without Dex at early time points were measured by shear

modulation force microscopy and optical tweezers. The results were compared to cell morphology and biomineralization at late time points. Furthermore, TiO_2 nanoparticles were added to the PI matrix to evaluate the proliferation of DPSCs on the polymer nanocomposite scaffold. The polymer matrix-nanoparticle fillers system were similar to clinically used root canal obturators. Thus, we provided the potential of PI as a scaffold material for tooth regeneration therapy without chemical inducers.

4.2 Experimental Section

4.2.1 Preparation of thin film surfaces

Polyisoprene (Mw=87,500, polydispersity index=1.36, Scientific Polymer Products) was dissolved in toluene (Sigma-Aldrich) at a series of concentration. Besides the PI solution, we also added anatase and rutile titanium dioxide (TiO_2) nanoparticles respectively into it and made suspensions with a final concentration of 0.5mg/ml. All the solutions/suspensions were spun cast onto hydrophobic Si wafers, as described in chapter 2, at 2500rpm for 30s. The thickness of the layers was measured by ellipsometry (Rudolph Technologies). Polymer films were then annealed at 130 ℃ in a vacuum of 10^{-8} Torr overnight to remove the residual solvent, sterilize, and relax strains induced by the spinning process.

4.2.2 Shear modulation force microscopy (SMFM)

The moduli of PI films and DPSCs cultured on PI films were measured by Scanning Probe Microscope (SPM, Dimension 3000; Digital Instruments, Co., Ltd. Santa Barbara, CA). SPM was operated in shear modulation force microscopy (SMFM) mode using a silicon nitride tip on a cantilever with a bending spring constant of 0.06 N/m [117]. During the measurement, a normal indenting force of 25nN was exerted by the cantilever to induce a small oscillatory

motion. The SPM tip, when applied to indent the surface, was laterally modulated and the mechanical response was fed into a lock-in amplifier and recorded [118]. When the drive signal amplitude was varied from 7.5mV up to 125mV, which corresponds to an x-piezo displacement of 1.5–25nm, the cantilever response was recorded to estimate the stiffness of the sample surface [7]. The drive frequency of 1400Hz was chosen for the measurements since it lies in the flattest region of the cantilever's response curve. A total of nine experimental points (three times per spot and three points per sample) were obtained for each sample.

4.2.3 Cell isolation and cell plating

Human dental pulp stem cells (DPSC) strain AX3 were isolated and cultured as described in previous chapter 3. Then the DPSCs were seeded onto PI films, PI with TiO_2 films, and tissue culture polystyrene plastics (TCP) at a density of 5000 cells/cm^2. The number of DPSCs grown in "base media" was counted on day 3, 6, and 8 using a hemacytometer (Hausser Scientific). For the differentiation experiments, half of the samples were cultured with the "base medium" and the other half with the "induction medium" till 28 days. Culture medium was refreshed every alternate day.

4.2.4 Confocal laser scanning microscopy

Actin cytoskeleton organization and the morphology of the cells on days 3, 6, 8, and 28 were visualized as described in previous chapter 3.

4.2.5 Optical tweezer microrheology

Oscillating optical tweezer technique developed by Wei M *et al* [119] was used to measure the microrheological properties of DPSCs on PI substrate. Protein-A coated 1.5μm silica beads (G.

KISKER GbR, Germany) were treated with the anti-integrin αV antibody (Sigma, CD51) by incubation at 50 μg per 1 mg of beads in phosphate buffered saline (PBS) [120]. The bead solution was added to the cell-seeded substrates for 20 minutes incubation. This process allowed the bead to adhere to the plasma membrane by the formation of integrin-antibody linkages for extracellular stiffness measurement. Unmodified beads were endocytosed into the cell and indirectly measured the modulus of cytoplasm, referred to as intracellular stiffness. Then a polarized laser beam was used to sinusoidally oscillate the bead at different frequencies. A second laser beam was used to measure the bead's displacement and phase shift as a function of oscillation frequency to determine the viscoelastic moduli of the media. [121]. The trapped bead was forced to oscillate along the x direction by the oscillatory tweezers driven by the PZT-controlled mirror.

4.2.6 Scanning electron microscopy and energy dispersive analysis X-ray (SEM/EDAX)

The elemental compositions of deposits on PI films were determined as described in previous chapter 3.

4.3 Results and Discussion

4.3.1 Mechanics of PI substrates and DPSCs proliferation

PI surfaces were prepared by spin casting thin films onto polished single crystal silicon wafers, with a series of thickness from 15 to 210nm, to determine the correlation of film hardness with film thickness. SMFM was used to measure the moduli of PI substrates. As shown in Figure 4.1, the moduli of PI films are plotted as a function of film thickness. We can see that the moduli of the films followed a continuous decreasing exponential function, with increasing of film thickness. Previous research by Zheng *et al* showed that the decrease in viscosity with film thickness had a similar functional form, by a 10Rg decay length [122]. Since Rg of PI we

used was calculate to be apporimary71Å, we noticed that when the thickness of film was less than 4Rg, the substrate influence resulted in large increase of the modulus relative to the bulk value obtained for the thicker film. On the other hand, when this thickness is larger than 4Rg, the influence of the substrate is minimized.

In order to determine whether the substrate mechanics influence cell proliferation, DPSCs were cultured on PI films with different thickness. The growth curve and doubling time of DPSCs grown on PI substrates are shown in Figure 4.2(A, B), compared with DPSCs grown on TCP. PI films of three thicknesses were used and the moduli of them were calculated from the curve in Figure 4.1, 25nm with a modulus of 2.76MPa, 120nm with a modulus of 1.16MPa, and 200nm with a modulus of 0.70MPa. In Figure 4.2A, the difference of cell numbers at day 3 shows a difference in plating efficient on each PI substrates. It suggests that harder PI substrate may have better plating efficient than softer one. In Figure 4.2B, the doubling time of cells on the 25nm PI substrate (51.5 ±1.0 h) is close to the value on TCP (44.3 ±3.2 h), indicating that the harder PI surface supported cell adhesion and proliferation similar to TCP, without the need for additional surface modification. On the thicker 120nm PI substrate, the doubling time increases a lot (62.6 ±3.6 h), and is statistically different from control ($p<0.05$). Furthermore, the DPSCs didn't proliferate at all on the 200nm PI substrate. Since the composition of the substrate is the same, these results indicate that the DPSCs are sensitive to the changes in substrate mechanics and are adversely affected by the decrease in modulus.

At day 3, 6, and 8 after plating, the DPSCs on these substrates were stained with Alexa Fluor 488 Phalloidin to visualize actin fibers and propidium iodide to visualize nuclei, with confocal microscopy, as shown in Figure 4.3. It was clear that the cells grown on the harder 25nm PI substrate are well extended with organized actin fibers, similar to those on TCP, while the cells

grown on softer 120nm PI show less organized actin cytoskeleton and morphology. And there are only few poorly organized dying cells on 200nm PI, which is consistent with the cell counting number. Similar to our results, it was reported that the fibroblasts and endothelial cells plated on harder hydrogel substrates had more extended actin filaments and exerted larger traction forces compared to cells plated on softer ones [102, 123]. Our previous research also indicates that the increased doubling time on the softer polybutadiene (PB) may be due to the inability of the cells to exert adequate traction [118]. Thus, that could also be the reason for the increased doubling time on the softer PI substrate, since it's know that cell division is impart regulated by the ability of cells to exert large traction forces [123].

4.3.2 Mechanics of DPSCs on PI substrates

From the cell proliferation experiment, we know that DPSCs can sense substrates mechanics and will proliferate differently on substrates with different moduli. In order to further determine whether substrate mechanics also influences cell mechanics, the moduli of DPSCs grown on PI films were measured using the SMFM liquid cell setup method. In this experiment, we used 25nm PI films considered to be "thin" PI and 120nm PI films as "thick" PI. It has been previously reported that independent of chemical inducers, the moduli of DPSCs grown on PB thin films reaches a plateau at day 7 and the increases after day 7 are not significant [97]. Thus, only time points before day 7 were chosen for cell modulus measurement. As shown in Figure 4.4, without the chemical inducer, Dex, the moduli of the cells decreases with increasing of film thickness. Also, compared to day 5, the difference becomes lager at day 7. We not only studied the mechanic influence, but also compared the influence of chemical environment. Thus, the moduli of the DPSCs grown with chemical inducer Dex are also shown in Figure 4.4. Compared to the cells without Dex, the moduli of the cells grown with Dex are higher after 5 days of

incubation. In Figure 4.4, we can see clearly that the moduli of cells grown on the thick PI samples increases by a factor of three after 5 days of incubation with Dex. In this case, Dex rather than the modulus of the substrate appears to determine the moduli of the cells. In the case of cells grown on thin PI without Dex, the moduli of the cells is more than twice of thick PI at day 5 and three times larger at day 7. It is even close to thick PI with Dex sample at day 7. On the other hand, adding Dex to the media for thin PI samples results in an additional increase in the cell moduli by nearly 75% at day 7, indicating a synergistic or addition effect when mechanical and chemical induction are combined. These results are consistent with the previous report that the moduli of PB films and DPSCs grown on top followed a continuous decreasing exponential function with increasing of film thickness [97].

We next used optical tweezers to monitor membrane cytosol stiffness as a function of substrate and Dex, and compare to the moduli measured by SMFM. For the extracellular stiffness of cells, bead with antibodies was attached to integrin receptors on cell membrane and directly measured cell membrane rigidity. For the intracellular stiffness of cells, unmodified bead was endocytosed into the cell and indirectly measured the modulus of cytoplasm. To be able to see cells through microcopy, glass substrates were used instead of Si wafer. As was evaluated by SMFM, we used 25 nm PI films (thin PI), and 120nm PI films (thick PI), and the glass substrate as control sample. Although these PI thin films were spun cast on glass substrates instead of Si wafers, the moduli were similar to that of Si wafer substrates as measured by SMFM (Figure 4.5A). We also used a Rho-associated, coiled-coil containing protein kinase (ROCK) inhibitor, Y-27632 dihydrochloride, in this study, to block focal adhesion signaling, which influences the cells ability to sense the substrate. For samples without addition of the Y-27632, as shown in Figure 4.5(B, C), the intracellular and extracellular stiffness measurements have the same

tendency between them and a similar tendency to the SMFM results (Figure 4.4). It further confirms our hypothesis that the mechanics of substrates could influence the cells grown on top. Furthermore, the addition of Y-27632 decreases intracellular stiffness by more than 10X by day 7, while Y-27632 differential effect is smaller for extracellular stiffness. And it is the same tendency for all the growth conditions, independent of the chemical inducer Dex. It's well known that the integrins serve to link the extracellular matrix (ECM) and the intracellular actin filamentous system across the plasma membrane, and with focal adhesion kinase (FAK) transmitting signal from integrin receptors. Thus, it indicates that the ROCK inhibitor, Y-27632, could cutoff the signals from integrin receptor and thus block integrin sensing of the surface. This result is consistent with previous reports that ROCK inhibitor Y-27632 blocks the Rho cascade, thus inhibiting actomyosin contraction and disrupting actin stress fibers [124]. The cell membrane can receive mechanical cues from environment to cause a polarized intracellular tension, which may cause the subsequently FAK polarity and can be attenuated by RhoA activity and actin stress fibers [125]. The actin stress fibers could be contributed to the increased stiffness of cells.

4.3.3 Characterization of the biomineralization deposits

To further study the correlation of the increase in DPSCs moduli with biomineralization after a long period growth, the DPSCs were cultured on the thin and thick PI substrates for 28 days with and without Dex. Confocal microscopy images of the cells after 28 days of incubation, stained with Alexa Fluor 488 Phalloidin for actin fiber and propidium iodide for nucleus, is shown in Figure 4.6. Where we see that the cells grown with Dex have some rounded appearance on both thin and thick PI substrates, and the actin fibers do not as well organized as the ones without Dex. According to previous report, that is the typical morphology of differentiated DPSCs [97].

Additionally, for the cells cultured without Dex, they have more extended and better organized actin fibers on the thick PI substrate, comparing to the thin PI. It suggests that the substrate mechanics had influence on differentiation of the cells. Thus, the DPSCs on the softer thick PI substrate are not able to differentiate without chemical inducer Dex.

After the cells were taken away, SEM and EDAX were used to identify the mineral deposits on PI substrates. SEM images in Figure 4.7 shows a large number of deposits on thin PI substrates either with or without Dex. On the other hand, no deposits were observed on thick PI substrates without Dex. The Ca, P, O peaks on EDAX spectrums confirm that the mineral deposits are calcium phosphates. These results indicate that mechanics of PI substrates alone can induce DPSCs to biomineralize, in absence of the chemical inducer. Then we could compare these results to the cell moduli at earlier time points shown in Figure 4.4 and 4.5 (A, B, C). We notice that only the samples that had increased cell moduli at earlier time points show biomineralization deposits at day 28. It indicates that the increase in cell moduli at earlier time point is related to the biomineralization after long period growth. Thus, the measurement of cell moduli at day 7 may be used as a sign for predicting the later cell behavior on substrates. The results are also consistent with previous research that for the DPSCs grown on PB thin films without Dex, biomineralized deposition could only be observed on substrates with a critical modulus larger than 2.3 MPa [118].

4.3.4 Influence of PI with TiO_2 thin films on DPSCs proliferation

For root canal therapy, the dentist removes debris and infected tissue in root canal, and fills the chamber with an inert material, such as Gutta-percha. In the inert materials, nanoparticle fillers are usually added to polymer matrix to provide mechanical properties, radiopacity, anti-bacterial

properties, *etc.* Since we know that the softer PI substrate (thickness greater than 120nm) is not good for DPSCs proliferation, we decided to evaluate the behavior of cells when hard nanoparticles are introduced to the PI films. Thus we spun cast two kinds of nanocomposite thin films: 120nm PI with anatase TiO_2 nanoparticles (thick PI+A) and 120nm PI with rutile TiO_2 nanoparticles (thick PI+R). anatase and rutile are two crystal forms of TiO_2 with almost the same properties, such as hardness, density, and luster. The moduli of pure PI and PI with TiO_2 nanoparticles substrates were measured with SMFM and shown in Figure 4.8. It is clear that the moduli pf PI spun cast with TiO_2 are closer to thin PI (25nm) rather than the thick one (120nm), even though the PI matrix is 120nm thick. Therefore, the cell behavior on thick PI+A and thick PI+R may be more like the thin PI substrate. The growth curve and doubling time of DPSCs on PI with TiO_2 confirm that, as shown in Figure 4.9. The growth curve and doubling time of PI+0.5A (53.0 ±1.6 h) are almost the same as that of thin PI (51.5 ±1.0 h). The growth curve and doubling time of PI+0.5R (44.7 ±2.6 h) are also closer to that of thin PI rather than the thick one, even with a shorter doubling time than thin PI. The difference of cell numbers at day 3 could be due to different plating efficient on each substrate. It suggests that harder substrate may have better plating efficient than softer one. Furthermore, the confocal microscopy images in Figure 4.10 confirm that DPSCs proliferated better on thin PI and PI with TiO_2 substrates than thick PI at day 8. The results indicate that the addition of TiO_2 nanoparticles made the PI film harder, thus improved DPSCs proliferation on the substrate. It is consistent with our previous research that DPSCs proliferated well and biomineralized on Gutta-percha substrates in chapter 3.

4.4 Conclusion

Previous research indicated that the gene expression such as osteocalcin (OCN) of DPSCs was regulated by two separate signaling pathways, one was by the mechanical cues, probably through

focal adhesion points, and the other induced by Dex receptor mediated signaling events [118]. Thus, this chapter compared the effects of mechanical inducer and chemical inducer on DPSCs proliferation and biomineralization. The DPSCs proliferated better on harder PI based substrates, with or without nanoparticles, and hydroxyapatite biomineralized deposits were observed at day28 whether chemical inducer Dex was added or not on harder PI substrate (Modulus larger than 2.3 MPa), which could be related to the increase of cell modulus at earlier time points. The results indicate that the DPSCs can sense mechanics of substrates with harder surfaces better for cell proliferation and differentiation without chemical inducer. Hence PI may be used as a polymer matrix to re-engineer for pulp regeneration rather than obduration.

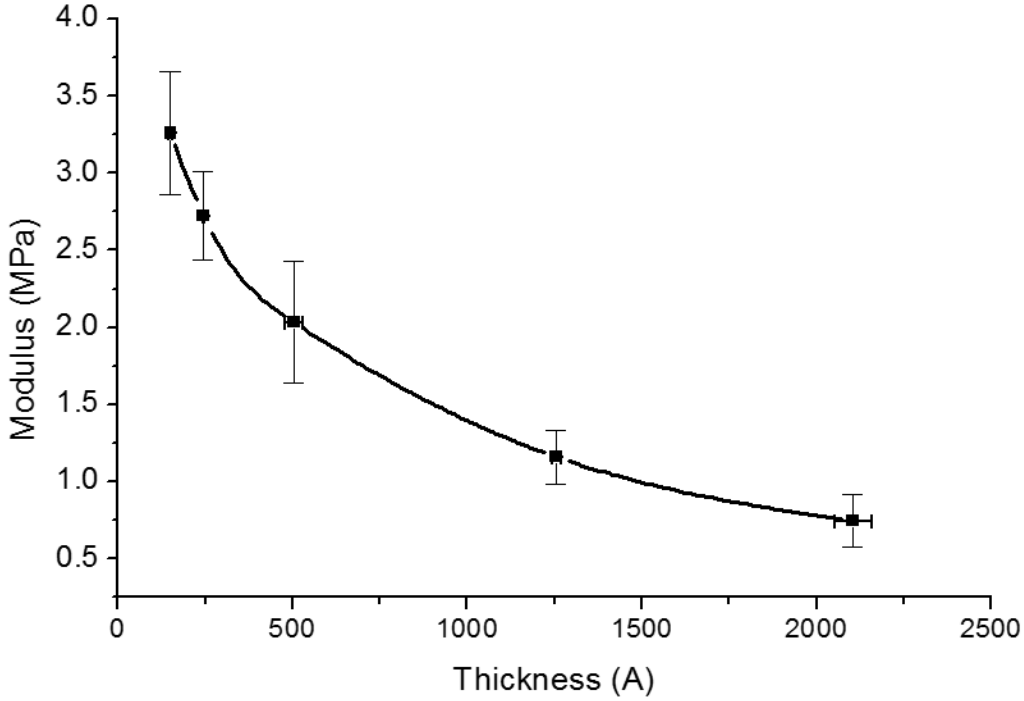

Figure 4.1 The correlation of the SMFM moduli of PI coated Si substrates with the film thickness.

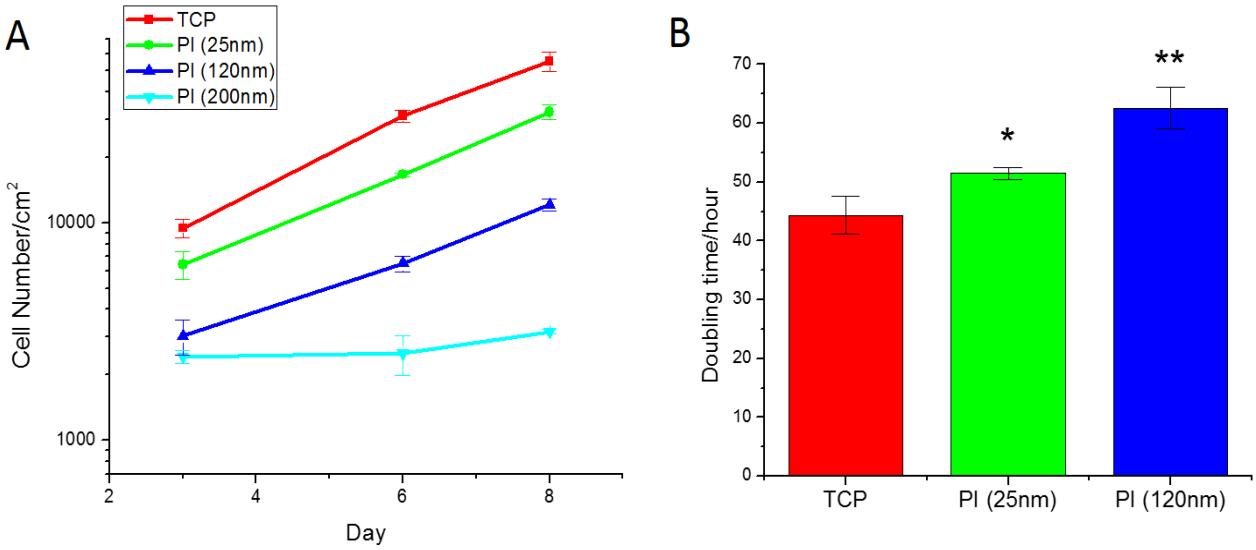

Figure 4.2 Cell proliferation curve (A) and doubling time (B) of DPSCs grown on different thickness PI coated Si substrates, with TCP as control. The PI samples differ from control sample at a statistical level of $P>0.05$ (*) and $P<0.05$ (**).

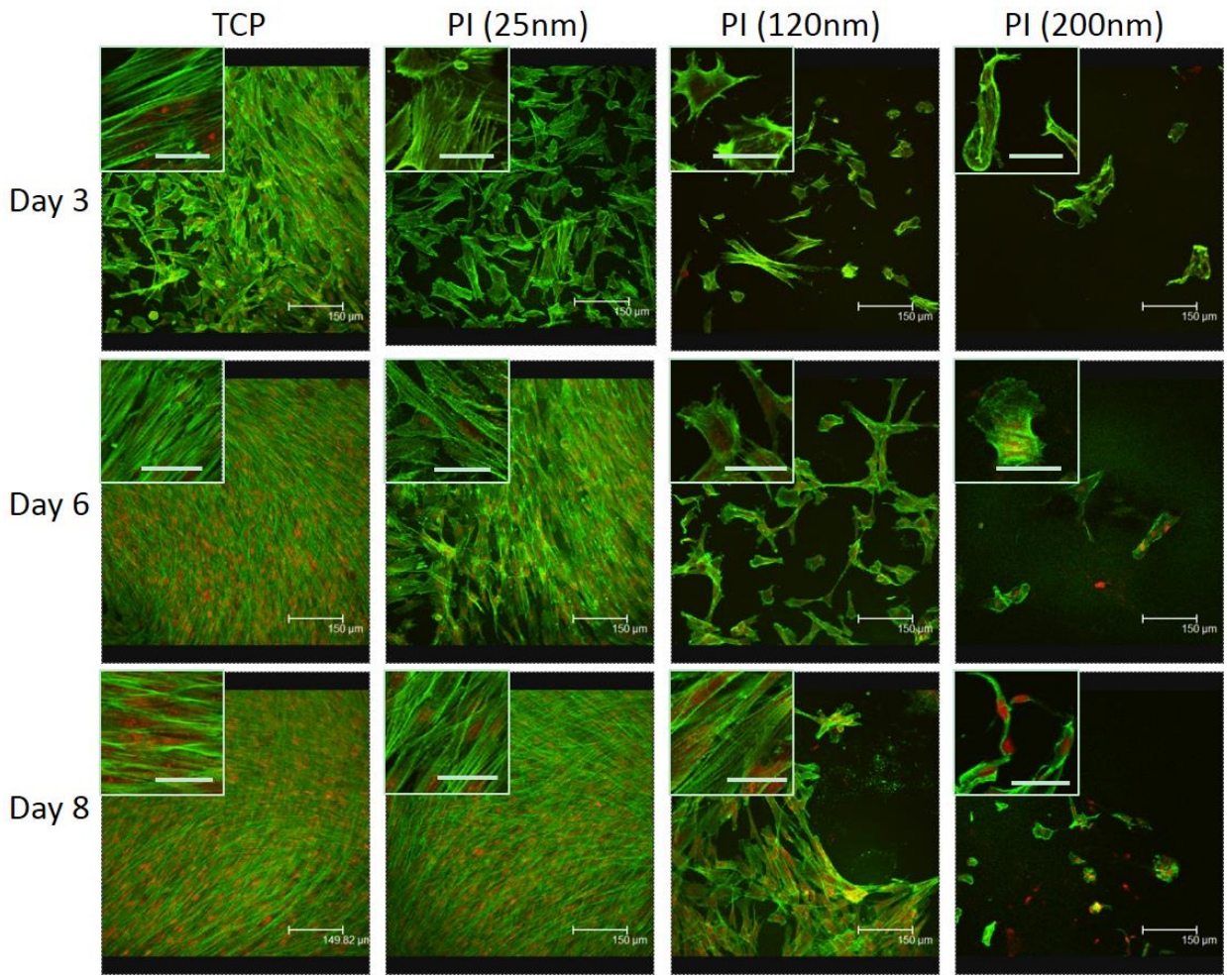

Figure 4.3 Confocal microscopy images of DPSCs morphology and organization on different thickness PI coated Si substrates at Day 3, 6, and 8 (Insert scale bar is 50μm). DPSCs were stained with Alex Flour 488 for actin fiber (green) and Propium Iodide for nucleus (red).

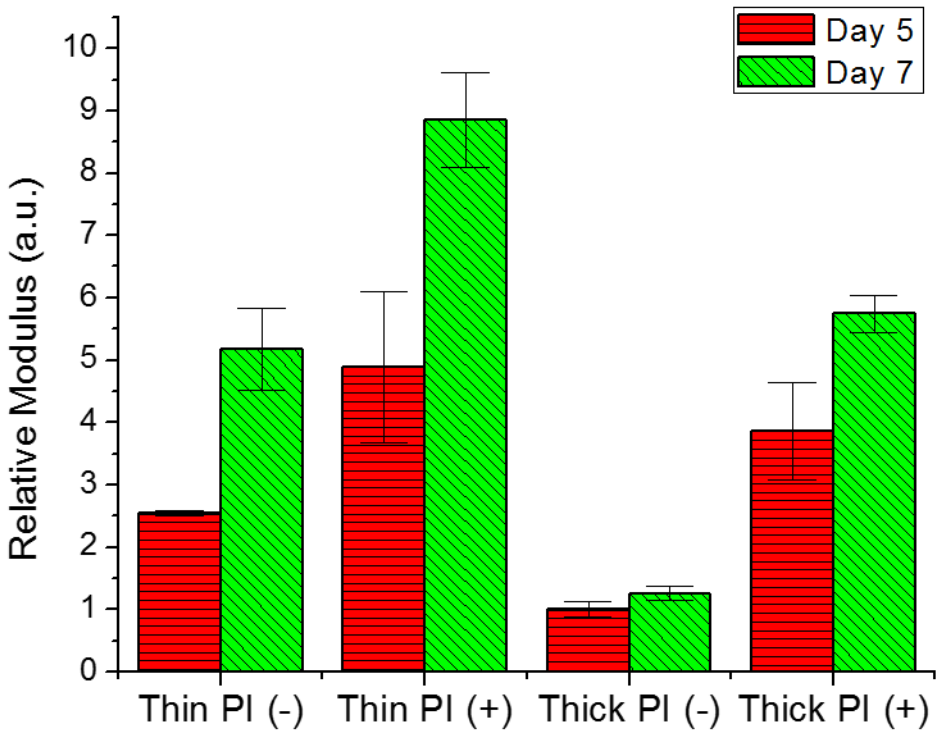

Figure 4.4 The SMFM moduli of the DPSCs grown with and without Dex on thin (25nm) and thick (120nm) PI coated Si substrates at day 5 and 7.

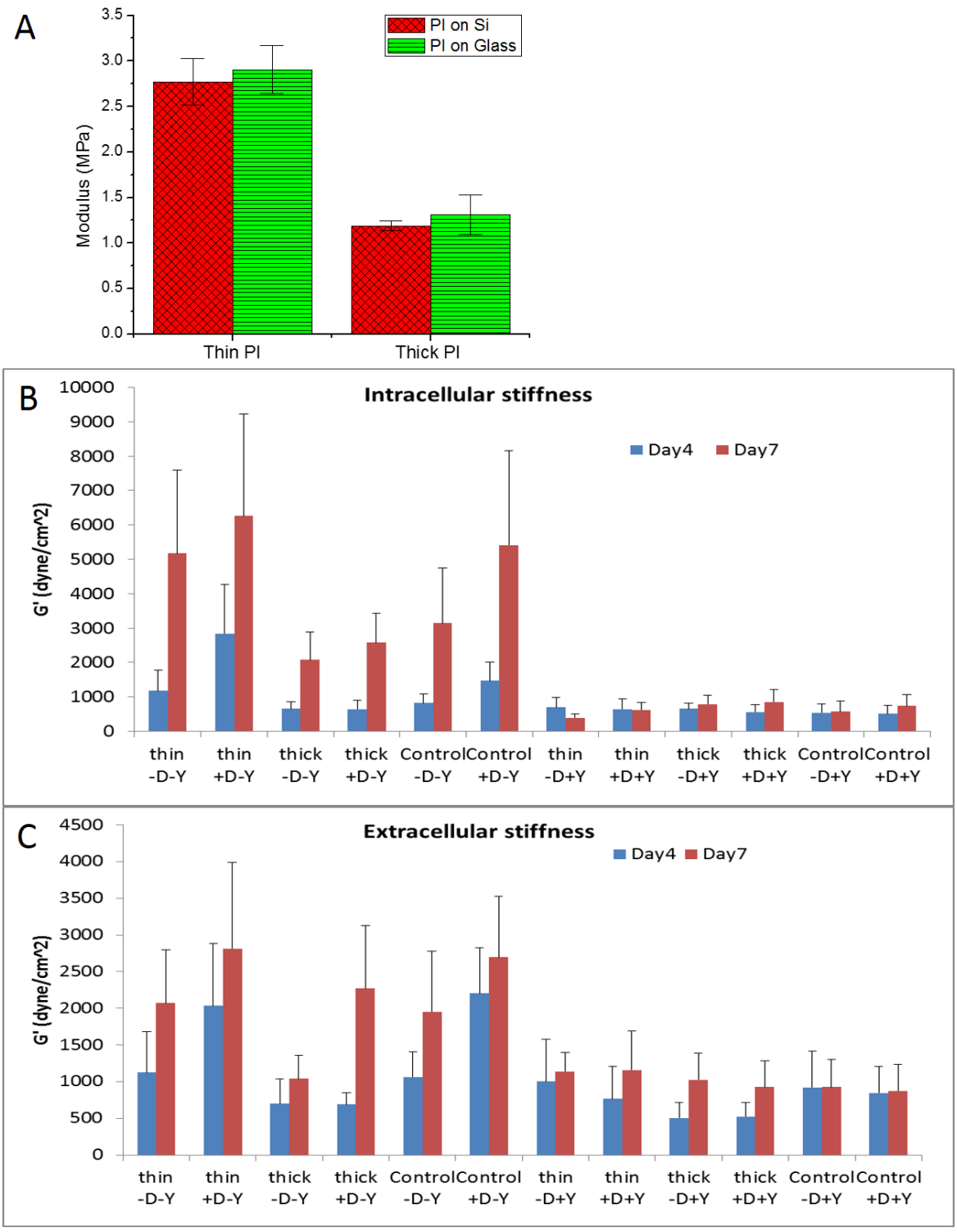

Figure 4.5 (A) The SMFM moduli of PI coated Si substrates and PI coated glass substrates. (B, C)The intracellular and extracellular stiffness of the DPSCs grown with/without Dex and with/without Y factor on thin (25nm) and thick (120nm) PI coated glass substrates at day 4 and 7, measured with optical tweezers.

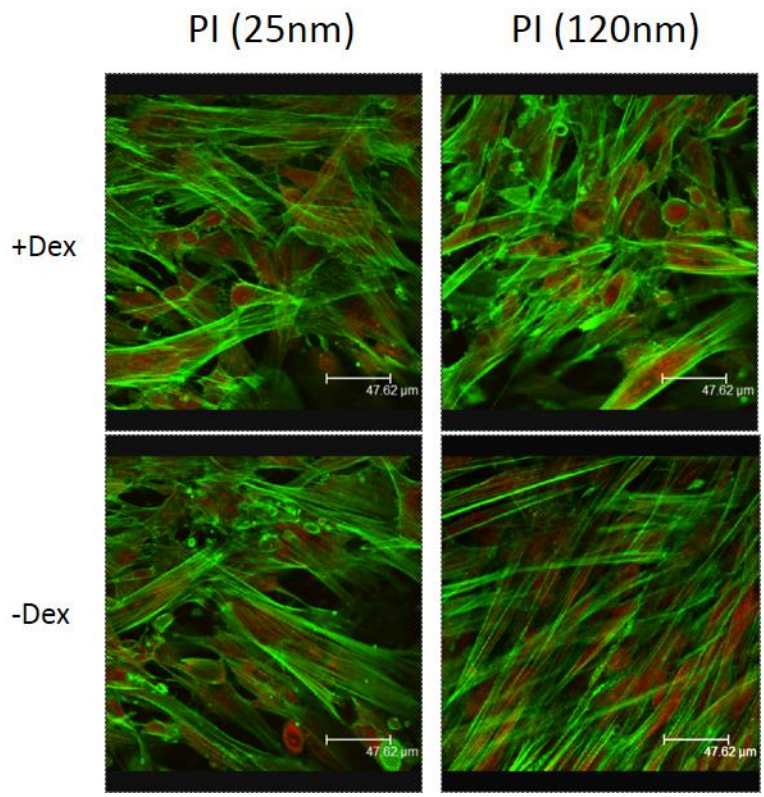

Figure 4.6 Confocal microscopy images of DPSCs morphology and organization on thin (25nm) and thick (120nm) PI coated Si substrates at Day 28, with and without Dex. DPSCs were stained with Alex Flour 488 for actin fiber (green) and Propium Iodide for nucleus (red).

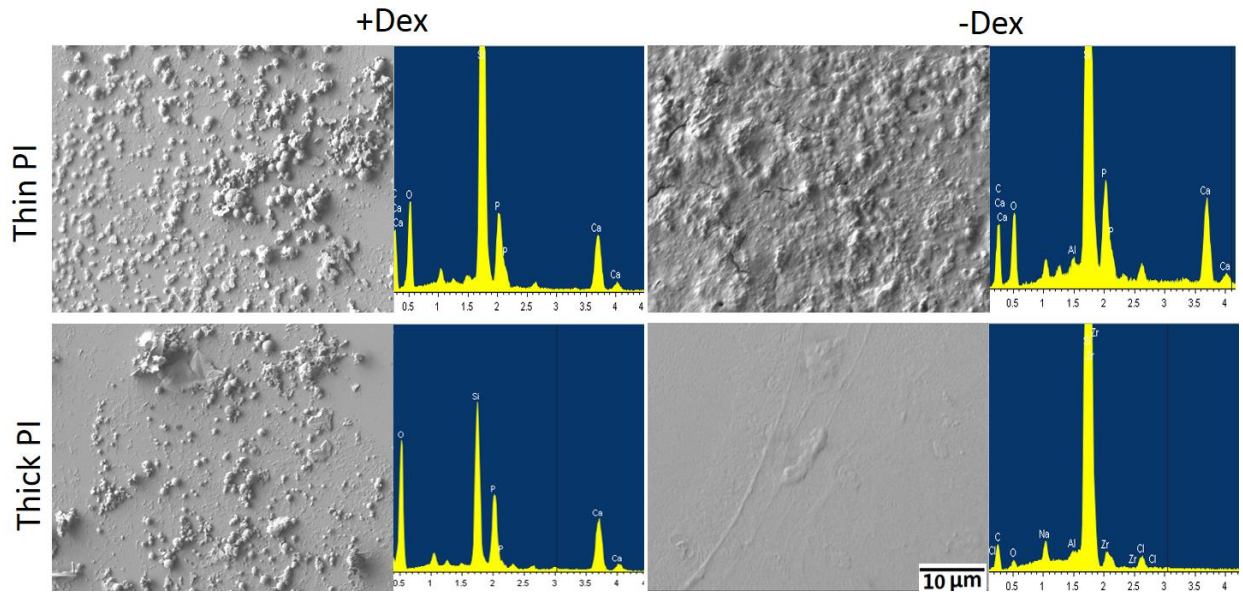

Figure 4.7 SEM images and EDAX spectra of DPSCs deposited minerals on thin (25nm) and thick (120nm) PI coated Si substrates at Day 28, with/without Dex.

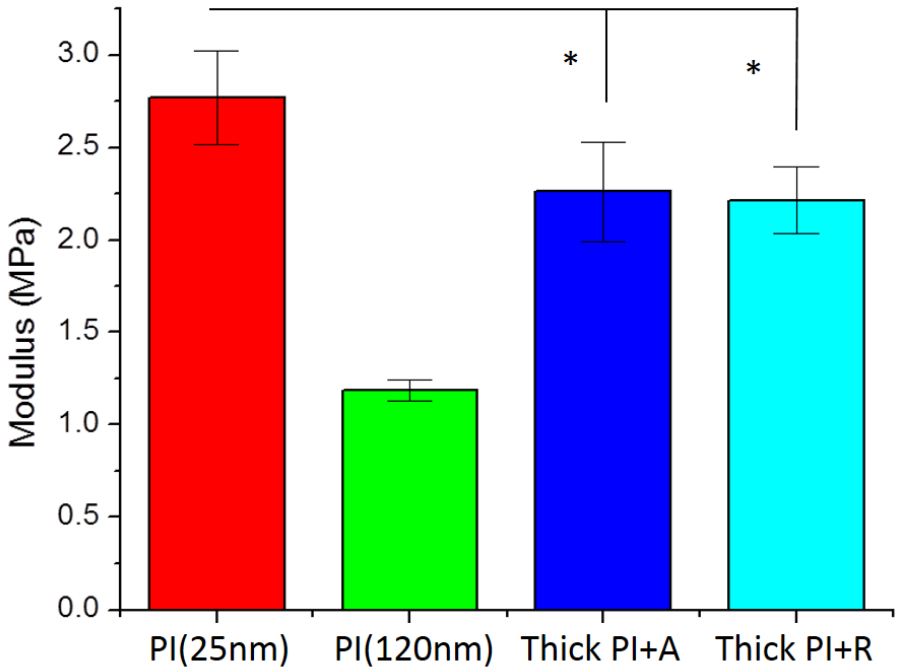

Figure 4.8 The SMFM moduli of thin PI (25nm), thick PI (120nm), thick PI with Anatase TiO_2, and thick PI with Rutile TiO_2 coated Si substrates. The results differ at a statistical level of $P>0.05$ (*) and $P<0.05$ (**).

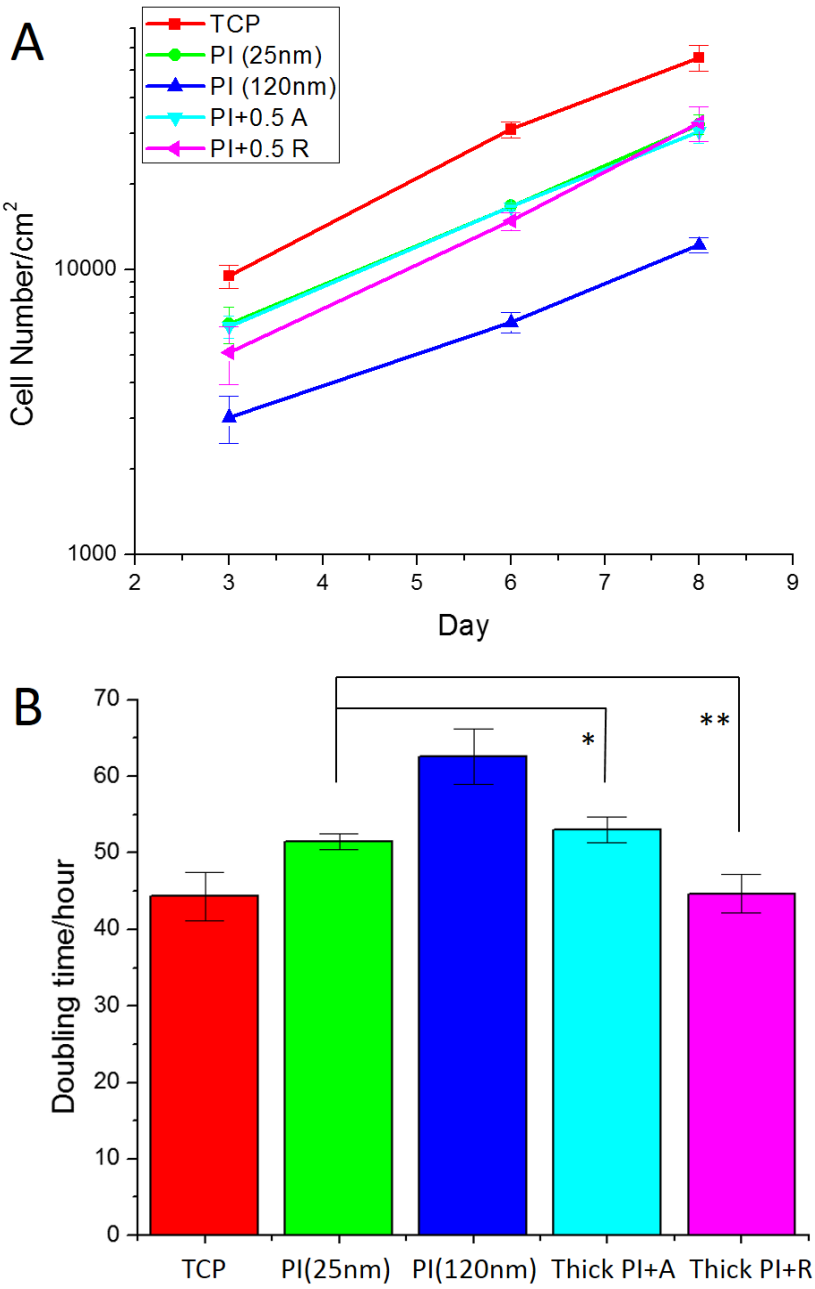

Figure 4.9 Cell proliferation curve (A) and doubling time (B) of DPSCs grown on: TCP, thin PI (25nm), thick PI (120nm), thick PI with Anatase TiO_2, and thick PI with Rutile TiO_2 coated Si substrates. The results differ at a statistical level of $P>0.05$ (*) and $P<0.05$ (**).

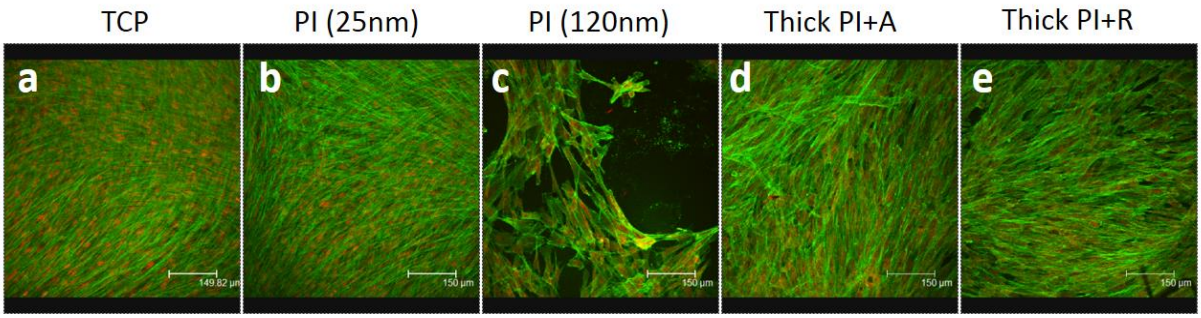

Figure 4.10 Confocal microscopy images of DPSCs morphology and organization on (a) TCP, (b) 25nm PI, (c) 120nm PI, (d) 120nm PI with Anatase TiO_2, and (e) 120nm PI with Rutile TiO_2 coated Si substrates at Day 8. DPSCs were stained with Alex Flour 488 for actin fiber (green) and Propium Iodide for nucleus (red).

Reference

[1] B.D. Ratner, Biomaterials science : an introduction to materials in medicine, 2nd ed., Elsevier Academic Press, Amsterdam ; Boston, 2004.
[2] M. Popa, R.M. Ottenbrite, C.V. Uglea, Medical applications of polymers, American Scientific Publishers, Stevenson Ranch, calif., 2011.
[3] D.M. Link, Med Instrum, 7 (1973) 151-152.
[4] P.L. Goering, W.D. Galloway, Fundam Appl Toxicol, 13 (1989) 193-195.
[5] J.I. Kroschwitz, Polymers : biomaterials and medical applications, Wiley, New York, 1989.
[6] E.P. McFadden, E. Stabile, E. Regar, E. Cheneau, A.T. Ong, T. Kinnaird, W.O. Suddath, N.J. Weissman, R. Torguson, K.M. Kent, A.D. Pichard, L.F. Satler, R. Waksman, P.W. Serruys, Lancet, 364 (2004) 1519-1521.
[7] D. Bhatnagar, A.K. Bherwani, M. Simon, M.H. Rafailovich, Journal of Materials Chemistry B, (2015).
[8] X. Yang, F. Yang, X.F. Walboomers, Z. Bian, M. Fan, J.A. Jansen, J Biomed Mater Res A, 93 (2010) 247-257.
[9] J.W. Weisel, Adv Protein Chem, 70 (2005) 247-299.
[10] M.W. Mosesson, J Thromb Haemost, 3 (2005) 1894-1904.
[11] L. Medved, J.W. Weisel, Fibrinogen, X.S.o.S.S.C.o.I.S.o.T. Factor, Haemostasis, J Thromb Haemost, 7 (2009) 355-359.
[12] L. Lorand, Ann N Y Acad Sci, 936 (2001) 291-311.
[13] E. Ernst, K.L. Resch, Ann Intern Med, 118 (1993) 956-963.
[14] A. Undas, J. Zalewski, M. Krochin, Z. Siudak, M. Sadowski, J. Pregowski, D. Dudek, M. Janion, A. Witkowski, K. Zmudka, Arterioscler Thromb Vasc Biol, 30 (2010) 276-282.
[15] M. Jaster, D. Horstkotte, T. Willich, C. Stellbaurn, W. Knie, S. Spencker, M. Pauschinger, H.P. Schultheiss, U. Rauch, Atherosclerosis, 197 (2008) 190-196.
[16] F. Bischoff, Clin Chem, 18 (1972) 869-894.
[17] H. Chen, L. Yuan, W. Song, Z.K. Wu, D. Li, Prog Polym Sci, 33 (2008) 1059-1087.
[18] C. Wischke, A. Lendlein, Clin Hemorheol Microcirc, 49 (2011) 347-355.
[19] J. Pluta, B. Karolewicz, Acta Pol Pharm, 60 (2003) 211-214.
[20] N. Angelova, D. Hunkeler, Trends Biotechnol, 17 (1999) 409-421.
[21] K. Modjarrad, S. Ebnesajjad, Handbook of polymer applications in medicine and medical devices, Elsevier/William Andrew, Amsterdam, 2013.
[22] Food, H.H.S. Drug Administration, Fed Regist, 67 (2002) 46852-46855.
[23] E. Piskin, J Biomater Sci Polym Ed, 6 (1995) 775-795.
[24] L.S. Nair, C.T. Laurencin, Prog Polym Sci, 32 (2007) 762-798.
[25] N. Sahiner, O. Ozay, Colloid Surface A, 378 (2011) 50-59.
[26] K.N. Stevens, M.L. Knetsch, A. Sen, V. Sambhy, L.H. Koole, ACS Appl Mater Interfaces, 1 (2009) 2049-2054.
[27] D.E. Babcock, R.W. Hergenrother, D.A. Craig, F.D. Kolodgie, R. Virmani, Biomaterials, 34 (2013) 3196-3205.
[28] S. Sanon, J.J. Maleszewski, C.S. Rihal, Catheter Cardio Inte, 83 (2014) 1152-1155.
[29] M. Amiji, K. Park, J Biomat Sci-Polym E, 4 (1993) 217-234.

[30] S. Dumitriu, Polymeric biomaterials, 2nd ed., Marcel Dekker, Inc., New York, 2002.
[31] D. Labarre, Trends in Biomaterials and Artificial Organs, 15 (2001) 1-3.
[32] C. Ozbek, A. Heisel, B. Gross, W. Bay, H. Schieffer, Cathet Cardiovasc Diagn, 41 (1997) 71-78.
[33] M. Gawaz, F.J. Neumann, I. Ott, A. May, A. Schomig, Circulation, 94 (1996) 279-285.
[34] A.J. Kirtane, G.W. Stone, Circulation, 124 (2011) 1283-1287.
[35] G.W. Stone, J.W. Moses, S.G. Ellis, J. Schofer, K.D. Dawkins, M.C. Morice, A. Colombo, E. Schampaert, E. Grube, A.J. Kirtane, D.E. Cutlip, M. Fahy, S.J. Pocock, R. Mehran, M.B. Leon, N Engl J Med, 356 (2007) 998-1008.
[36] B. Sivaraman, R.A. Latour, Biomaterials, 31 (2010) 832-839.
[37] W.B. Tsai, J.M. Grunkemeier, T.A. Horbett, J Biomed Mater Res A, 67 (2003) 1255-1268.
[38] B. Sivaraman, K.P. Fears, R.A. Latour, Langmuir, 25 (2009) 3050-3056.
[39] M. Zhang, Y. Wu, K. Hauch, T.A. Horbett, J Biomater Sci Polym Ed, 19 (2008) 1383-1410.
[40] J. Koo, M.H. Rafailovich, L. Medved, G. Tsurupa, B.J. Kudryk, Y. Liu, D.K. Galanakis, Journal of Thrombosis and Haemostasis, 8 (2010) 2727-2735.
[41] J. Koo, D. Galanakis, Y. Liu, A. Ramek, A. Fields, X.L. Ba, M. Simon, M.H. Rafailovich, Biomacromolecules, 13 (2012) 1259-1268.
[42] D.K. Galanakis, M. Neerman-Arbez, S. Brennan, M. Rafailovich, L. Hyder, O. Travlou, E. Papadakis, M.J. Manco-Johnson, A. Henschen, I. Scharrer, Thromb Res, 133 (2014) 1115-1123.
[43] N. Laurens, P. Koolwijk, M.P. de Maat, J Thromb Haemost, 4 (2006) 932-939.
[44] W.B. Tsai, J.M. Grunkemeier, C.D. McFarland, T.A. Horbett, J Biomed Mater Res, 60 (2002) 348-359.
[45] B. Sivaraman, R.A. Latour, Biomaterials, 32 (2011) 5365-5370.
[46] A. Chiumiento, S. Lamponi, R. Barbucci, Biomacromolecules, 8 (2007) 523-531.
[47] M.W. Mosesson, S. Sherry, Biochemistry, 5 (1966) 2829-&.
[48] E.A. Vogler, J Biomat Sci-Polym E, 10 (1999) 1015-1045.
[49] E.I. Peerschke, D.K. Galanakis, Blood, 69 (1987) 950-952.
[50] G. Banfi, G.L. Salvagno, G. Lippi, Clin Chem Lab Med, 45 (2007) 565-576.
[51] C.J. Jen, J.S. Lin, Am J Physiol, 261 (1991) H1457-1463.
[52] T.M. Ko, J.C. Lin, S.L. Cooper, Biomaterials, 14 (1993) 657-664.
[53] W.B. Tsai, J.M. Grunkemeier, T.A. Horbett, J Biomed Mater Res, 44 (1999) 130-139.
[54] Y. Wu, F.I. Simonovsky, B.D. Ratner, T.A. Horbett, J Biomed Mater Res A, 74 (2005) 722-738.
[55] J. Jesty, W. Yin, P. Perrotta, D. Bluestein, Platelets, 14 (2003) 143-149.
[56] S. Einav, D. Bluestein, Ann Ny Acad Sci, 1015 (2004) 351-366.
[57] A.D. Protopopova, N.A. Barinov, E.G. Zavyalova, A.M. Kopylov, V.I. Sergienko, D.V. Klinov, J Thromb Haemost, 13 (2015) 570-579.
[58] S. Cohen, K.M. Hargreaves, Pathways of the pulp, 9th ed., Mosby Elsevier, St. Louis, Mo., 2006.
[59] S. Patel, J.J. Barnes, M. Manogue, The principles of endodontics, 2nd ed., Oxford University Press, Oxford, 2013.
[60] A.R. Kemp, H. Peters, Ind Eng Chem, 33 (1941) 1391-1398.
[61] C.M. Friedman, J.L. Sandrik, M.A. Heuer, G.W. Rapp, J Dent Res, 54 (1975) 921-925.
[62] E.D. Gurgel-Filho, J.P. Andrade Feitosa, F.B. Teixeira, R.C. Monteiro de Paula, J.B. Araujo Silva, F.J. Souza-Filho, Int Endod J, 36 (2003) 302-307.

[63] C. Maniglia-Ferreira, E.D. Gurgel-Filho, J.B. de Araujo Silva, Jr., R.C. de Paula, J.P. de Andrade Feitosa, F.J. de Sousa-Filho, Eur J Dent, 7 (2013) 201-206.
[64] N. Gencoglu, Oral Surg Oral Med Oral Pathol Oral Radiol Endod, 96 (2003) 91-95.
[65] G. Tsukada, T. Tanaka, M. Torii, K. Inoue, J Oral Rehabil, 31 (2004) 1139-1144.
[66] G.H. Li, L.N. Niu, L.C. Selem, A.A. Eid, B.E. Bergeron, J.H. Chen, D.H. Pashley, F.R. Tay, J Dent, 42 (2014) 1124-1134.
[67] J.L. Gutmann, Dent Today, 30 (2011) 128, 130-121.
[68] J.J. Camps, W.J. Pertot, J.Y. Escavy, M. Pravaz, Endod Dent Traumatol, 12 (1996) 50-53.
[69] M. Zehnder, B. Guggenheim, International Endodontic Journal, 42 (2009) 277-287.
[70] E. Bodrumlu, T. Alacam, J Can Dent Assoc, 72 (2006) 733.
[71] G.T. Huang, Front Biosci (Elite Ed), 3 (2011) 788-800.
[72] R.M. El-Backly, A.G. Massoud, A.M. El-Badry, R.A. Sherif, M.K. Marei, Aust Endod J, 34 (2008) 52-67.
[73] T.F. Kuo, A.T. Huang, H.H. Chang, F.H. Lin, S.T. Chen, R.S. Chen, C.H. Chou, H.C. Lin, H. Chiang, M.H. Chen, J Biomed Mater Res A, 86 (2008) 1062-1068.
[74] J. Wang, X. Liu, X. Jin, H. Ma, J. Hu, L. Ni, P.X. Ma, Acta biomaterialia, 6 (2010) 3856-3863.
[75] W. Zhang, X.F. Walboomers, J.G. Wolke, Z. Bian, M.W. Fan, J.A. Jansen, Tissue engineering, 11 (2005) 357-368.
[76] C. Gennari, British journal of rheumatology, 32 Suppl 2 (1993) 11-14.
[77] H.A. Jeng, J. Swanson, J Environ Sci Health A Tox Hazard Subst Environ Eng, 41 (2006) 2699-2711.
[78] T.J. Brunner, P. Wick, P. Manser, P. Spohn, R.N. Grass, L.K. Limbach, A. Bruinink, W.J. Stark, Environ Sci Technol, 40 (2006) 4374-4381.
[79] E.A. Pascon, L.S. Spangberg, J Endod, 16 (1990) 429-433.
[80] G. Gambarini, L. Testarelli, D. Al-Sudani, G. Plotino, N.M. Grande, A. Lupi, B. Giardina, G. Nocca, M. De Luca, Open Dent J, 5 (2011) 29-32.
[81] B.D. Holt, A.G. Engelkemeir, Analytical Chemistry, 42 (1970) 1451-1453.
[82] J. Michetti, D. Maret, J.P. Mallet, F. Diemer, J Endod, 36 (2010) 1187-1190.
[83] P. Wang, X.B. Yan, D.G. Lui, W.L. Zhang, Y. Zhang, X.C. Ma, Dentomaxillofac Radiol, 40 (2011) 290-298.
[84] G. Kraus, C.W. Childers, K.W. Rollmann, J Appl Polym Sci, 10 (1966) 229-&.
[85] J. Diani, B. Fayolle, P. Gilormini, Eur Polym J, 45 (2009) 601-612.
[86] S. Cantournet, R. Desmorat, J. Besson, Int J Solids Struct, 46 (2009) 2255-2264.
[87] J.H. Xavier, S. Sharma, Y.S. Seo, R. Isseroff, T. Koga, H. White, A. Ulman, K. Shin, S.K. Satija, J. Sokolov, M.H. Rafailovich, Macromolecules, 39 (2006) 2972-2980.
[88] S. Sharma, M.H. Rafailovich, D. Peiffer, J. Sokolov, Nano Lett, 1 (2001) 511-514.
[89] H.N. An, S.J. Picken, E. Mendes, Soft Matter, 8 (2012) 11995-12001.
[90] G.P. Baeza, A.C. Genix, C. Degrandcourt, L. Petitjean, J. Gummel, M. Couty, J. Oberdisse, Macromolecules, 46 (2013) 317-329.
[91] J. Li, J. Yang, J. Li, L. Chen, K. Liang, W. Wu, X. Chen, J. Li, Biomaterials, 34 (2013) 6738-6747.
[92] D. Wu, J. Yang, J. Li, L. Chen, B. Tang, X. Chen, W. Wu, J. Li, Biomaterials, 34 (2013) 5036-5047.
[93] D. Dietschi, O. Duc, I. Krejci, A. Sadan, Quintessence international, 38 (2007) 733-743.
[94] D. Dietschi, O. Duc, I. Krejci, A. Sadan, Quintessence international, 39 (2008) 117-129.

[95] P. Holm-Pedersen, K. Schultz-Larsen, N. Christiansen, K. Avlund, Journal of the American Geriatrics Society, 56 (2008) 429-435.
[96] K. Otsu, M. Kumakami-Sakano, N. Fujiwara, K. Kikuchi, L. Keller, H. Lesot, H. Harada, Frontiers in physiology, 5 (2014) 36.
[97] C.-C. Chang, (2012).
[98] A.J. Engler, S. Sen, H.L. Sweeney, D.E. Discher, Cell, 126 (2006) 677-689.
[99] A.J. Engler, H.L. Sweeney, D.E. Discher, J.E. Schwarzbauer, Journal of musculoskeletal & neuronal interactions, 7 (2007) 335.
[100] D.E. Discher, P. Janmey, Y.L. Wang, Science, 310 (2005) 1139-1143.
[101] F. Rehfeldt, A.J. Engler, A. Eckhardt, F. Ahmed, D.E. Discher, Advanced drug delivery reviews, 59 (2007) 1329-1339.
[102] T. Yeung, P.C. Georges, L.A. Flanagan, B. Marg, M. Ortiz, M. Funaki, N. Zahir, W. Ming, V. Weaver, P.A. Janmey, Cell motility and the cytoskeleton, 60 (2005) 24-34.
[103] S. Sen, A.J. Engler, D.E. Discher, Cellular and molecular bioengineering, 2 (2009) 39-48.
[104] G.C. Reilly, A.J. Engler, Journal of biomechanics, 43 (2010) 55-62.
[105] A.W. Holle, A.J. Engler, Nature materials, 9 (2010) 4-6.
[106] J.R. Tse, A.J. Engler, PloS one, 6 (2011) e15978.
[107] R. d'Aquino, A. Graziano, M. Sampaolesi, G. Laino, G. Pirozzi, A. De Rosa, G. Papaccio, Cell death and differentiation, 14 (2007) 1162-1171.
[108] A. Almushayt, K. Narayanan, A.E. Zaki, A. George, Gene therapy, 13 (2006) 611-620.
[109] M. Miura, S. Gronthos, M. Zhao, B. Lu, L.W. Fisher, P.G. Robey, S. Shi, Proc Natl Acad Sci U S A, 100 (2003) 5807-5812.
[110] I.V. Nosrat, C.A. Smith, P. Mullally, L. Olson, C.A. Nosrat, The European journal of neuroscience, 19 (2004) 2388-2398.
[111] S. Gronthos, M. Mankani, J. Brahim, P.G. Robey, S. Shi, Proc Natl Acad Sci U S A, 97 (2000) 13625-13630.
[112] M. Mina, A. Braut, Cells, tissues, organs, 176 (2004) 120-133.
[113] K. Iohara, M. Nakashima, M. Ito, M. Ishikawa, A. Nakasima, A. Akamine, J Dent Res, 83 (2004) 590-595.
[114] B. Alliot-Licht, G. Bluteau, D. Magne, S. Lopez-Cazaux, B. Lieubeau, G. Daculsi, J. Guicheux, Cell and tissue research, 321 (2005) 391-400.
[115] J. Yu, Z. Deng, J. Shi, H. Zhai, X. Nie, H. Zhuang, Y. Li, Y. Jin, Tissue engineering, 12 (2006) 3097-3105.
[116] T. Blaine, R. Moskowitz, J. Udell, M. Skyhar, R. Levin, J. Friedlander, M. Daley, R. Altman, The Journal of bone and joint surgery. American volume, 90 (2008) 970-979.
[117] Y. Zhang, S. Ge, M.H. Rafailovich, J.C. Sokolov, R.H. Colby, Polymer, 44 (2003) 3327-3332.
[118] C. Chang, A. Bherwani, M. Simon, M. Rafailovich, V. Jurukovski, Annals of Materials Science & Engineering, 1 (2014) 1-7.
[119] M.T. Wei, A. Zaorski, H.C. Yalcin, J. Wang, S.N. Ghadiali, A. Chiou, H.D. Ou-Yang, Opt Express, 16 (2008) 8594-8603.
[120] D. Choquet, D.P. Felsenfeld, M.P. Sheetz, Cell, 88 (1997) 39-48.
[121] H.C. Yalcin, K.M. Hallow, J. Wang, M.T. Wei, H.D. Ou-Yang, S.N. Ghadiali, Am J Physiol Lung Cell Mol Physiol, 297 (2009) L881-891.
[122] X. Zheng, J.C. Sokolov, M.H. Rafailovich, Y. Strzhemechny, S.A. Schwarz, B.B. Sauer, M. Rubinstein, Physical Review Letters, 79 (1997) 241-244.

[123] K. Ghosh, Z. Pan, E. Guan, S. Ge, Y. Liu, T. Nakamura, X.D. Ren, M. Rafailovich, R.A. Clark, Biomaterials, 28 (2007) 671-679.
[124] B. Tian, P.L. Kaufman, Expert review of ophthalmology, 7 (2012) 177-187.
[125] B. Liu, S. Lu, Y.L. Hu, X. Liao, M. Ouyang, Y. Wang, Scientific reports, 4 (2014) 7008.